AD-A251 736

REPORT DOCUMENTATION PAGE

Form Approved
OMB No 0704-0188

Public reporting burden for this collection of information is estimated to average 1 hour per response, including the time for reviewing instructions, searching existing data sources, gathering and maintaining the data needed, and completing and reviewing the collection of information. Send comments regarding this burden estimate or any other aspect of this collection of information, including suggestions for reducing this burden, to Washington Headquarters Services, Directorate for Information Operations and Reports, 1215 Jefferson Davis Highway, Suite 1204, Arlington, VA 22202-4302, and to the Office of Management and Budget, Paperwork Reduction Project (0704-0188), Washington, DC 20503.

1. AGENCY USE ONLY (Leave blank)	2. REPORT DATE	3. REPORT TYPE AND DATES COVERED
	May 30, 1992	Final Technical Report 2/1/89-4/30/92

4. TITLE AND SUBTITLE
Micromechanics of Interfaces in High Temperature Composites

5. FUNDING NUMBERS
G-AFOSR-89-0269

2

6. AUTHOR(S)
Toshio Mura and Katherine T. Faber

7. PERFORMING ORGANIZATION NAME(S) AND ADDRESS(ES)
Center for Quality Engineering and Failure Prevention
Northwestern University
Evanston, IL 60208

8. PERFORMING ORGANIZATION REPORT NUMBER

9. SPONSORING/MONITORING AGENCY NAME(S) AND ADDRESS(ES)
Air Force office of Scientific Research
Directorate of Aerospace Science and
Directorate of Electronic and Materials Sciences
Building 410
Bolling AFB, DC 20332-6448

10. SPONSORING/MONITORING AGENCY REPORT NUMBER

11. SUPPLEMENTARY NOTES

DTIC
ELECTE
JUN 19 1992
S A D

12a. DISTRIBUTION AVAILABILITY STATEMENT
unlimited

This document has been approved for public release and sale; its distribution is unlimited.

12b. DISTRIBUTION CODE

13. ABSTRACT (Maximum 200 words)

Both theoretical and experimental approaches have been used to examine the micromechanics of interfaces in ceramic-matrix, fiber-reinforced composites. In order to examine variables which allow for the optimization of fracture toughness, analytical solutions first were developed to describe the stress displacement fields for a cylindrical inclusion adjoining a surface of an elastic half-space (equivalent to a single fiber intercepting a matrix crack). This same equivalent inclusion model was used to approximate multiple fibers spanning an internal crack. An energy approach was used to describe conditions of crack propagation and arrest in systems containing long fibers as a function of interface toughness, residual thermal stress, fiber size and concentration. Experimentally, the validity of fiber pullout tests was examined as means of acquiring accurate interfacial data. A new fiber pullout test was developed which best approximates matrix fracture, and fiber debonding and pullout in a full scale composite. Bridging forces by both on and off-axis fibers have been evaluated for a SiC/borosilicate composite, the latter providing the first experimental measures of bridging forces of inclined fibers. Finally, studies on fiber-reinforced cements have been conducted and compared to Mura's crack arrest theory with excellent agreement.

14. SUBJECT TERMS
composites, interfaces, ceramics, pullout, crack arrest, debonding, sliding, fibers, crack bridging

15. NUMBER OF PAGES
129

16. PRICE CODE

17. SECURITY CLASSIFICATION OF REPORT	18. SECURITY CLASSIFICATION OF THIS PAGE	19. SECURITY CLASSIFICATION OF ABSTRACT	20. LIMITATION OF ABSTRACT
			SAR

GENERAL INSTRUCTIONS FOR COMPLETING SF 298

The Report Documentation Page (RDP) is used in announcing and cataloging reports. It is important that this information be consistent with the rest of the report, particularly the cover and title page. Instructions for filling in each block of the form follow. It is important to **stay within the lines to meet optical scanning requirements.**

Block 1. Agency Use Only (Leave Blank)

Block 2. Report Date. Full publication date including day, month, and year, if available (e.g. 1 Jan 88). Must cite at least the year.

Block 3. Type of Report and Dates Covered. State whether report is interim, final, etc. If applicable, enter inclusive report dates (e.g. 10 Jun 87 - 30 Jun 88).

Block 4. Title and Subtitle. A title is taken from the part of the report that provides the most meaningful and complete information. When a report is prepared in more than one volume, repeat the primary title, add volume number, and include subtitle for the specific volume. On classified documents enter the title classification in parentheses.

Block 5. Funding Numbers. To include contract and grant numbers; may include program element number(s), project number(s), task number(s), and work unit number(s). Use the following labels:

C	- Contract	**PR**	- Project
G	- Grant	**TA**	- Task
PE	- Program Element	**WU**	- Work Unit Accession No.

Block 6. Author(s). Name(s) of person(s) responsible for writing the report, performing the research, or credited with the content of the report. If editor or compiler, this should follow the name(s).

Block 7. Performing Organization Name(s) and Address(es). Self-explanatory.

Block 8. Performing Organization Report Number. Enter the unique alphanumeric report number(s) assigned by the organization performing the report.

Block 9. Sponsoring/Monitoring Agency Names(s) and Address(es). Self-explanatory.

Block 10. Sponsoring/Monitoring Agency. Report Number. (If known)

Block 11. Supplementary Notes. Enter information not included elsewhere such as: Prepared in cooperation with...; Trans. of ..., To be published in .... When a report is revised, include a statement whether the new report supersedes or supplements the older report.

Block 12a. Distribution/Availablity Statement. Denote public availability or limitation. Cite any availability to the public. Enter additional limitations or special markings in all capitals (e.g. NOFORN, REL, ITAR)

DOD - See DoDD 5230.24, "Distribution Statements on Technical Documents."
DOE - See authorities
NASA - See Handbook NHB 2200.2.
NTIS - Leave blank.

Block 12b. Distribution Code.

DOD - DOD - Leave blank
DOE - DOE - Enter DOE distribution categories from the Standard Distribution for Unclassified Scientific and Technical Reports
NASA - NASA - Leave blank
NTIS - NTIS - Leave blank.

Block 13. Abstract. Include a brief (Maximum 200 words) factual summary of the most significant information contained in the report.

Block 14. Subject Terms. Keywords or phrases identifying major subjects in the report.

Block 15. Number of Pages. Enter the total number of pages.

Block 16. Price Code. Enter appropriate price code (NTIS only).

Blocks 17. - 19. Security Classifications. Self-explanatory. Enter U.S. Security Classification in accordance with U.S. Security Regulations (i.e., UNCLASSIFIED). If form contains classified information, stamp classification on the top and bottom of the page.

Block 20. Limitation of Abstract. This block must be completed to assign a limitation to the abstract. Enter either UL (unlimited) or SAR (same as report). An entry in this block is necessary if the abstract is to be limited. If blank, the abstract is assumed to be unlimited.

Micromechanics of Interfaces in High Temperature Composites

T. Mura and K. T. Faber

Final Report

for

AFOSR Grant No. 89-0269

for the period

February 1, 1989 - May 30, 1992

Accesion For
NTIS CRA&I
DTIC TAB
Unannounced
Justification
By
Distribution
Dist
A-1

I. Introduction

The ›rk described here represents a combined theoretical and experimental effort to address the mechanical behavior of interfaces in brittle fiber-reinforced brittle matrices. In the three year program, it was the aim of the study to examine variables which allow for toughness optimization of ceramic fiber-reinforced ceramic matrix composites. The results highlighted below range the gambit from the development of analytical solutions to solve the eigenstrain problem of both a single fiber (treated as a cylindrical inclusion) in an elastic half-space to the experimental verification of toughening models for one fiber-reinforced system. We have further examined the validity of a variety a test techniques which are used to acquire the material properties for composite systems, and have designed a new single fiber pullout technique reminiscent of actual fracture in fiber-reinforced composites. Finally, additional tests on model fiber systems have been performed to measure parameters, such as bridging forces, necessary for toughening models.

II. Highlights

(A) Inclusion Method Applied to Fiber-Reinforced Composite Problems

Exact solutions have been developed for axisymmetric stresses and displacement fields caused by a solid cylindrical inclusion in the presence of a uniform eigenstrain in a half space by using Green's functions. Green's functions were obtained for problems of an elastic half space with a free surface or rigidly fixed surface for a homogeneous isotropic elastic solid in earlier work.[1-3] The strain energy is also obtained in closed form. These

92 6 17 058

92-15926

solutions are now of the form which allows for evaluation of load diffusion and absorption capabilities in the matrix as a function of fiber length and material properties.(See Appendix 6.) Such solutions are necessary to examine problems of fiber debonding and pullout from a matrix.

(B) Theoretical Fracture Maps

An energy method has been used to examine the amount of toughening which results from the bridging, debonding, and sliding processes in ceramic matrix ceramic fiber composites. Using the equivalent inclusion method, the crack is approximated as a thin spheroid bridged by a series of fibers. In prior studies, this method was used to calculate a "fracture map" which described conditions for crack propagation and arrest with and without fiber reinforcement. The maps demonstrate the various contributions of bridging, debonding and frictional sliding for both constant and Coulomb friction. Most recently, this method has been extended to examine debond initiation stresses and bridging stresses as a function of interface toughness, residual thermal stresses, volume fraction and fiber radius.(See Appendix 3.) These stresses are compared to the fiber strength and hence, describe conditions where debonding and pullout are favored over fiber fracture. Calculations of bridging stresses are compared with those measured in the experimental program described below.

(C) Bridging Forces by Inclined Fibers or Whiskers

In general, fracture toughening models neglect any fibers which are not aligned parallel to the axis of applied stress under the supposition that they contribute little to the toughening process. In order to test this assumption, model composite specimens containing fibers of different inclination angle were fabricated with SiC monofilaments and borosilicate glass matrices via hot-pressing. The double cleavage drilled compression fracture mechanics specimen was used to characterize crack bridging by the inclined fibers. During stable crack growth, the crack opening displacement is monitored using a computer data acquisition system. The bridging force was extracted using a fracture mechanics analysis involving finite element computation. Results are shown in Appendix 1 and these represent the first quantitative experimental measurements of crack bridging by inclined fibers in ceramic composites. At small crack opening displacements, the bridging forces decrease with inclination angle. However, the bridging forces remain significant for large inclination angles over long distances (many orders of magnitude of the fiber diameter)

indicating that the fibers, though undergoing a bending stress, do not automatically fracture in the crack wake region . This is most likely due to matrix spalling, shown in Appendix 1, which diminishes the severity of the bending angle. These results are useful for toughening models of both fiber- and whisker-reinforced systems where the fiber reinforcement is not perpendicular to the crack plane.

(D) Fiber Debonding and Pullout using a Novel Pullout Test

In order to develop a basic understanding of the fiber debonding and pullout process as a function of interfacial chemistry and interfacial roughness, a number of interfacial (pullout) tests were evaluated. None were satisfactory to to adequately represent crack growth through the matrix of a real composite coupled with fiber interception, debonding, and pullout. In order to correct this deficiency, a modified single fiber pullout test was designed. In this test, a stiff fixture holds the specimen in place: a single fiber embedded along its entire length in matrix material. A pre-crack is started in the matrix and grown to intercept the fiber. The resultant load displacement is shown in Appendix 2. The curve shows the corresponding non-linear load displacement curve is indicative of progressive debonding of the fiber, followed by complete debonding and finally, frictional sliding. Pullout lengths of over 10 mm have been observed in the SiC monofilament/borosilicate glass system. Using the analytical methods of Kerans and Parthasarathy [4] and Marshall [5], an interfacial fracture toughness (G_i) of approximately 0.2 J/m^2 and a coefficient of friction (μ) of 0.14 have been measured.

(E) Uniaxial Tensile Tests of Fiber Composites

In order to compare experimental results with earlier crack arrest theory (Section B), studies on fiber-reinforced cements have been conducted. Specifically, the stress-strain response of steel fiber-reinforced cements with varying fractions of fiber-reinforcement were measured. Of particular interest is the composite stress at the bend-over-point in the stress-strain curve. The theoretical treatment establishes a critical volume fraction of reinforcement below which debonding precedes the bend-over-point in the stress-strain response and above which nonlinearity occurs prior to debonding. Good agreement is demonstrated between experiment and theory.

IV. Publications

The following papers have been published or submitted under the auspices of this grant: (All papers not yet in print are attached in Appendices 1 through 6.)

"Micromechanics of Interfaces: Crack Arrest by Strong Long Fibers in a Brittle Matrix", C. C. Yang, B. Tsai, S. Qin and T. Mura, pp. 113-20 in Microcracking-Induced Damage in Composites, AMD - Vol. 111. Ed. by G. Dvorak and D. Lagoudes, ASME, (1990).

"Crack Arrest by Strong Long Fibers in a Brittle Composite", C.C. Yang, W.-B. Tsai, S. Qin, T. Mura, S. Shibata and T. Mori, Composites Engg. **1**, 113-25 (1991).

"The Annular Crack Surrounding an Elastic Fiber in a Tension Field", A. C. Wijeyevickrema, L. M. Keer, K. Hirashima and T. Mura, Int. J. Solids Structures 27 [3] 315-28 (1991).

"Micromechanical theory and uniaxial tensile tests of fiber reinforced cement composites", C. C. Yang, T. Mura, and S. P. Shah, J. Mater. Res. 6 [11] 2463-73 (1991).

"Crack Bridging by Inclined Fibers in Ceramic Composites", H. Cai, K. T. Faber and E. R. Fuller, Jr., to appear in J. Amer. Ceram. Soc. (Appendix 1).

"Fiber Debonding and Pullout Processes in Ceramic Composites", D. R. Mumm and K. T. Faber, to appear in Ceram. Sci. Engg. Proc. (Appendix 2).

"Tensile Fracture of Fiber-Reinforced Composites: Influence of Thermal Residual Effect", W.-B. Tsai and T. Mura, to appear in Composites Engg. (Appendix 3)

"Loading Configurations of Single Fiber Pull-out Tests", H. Cai, Y. Makita and K. T. Faber, submitted to Materials Science and Engineering Letters. (Appendix 4)

"Inverse problems in elasticity", T. Koya and T. Mura, submitted to Computer Methods in Applied Mechanics and Engineering (Appendix 5).

"Load Diffusion and Absorption Problems from a Finite Fiber to an Elastic Infinite Matrix by the Equivalent Inclusion Method", V.-G. Lee and T. Mura, in preparation for J. Appl. Mech. (Abstract in Appendix 6)

V. Associated Personnel

Participating professionals supported and degrees granted under the auspices of this grant:

Master of Science:

Yoshio Makita (Materials Science and Engineering) "Determination of the Interfacial Properties in Fiber-Reinforced Composites via Model Single Fiber Pullout Tests", December, 1991

Doctor of Philosophy:

Tatsuhito Koya (Theoretical and Applied Mechanics), "Some Inverse Problems in Elasticity and Their Solution Methods", December, 1991

Wen-Ben Tsai (Theoretical and Applied Mechanics), "Micromechanics of Matrix Cracking in Fiber-Reinforced Composites", anticipated, June 1993

Daniel R. Mumm (Materials Science and Engineering), "Fiber Debonding and Pullout in Ceramic-Matrix Composites", anticipated, June, 1993

Ven-Gen Lee (Theoretical and Applied Mechanics), "Load Transfer Behavior of Fiber-Reinforced Materials by the Equivalent Inclusion Method", anticipated, June, 1993

Post-Doctoral Fellows:

Dr. Eizo Yoshitake (Materials Science and Engineering), 1989-1990

Dr. Hongda Cai (Materials Science and Engineering), 1990-91

VI. Scientific Interactions:

Presentations:

"Loading Configurations of Single Fiber Pullout Tests" H. Cai, K. T. Faber and J. O. Brittain, Fifth Technical Conference of the American Composites Society, East Lansing, MI, June, 1990.

"Photoelastic Analysis of Fiber Debonding in Brittle Matrix Composites", D. R. Mumm and K. T. Faber, Fifth Technical Conference of the American Composite Society, East Lansing, MI, June, 1990

"Micromechanics of Interfaces: Crack Arrest by Strong, Long Fibers in a Brittle Matrix", C. C. Yang, B. Tsai, S. Qin, T. Mura and T. Mori, The Winter Annual Meeting of the American Society of Mechanical Engineers, Dallas, TX, November, 1990.

"Crack Bridging by Inclined Whiskers", H. Cai and K. T. Faber, Annual Meeting of the American Ceramic Society, Cincinnati, OH, April, 1991.

"Fracture of a Brittle Matrix Composite with Strong, Long Fibers", W.-B. Tsai and T. Mura, Sixth Technical Conference of the American Composite Society, Albany, NY, October, 1991.

"Fiber Debonding and Pullout Processes in Ceramic Composites", D. R. Mumm and K. T. Faber, Annual Meeting on Composite Materials, Cocoa Beach, FL, January, 1992

"Crack Bridging by Inclined Fibers/Whiskers in Ceramic Composites", H. Cai, K. T. Faber and E. R. Fuller, Jr., Annual Meeting of the American Ceramic Society, Minneapolis, MN, April, 1992

"Investigation of Fiber Debonding and Pullout in Ceramic Composites", D. R. Mumm and K. T. Faber, Annual Meeting of the American Ceramic Society, Minneapolis, MN, April, 1992

VII. New Discoveries, Inventions, Applications, etc.

The main points from this work which could be used by the scientific and engineering communities are as follows:

1. Solutions were developed for stress and displacement fields for circular cylindrical inclusions adjoining the surface of a half-space. These solutions could be extended to treat single fiber pullout from a matrix.
2. A new single fiber test technique has been designed to determine interfacial properties of fiber-reinforced materials that more accurately reflects behavior in full-scale composites than any previous single-fiber test.
3. The first quantitative measurements of bridging forces were collected for inclined fibers in ceramic composites. Such measurements are imperative for accurately modelling toughening in fiber-reinforced and whisker-reinforced materials.
4. "Fracture maps" were designed to establish conditions for crack arrest, debonding, pullout, etc. in continuous fiber-reinforced ceramics.

VIII. References

1. H. Hasegawa, V.-G. Lee and T. Mura, "Green's Functions for Axisymmetric Problems of Dissimilar Elastic Solids" to appear in J. Appl. Mech.

2. H. Hasegawa, V.-G. Lee and T. Mura, "The Stress Fields Caused by a Circular Cylindrical Inclusion", to appear in J. Appl. Mech.

3. H. Hasegawa, V.-G. Lee and T. Mura, "Hollow Circular Cylindrical Inclusion Adjoining to the Surface of a Half Space", to appear in J. Appl. Mech.

4. R. J. Kerans and T. A. Parthasarathy, "Theoretical Analysis of the Fiber Pullout and Pushout Tests", J. Am. Ceram. Soc. 74 [7] 1585-96 (1991).

5. D. B. Marshall, "Analysis of Fiber Debonding and Sliding Experiments in Brittle Matrix Composites", Acta Metall., in press.

Crack Bridging by Inclined Fibers/Whiskers in Ceramic Composites

Hongda Cai*† and K.T. Faber*
Department of Materials Science and Engineering
Northwestern University
Evanston, Illinois 60208

Edwin R. Fuller, Jr.*
Ceramics Division
National Institute of Standards and Technology
Gaithersburg, Maryland 20899

Abstract

Crack bridging by inclined fibers has been studied in a brittle fiber–brittle matrix model ceramic composite. Results of the fiber bridging force vs. the crack opening displacement have been obtained for different fiber inclination angles using a fracture mechanics approach. Localized matrix cracking at the fiber has been observed and related to fiber inclination. The experimental results showing the effect of the fiber inclination angle are discussed and compared with theoretical analyses to provide insight into crack bridging by inclined fibers/whiskers. Implications for toughening by whisker bridging will also be discussed. [Key words: crack bridging, fibers, whiskers, inclination, composites]

For: *Journal of the American Ceramic Society*

Supported by the Air Force Office of Scientific Research under Funding No. G-AFOSR-89-0269.
*Member, American Ceramic Society.
†Present address: Ceramics Division, National Institute of Standards and Technology, Gaithersburg, MD 20899. On leave from Department of Materials Science and Engineering, Lehigh University, Bethlehem, PA.

I. Introduction

Significant increases of fracture toughness can be achieved by incorporating whiskers into ceramic matrices.[1-9] Studies of whisker–reinforced ceramic composites have established that the major toughening mechanism in these composites is crack bridging by whiskers.[6-9] A study of large-grain polycrystalline aluminas shows a similar toughening mechanism: crack bridging by grains.[9,10] These studies[7-10] have analyzed the mechanics of crack bridging by whiskers and grains. Due to the lack of information regarding the dependence of the bridging force on the whisker[††] inclination angle, the reinforcements are assumed to be perpendicular to the crack plane[7,9,10] or a simplistic relation between the bridging force and the inclination angle is used.[11] Alternatively, the inclined whiskers are neglected because they are considered to fail by bending and result in negligible toughening.[8] In reality, the whiskers can be of any orientation with respect to the crack plane in whisker-reinforced composites. The large majority of whiskers are not perpendicular to the crack plane. A more realistic model would consider whiskers of all orientations. Indeed, recent in situ observations for a SiC-whisker reinforced alumina have indicated the importance of inclined whiskers to the bridging process.[12] Therefore, it is essential to explore the effects of the fiber/whisker inclination angle on the degree of crack bridging by each individual fiber/whisker.

There have been a number of studies on the effect of fiber inclination angle on fiber pullout in systems other than brittle fiber–brittle matrix composites.[13-17] However, pullout of inclined fibers in brittle fiber–brittle matrix composites has received very limited treatment until recently. Wetherhold[11] analyzed the pullout of a short brittle fiber poorly bonded to the matrix. The simple analysis indicates that the frictional pullout force is inversely proportional to the cosine of the inclination angle ϕ of the fiber with respect to the surface normal for a given fiber embedded length. This relationship is assumed to apply for ϕ less than a physically plausible critical angle beyond which the fiber will fracture due to bending stresses.

Recently Leung and Li[18] conducted an extensive finite element analysis to study the effect of fiber inclination angle on the crack bridging stress in brittle fiber–brittle matrix composites. Matrix spalling was incorporated into the analysis based upon

[††]The term whiskers may also refer to elongated grains and short fibers.

observations in ductile fiber–brittle matrix composites.[17] The results for long fibers show that the bridging stress decreases with an increase of the inclination angle for a given crack opening displacement (COD). The maximum crack opening displacement before fiber failure is smaller for inclined fibers than aligned fibers. Nevertheless, the bridging stress from inclined fibers remains significant, particularly in the near crack-tip region where the crack opening displacements are small.

In spite of this progress in the theoretical aspect, there is little experimental work on the effect of fiber inclination on the fiber pullout or crack bridging. The objective of this work is to characterize experimentally crack bridging by inclined fibers/whiskers. Based upon the results for a single inclined whisker, the toughening contribution due to crack bridging of fibers/whiskers of distributed orientations can be estimated. The results are expected to be useful in providing insight into the mechanism of whisker bridging and in improving the present models of whisker bridging.

II. Fracture Mechanics Approach

For the present work, we chose to examine the effect of fiber inclination angle by studying a fiber bridging a crack which closely simulates the conditions of crack bridging in an actual composite. The double cleavage drilled compression (DCDC) fracture mechanics specimen was used for this purpose.

The DCDC specimen was developed by Janssen for studying slow crack growth in glasses.[19] The applied stress intensity K_{app} for the DCDC specimen is related to the measured crack length (a) and the applied compressive stress (σ_a) as follows:

$$K_{app} = \frac{\sigma_a \sqrt{r}}{g(a/r)} \tag{1}$$

where r is the central hole radius, $g(a/r)$ is the dimensionless geometric function of the crack length (a) and specimen geometry. The geometric function can be determined experimentally by testing specimens of known toughness or obtained by theoretical analyses. The advantages of the DCDC configuration (Fig. 1) include simple specimen shape and loading geometry, stable crack propagation over a large region of specimen length, and the fact that there is no need for crack guiding grooves.

The DCDC specimen has been used to study the crack interaction with an aligned fiber[20] and to quantify the toughening effect of fibers with a ductile interfacial layer.[21] The possibilities for quantifying the effects of bridging fibers using the DCDC specimen were demonstrated in terms of the traction exerted across the crack.[20] As shown schematically in Fig. 2(A), the crack is bridged by a fiber behind the crack tip. The influence of bridging can be expressed in terms of the change in the stress intensity:

$$\Delta K_b = K_c - K_{app} \tag{2}$$

where K_c is the base toughness of the matrix and K_{app} is the applied stress intensity (Negative ΔK_b indicates a closing action on the crack; positive ΔK_b indicates an opening action on the crack). Such results are useful for examining the toughening effect of a single fiber or whisker. However, for quantitative analyses of the propagation of a bridged crack, the key information is the relation between the bridging force and the crack opening displacement.[7,8,10,18,22]

The crack opening displacement (COD) can be measured directly using a displacement gauge. The bridging force must be extracted from the measured change in the stress intensity. It is necessary to establish the relation between the change in the stress intensity and the bridging force in the DCDC fracture mechanics specimen. The bridging action of a fiber behind the crack tip can be approximated by self-equilibrated traction forces (P/t) acting at a bridging distance (b) behind the crack tip, as illustrated in Fig. 2(B). For bridging forces very close to the crack tip (small bridging distance) the near tip solution can be used. For general values of the bridging distance, the crack bridging relation in the DCDC specimen is not available. A finite element analysis was used to obtain the relationship between the change in the stress intensity and traction forces. In this analysis, the change in the stress intensity (ΔK) was computed as a function of the bridging force (P/t), the crack length (a), and the bridging distance (b). For the given DCDC specimen geometry, the normalized change in stress intensity [$\Delta K\sqrt{r}/(P/t)$] is a function of the normalized crack length (a/r) and the normalized bridging distance (b/r). Typical results obtained by the finite element analysis are shown in Fig. 3 for three values of normalized crack length. From these numerical calculations, the crack bridging force was computed from the experimentally measured change in the stress intensity.

III. Experimental Procedure

The model composite system consists of SCS-6‡ silicon carbide fibers and a borosilicate glass‡‡ matrix. Specimen fabrication procedures were similar to those used by Butler et al.[23] The fibers were degreased in 1,1,1-trichloroethane and then rinsed with acetone and ethanol. The glass plates were washed with acetone and ethanol. Both the fibers and the glass plates were then dried at about 110°C for 60 minutes. The fibers were sandwiched between two glass plates. The sandwich assembly was placed in a hot press,§ which was then evacuated using a mechanical pump. The temperature was raised to 730°C before the hot pressing pressure was increased slowly to 1 MPa and held for 60 minutes. Specimens with fiber inclination angles from 0 to 40 degrees were fabricated. Each specimen with two fibers was machined to a DCDC specimen with the fibers located symmetrically on both sides of the center hole. There were four specimens for each fiber inclination angle. The specifications of the DCDC specimen dimensions are given in Fig. 1. For present work, the DCDC specimen with the Janssen geometry ($H/W = 10$, $W/r = 3.75$)[19] was used with the center hole radius of 0.795 mm and the specimen thickness of 3.5 mm.

Before testing, each DCDC specimen was precracked at the top and the bottom edges of the hole where the cracks would nucleate and grow.§§ A Knoop indenter with an indentation load of 29.4 N was used for this purpose. Compression testing of the DCDC specimen was carried out on an Instron universal testing machine¶ at a crosshead speed of 0.025 mm/min. The testing was conducted in a controlled environment of flowing dry nitrogen gas to minimize the effect of slow crack growth on the measured crack resistance of the glass. A crack opening displacement (COD) gauge was attached to measure the COD at the fiber location. A computerized data acquisition system was used to collect the crack length, load and crack opening displacement data. The crack length was monitored using a travelling microscope connected to a digital micrometer. Once the crack tip was located, the crack length, load and COD data were collected simultaneously. A data point was collected every

‡Silicon Carbide/Carbon fiber, AVCO Specialty Materials, Lowell, MA.

‡‡Soda borosilicate glass, Corning Code 7740, Corning Glass Works, Corning, NY.

§Vacuum hot press, GCA/Vacuum Industries, Inc.

§§It is not necessary to pre-crack the DCDC fracture mechanics specimen. To the authors' knowledge, none of previous studies pre-cracked the DCDC specimen. However, pre-cracking has the advantage of ensuring that cracks to starting at the center line. Without pre-cracking, the crack can propagate unstably to much greater distances than with pre-cracking, particularly if the load train is not very stiff.

¶Instron Model 1125, Instron, Corp., Canton, MA.

few seconds. Tests were stopped when the crack grew to a length of 13 to 15 times of the center hole radius. The maximum COD at the fiber was in the order of 10 μm. Borosilicate glass specimens without fibers were tested to obtain the dimensionless geometric function $g(a/r)$ for the DCDC specimen and for comparison purpose.

After mechanical testing, the specimen was bonded with a cyanoacrylate-based adhesive[¶¶] to a glass slide and a section of the specimen containing one of the fibers was cut with a slow speed diamond saw. After the adhesive was removed with acetone in an ultrasonic bath, two pieces of matrix glass held together by a bridging fiber were obtained. These two pieces of glass were then separated for microscopic examination. The fracture surface near the fiber was examined using scanning electron microscopy (SEM) to observe possible matrix spalling related to pullout of inclined fibers.

IV. Results

The experimentally determined dimensionless geometric function of the DCDC specimen is shown in Fig. 4 for the crack length range of interest. Results were obtained from two tests and provide almost identical geometric functions. This calibration function was used to compute the applied stress intensity for all other tests using Eq. (1).

The applied stress intensity vs. the crack length is presented in Fig. 5 for the cases: (A) without fibers, (B) fibers at $\phi = 0°$, (C) fibers at $\phi = 24°$, (D) fibers at $\phi = 40°$. In the case without fibers, the applied stress intensity is nearly independent of the crack length and is equal to the base toughness of the borosilicate glass. In the presence of bridging fibers, the applied stress intensity increases as the crack intercepts and passes the fiber, as shown in Fig. 5(B), (C) and (D). The results indicate a trend of decreasing bridging force with increasing inclination angle. Another interesting observation is that the applied stress intensity tends to decrease slightly as the crack approaches and passes the fiber before K_{app} increases again for the case of large inclination angles. This was consistently observed in a number of tests with large fiber inclination angles and is not well understood. Fiber inclination might have induced a mode II stress intensity which promotes crack growth.

[¶¶]Duro™ Quick Gel™ super glue, Loctite Corp., Cleveland, OH.

Based upon the applied stress intensity data, the equivalent bridging force (as defined in Fig. 2(B)) was computed using the finite element analysis described briefly in Section II. The crack bridging information consists of the bridging force as a function of the corresponding crack opening displacement. Examples of the bridging force vs. COD are presented in Fig. 6 for fiber inclination angles of 0, 8, 24, and 40°. For small fiber inclination angles, the bridging force levels off at a COD value of approximately 8 μm, indicating that fiber frictional sliding over the embedded length starts at this point. Comparison of these results shows a trend of decreasing bridging force with an increase in the fiber inclination angle in the range of COD studied, as expected from the stress intensity results.

The bridging force is plotted as a function of the inclination angle for different crack opening displacements in Fig. 7. The results show a general trend that the bridging force decreases with increasing fiber inclination angle for crack opening displacements between 2 and 10 μm. No data is available for greater crack opening displacements due to two limitations: 1) specimen size and 2) the crack length at which the test was stopped to prevent specimen shattering at high compressive stresses.

SEM micrographs of the matrix at the fiber are shown in Fig. 8 for fiber inclination angles of 8°, 24° and 40°. For the fiber inclination angle of 8°, fiber pullout occurred as the two pieces of matrix glass were separated. Little matrix cracking was observed (Fig. 8(A)). For large inclination angles, the fiber failed as the two pieces of matrix glass (held together by the fiber) were separated in the direction normal to the crack plane. Localized matrix cracking was observed (Fig. 8 (B) and (C)). The observed cracking pattern looks somewhat similar to cracks generated by Vickers indentation. The severity of matrix cracking increases with the fiber inclination angle, although part of the matrix cracking apparently has resulted from SEM sample preparation. In another observation, the matrix glass pieces were separated in the fiber direction using a fixture in order to minimize matrix cracking due to SEM sample preparation. This observation revealed much less severe matrix cracking. Further, the lateral crack did not intercepted the surface.

V. Discussion

We have studied the effect of fiber inclination on crack bridging in a SiC fiber–glass matrix model composite system. The results show that the bridging force by inclined fibers decreases with increasing fiber inclination angle in the range of crack opening displacement observed. This finding is in qualitative agreement with Leung and Li's theoretical analysis.[18]. Leung and Li have shown that the total crack bridging force consists of contributions due to: 1) the bending force on the inclined fiber and 2) fiber pullout.[18] The crack bridging force is the sum of these two contributions in a direction normal to the crack plane. The contribution from fiber bending increases with the fiber inclination angle initially but decreases at higher angle. The effect of localized matrix cracking relax the more heavily stressed fibers and thus reduce the difference between fibers lying at different angles. The fiber pullout contribution in the direction normal to the crack plane decreases with the inclination angle. Leung and Li[18] pointed out that for most composites the bridging force is usually dominated by the fiber pullout component. Therefore, the total bridging force decreases with the fiber inclination angle (see Ref. 18 for details).

It is expected that bending of inclined fibers eventually leads to fiber failure as the crack opening displacement increases. Nevertheless, the present study shows that the bridging force for inclined fibers is nowhere near zero. For example, crack bridging by fibers inclined by 40° is sustained more than 6 mm behind the crack tip (or more than 40 times the fiber diameter). Further crack propagation and large COD's would be required for fiber fracture. In actual whisker-reinforced materials, the majority of the whiskers are inclined with respect to the crack plane. Therefore, bridging by inclined whiskers is expected to make up the main portion of toughening in the near tip wake region. If the present results can be extended to whisker-reinforced ceramic composites, toughening predictions based on aligned fibers would represent overestimates. In addition, the dependence of bridging force on the whisker inclination angle and crack opening displacement also has a profound effect on the the shape of the crack resistance of the composite. Compared with predictions with aligned whiskers, the slope of the initial part of crack resistance curve would be smaller if the bridging force at a given COD is reduced as a result of whisker inclination.

Comparison of matrix cracking between smaller and large fiber inclination angles in Fig. 8 shows that localized matrix cracking is related to fiber inclination. It is

observed that larger fiber inclination angles result in a greater degree of matrix cracking. Matrix cracking reduces the severity of fiber bending and has the benefit of delaying fiber breakage.[18] Accordingly, the fiber can maintain integrity a greater distance behind the crack tip as a result of matrix cracking. At the same, matrix cracking also modifies the force–displacement relation.

The present observation that the crack bridging force decreases with the fiber inclination appears to be in contradiction with Wetherhold's simple analysis[11] which concludes that the bridging force should increase with the fiber inclination angle. It must be pointed out that the results of the present study are obtained for the case where the fiber pullout dominates the total bridging force. Such cases include those with large embedded fiber length (e.g., the embedded length more than 20 times of the fiber radius for present study) and high interfacial shear strength and frictional shear stress. For very short whiskers or elongated grains, or very low interfacial shear strength and frictional shear stress, increased frictional shear or interlocking due to whisker inclination could dominate the bridging force. In this case, the bridging force is expected to increase as a results of whisker inclination angle until whiskers fail or the matrix spalls. Indeed, high values of the coefficient of friction (greater than unity) required for parametric fitting of crack resistance curves in some alumina ceramics using a grain-bridging model can be attributed to geometrical irregularities including grain interlocking.[10] Based upon the foregoing discussion, it is clear that there is no general trend for the effect of the fiber/whisker inclination angle on crack bridging. It is determined by other factors in addition to the fiber/whisker inclination angle. The present study covers a limited range of these factors, and further studies are required to obtain a complete quantitative picture.

Acknowledgement: The authors would like to thank Prof. Brian Moran (Northwestern University) and Dr. Christopher Leung (Massachusetts Institute of Technology) for useful discussions, and Drs. Brian Lawn and Nitin Padture (National Institute of Standards and Technology) for comments on the manuscript.

References

[1]P. F. Becher and G. C. Wei, "Toughening Behaviour in SiC-Whisker-Reinforced Alumina," *J. Am. Ceram. Soc.*, **67** [12] C267-C269 (1984).

[2]P. F. Becher, T. N. Tiegs, J. C. Ogle and W. H. Warwick, "Toughening of Ceramics by Whisker Reinforcement," pp.61-73 in *Fracture Mechanics of Ceramics*, Vol.7, R. C. Bradt, A. G. Evans, D. P. H. Hasselman and F. F. Lange, eds., Plenum Press, New York, 1986.

[3]N. Claussen and G. Petzow, "Whisker-Reinforced Zirconia-Toughened Ceramics," pp.649-662 in *Tailoring Multiphase and Composite Ceramics*, R. E. Tressler, G. L. Messing, C. G. Pantano and R. E. Newnham, eds., Plenum Press, New York, 1986.

[4]T. N. Tiegs and P. F. Becher, "Whisker Reinforced Ceramic Composites," pp.639-647 in *Tailoring Multiphase and Composite Ceramics*, R. E. Tressler, G. L. Messing, C. G. Pantano and R. E. Newnham, eds., Plenum Press, New York, 1986.

[5]J. Homeny, W. L. Vaughn and M. K. Ferber, "Processing and Mechanical Properties of SiC-Whisker-Al_2O_3-Matrix Composites," *Am. Ceram. Soc. Bull.*, **67** [2] 333-338 (1987).

[6]M. Rühle, B. J. Dalgleish and A. G. Evans, "On the Toughening of Ceramic by Whiskers," *Scr. Metall.*, **21** [5] 681-686 (1987).

[7]P. F. Becher, C.-H. Hsueh, P. Angelini and T. N. Tiegs, "Toughening Behavior in Whisker-Reinforced Ceramic Matrix Composites," *J. Am. Ceram. Soc.*, **71** [12] 1050-1061 (1988).

[8]G. H. Campbell, M. Rühle, B. D. Dalgleish and A. G. Evans, "Whisker Toughening: A Comparison Between Aluminum Oxide and Silicon Nitride Toughened with Silicon Carbide," *J. Am. Ceram. Soc*, **73** [3] 521-530 (1990).

[9]P. F. Becher, E. R. Fuller, Jr. and P. Angelini, "Matrix-Grain-Bridging Contributions to the Toughness of Whisker-Reinforced Ceramics," *J. Am. Ceram. Soc.*, **74** [9] 2131-35 (1991).

[10]S. J. Bennison and B. R. Lawn, "Role of Interfacial Grain-Bridging Sliding Friction in the Crak-Resistance and Strength Properties of Nontransforming Ceramics," *Acta Metall.*, **37** [10] 2659-2671 (1989).

[11]R. C. Wetherhold, "Energy of Fracture for Short Fiber-Brittle Matrix Composites with Planar Fiber Orientation," *Mater. Sci. Eng.*, **A112**, 31-37 (1989).

[12]J. Rödel, E. R. Fuller, Jr. and B. R. Lawn, "In-Situ Observation of Toughening Processes in Alumina Reinforced with Silicon Carbide Whiskers," *J. Am. Ceram. Soc.*, **74** [12] 3154-57 (1991).

[13]J. Morton and G. W. Groves, "The Cracking of Composites Consisting of Discontinuous Ductile Fibres in a Brittle Matrix - Effect of Fibre Orientation," *J. Mater. Sci.*, **9**, 1436-1445 (1974).

[14]J. Morton and G. W. Groves, "The Effect of Metal Wires on the Fracture of a Brittle-Matrix Composite," *J. Mater. Sci.*, **11**, 617-622 (1976).

[15]M. R. Piggott, "Toughness in Obliquely-Stressed Fibrous Composites," *J. Mech. Phys. Solids*, **22** [6] 457-468 (1974).

[16]A. E. Naaman and S. P. Shah, "Pull-Out Mechanism in Steel Fiber-Reinforced Concrete," *ASCE J. Struct. Div.*, **102** [ST8] 1537-1548 (1976).

[17]V. C. Li, Y. Wang and S. Backer, "Effect of Inclining Angle, Bundling, and Surface Treatment on Synthetic Fiber Pull-Out from a Cement Matrix," *Composites*, **21** [2] 132-140 (1990).

[18]C. K. Y. Leung and V. C. Li, "Effect of Fiber Inclination on Crack Bridging Stresses in Brittle Fiber Reinforced Brittle Matrix Composites," *J. Mech. Phys. Solids*, in press.

[19]C. Janssen, "Specimen For Fracture Mechanics Studies on Glass," pp.10.23–10.30 in *Tenth International Congress on Glass*, Kyoto, Japan, July 8-13, The Ceramic Society of Japan, Kyoto, Japan, 1974.

[20]T. W. Coyle, E. R. Fuller, Jr., P. Swanson and T. Palamides, "Fracture Mechanics Characterization of Crack/Fiber Interactions in Ceramic Matrix Composites," *Ceram. Eng. Sci. Proc.*, **8** [7-8] 630-635 (1987).

[21]E. P. Butler, H. M. Chan, T. R. Palamides and E. R. Fuller, Jr., "Debonding and Frictional Effects During Fibre Pull-Out in Model SiC Fibre-reinforced Glass Composites in Relation to Fracture Resistance," pp.178-187 in *Proceedings of the International Symposium on Advances in Processing of Ceramic and Metal Matrix Composites*, H. Mostaghaci, eds., Pergamon Press, Halifax, 1989.

[22]D. B. Marshall, B. N. Cox and A. G. Evans, "The Mechanics of Matrix Cracking in Brittle-Matrix Fiber Composites," *Acta Metall*, **33** [11] 2013-2021 (1985).

[23]E. P. Butler, E. R. Fuller, Jr. and H. M. Chan, "Interface Properties for Ceramic Composites from a Single-Fiber Pullout Test," pp.17-24 in *Tailored Interfaces in Composite Materials*, C. G. Pantano and E. J. H. Chen, eds., MRS, Pittsburgh, PA, 1990.

List of Figures

Fig. 1. Schematic of the DCDC specimen in which $2H$ is the specimen height, $2W$ is the specimen width, t is the thickness, r is the radius of the center hole, a is the crack length, and σ_a is the applied compression stress. For the Janssen geometry, $H/W = 10$ and $W/r = 3.75$.

Fig. 2. Schematic of crack bridging in the DCDC specimen: (A) Fibers at an inclination angle ϕ bridge the DCDC cracks; (B) Representation of the bridging force by traction force P/t. The distance from the crack tip to the bridging force, or the bridging distance, is denoted by b.

Fig. 3. Crack bridging relations in the DCDC fracture mechanics specimen showing the normalized change in the stress intensity as a function of the normalized bridging distance for different crack lengths. The results were obtained using a finite element analysis. The dimensions of the DCDC specimen are: $H/W = 10$, $W/r = 3.75$, and $r = 0.795$.

Fig. 4. The dimensionless geometric function of the DCDC fracture specimen obtained experimentally.

Fig. 5. Examples of the results showing the applied stress intensity vs. the normalized crack length for the cases: (A) without fibers, (B) fibers at $\phi = 0°$, (C) fibers at $\phi = 24°$ and (D) fibers at $\phi = 40°$.

Fig. 6. Examples of the results showing the bridging force vs. the crack opening displacement for different fiber inclination angles.

Fig. 7. The bridging force as a function of the inclination angle for different crack opening displacements. Open symbols indicate data points from a single test.

Fig. 8. Matrix cracking related to fiber inclination at inclination angles: (A) 8°, (B) 24°, and (C) 40°.

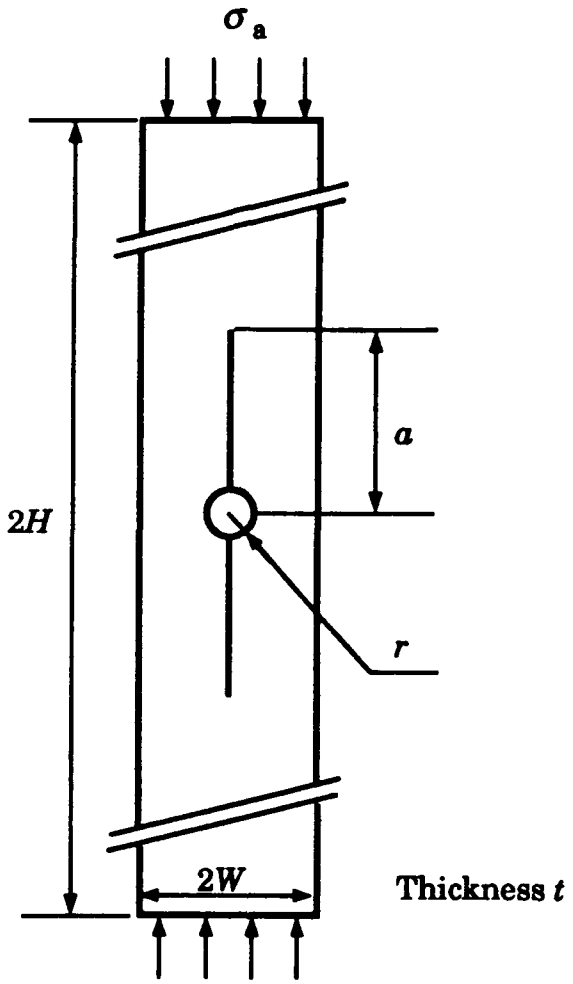

Fig. 1

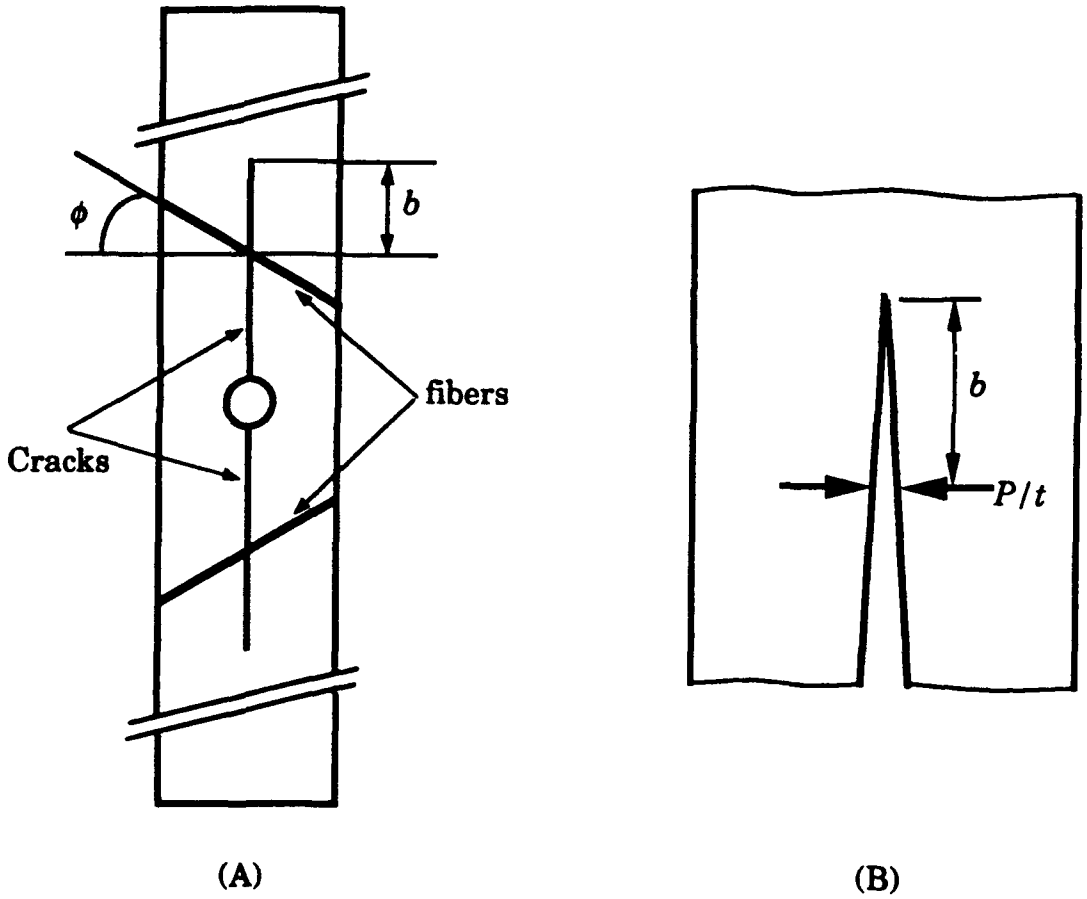

Fig. 2

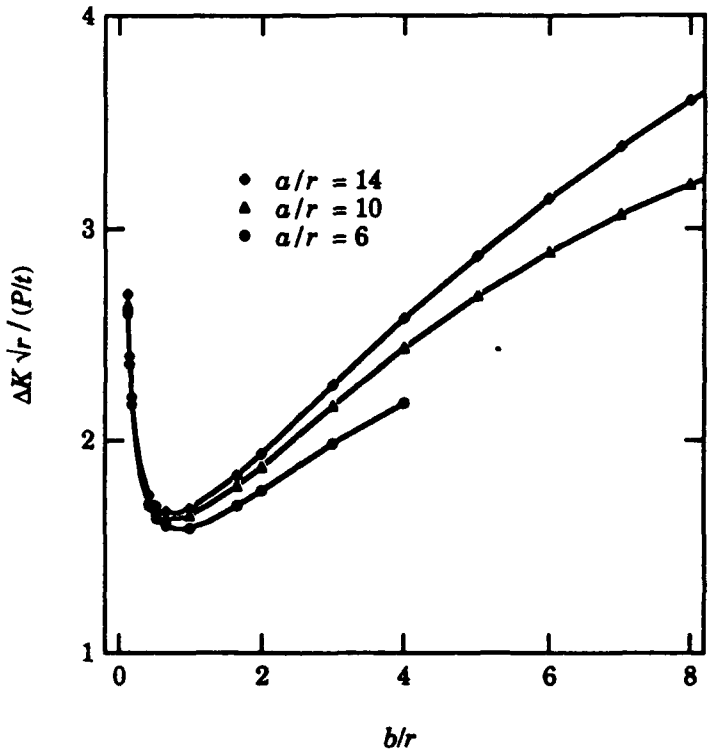

Fig. 3

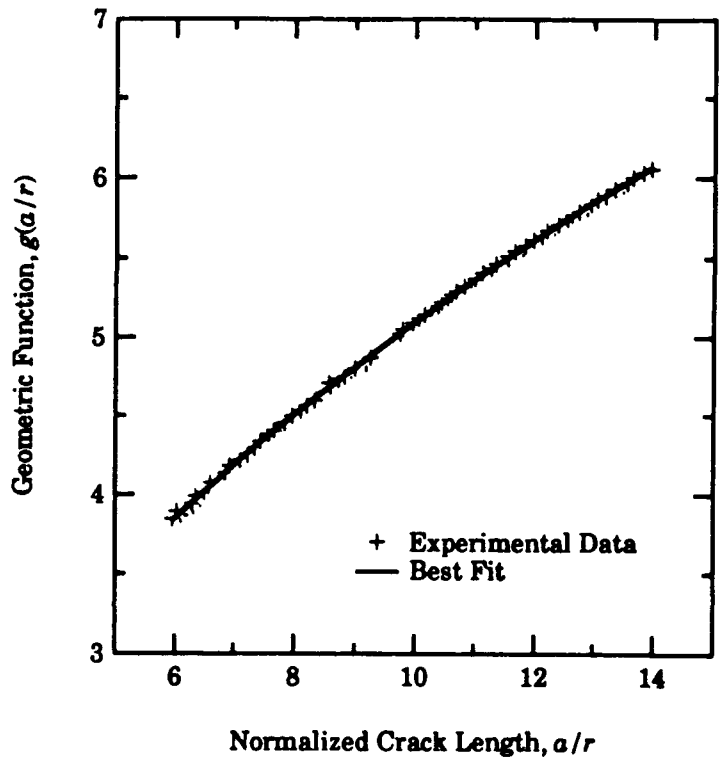
7
6
5
4
3
6
8
10
12
14
Geometric Function, g(a/r)
Normalized Crack Length, a/r
+ Experimental Data
— Best Fit

Fig. 4

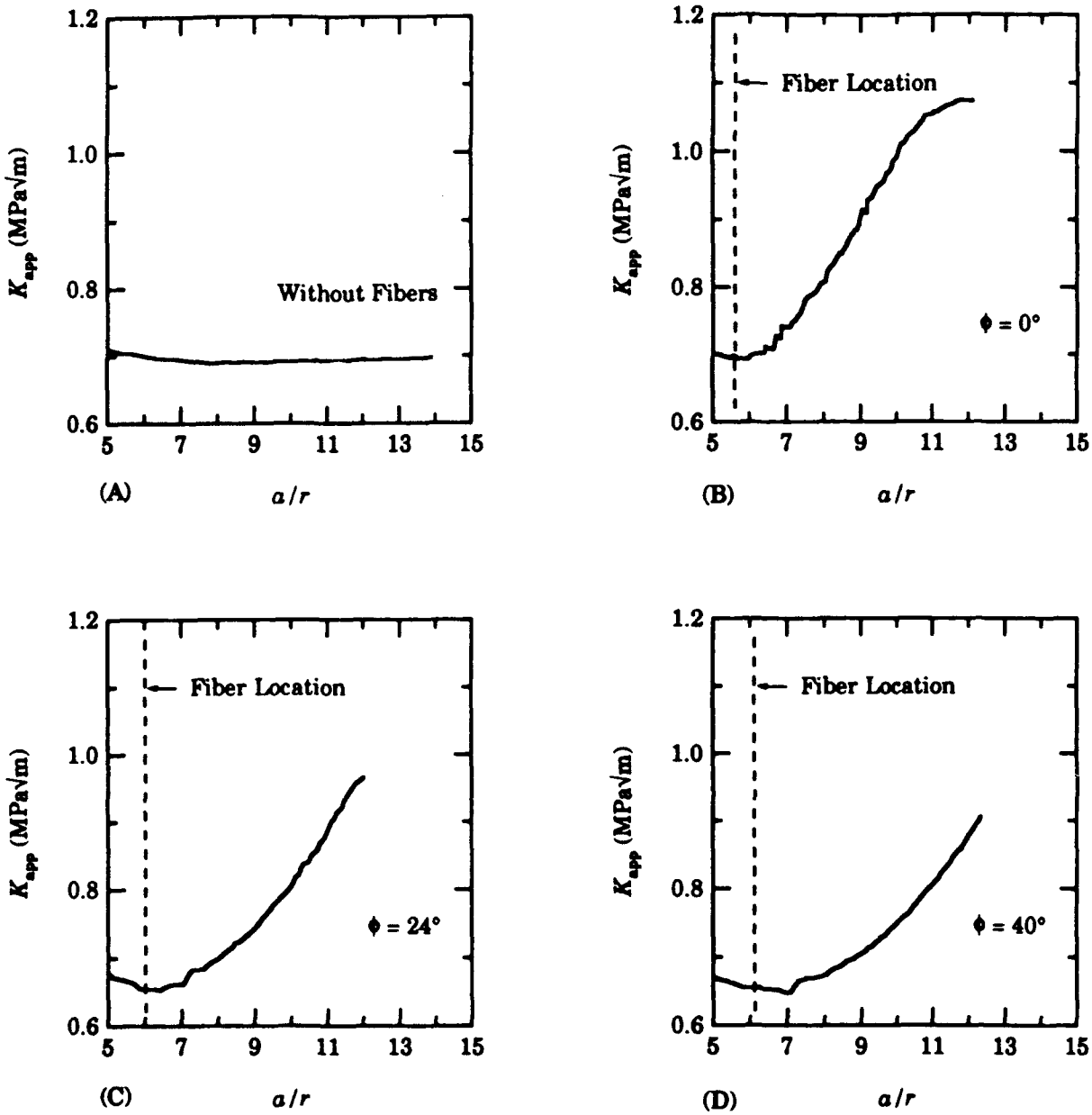
1.2
1.0
0.8
0.6
K_{app} (MPa√m)
Without Fibers
5
7
9
11
13
15
(A)
a/r
Fiber Location
ϕ = 0°
(B)
a/r
Fiber Location
ϕ = 24°
(C)
a/r
Fiber Location
ϕ = 40°
(D)
a/r

Fig. 5

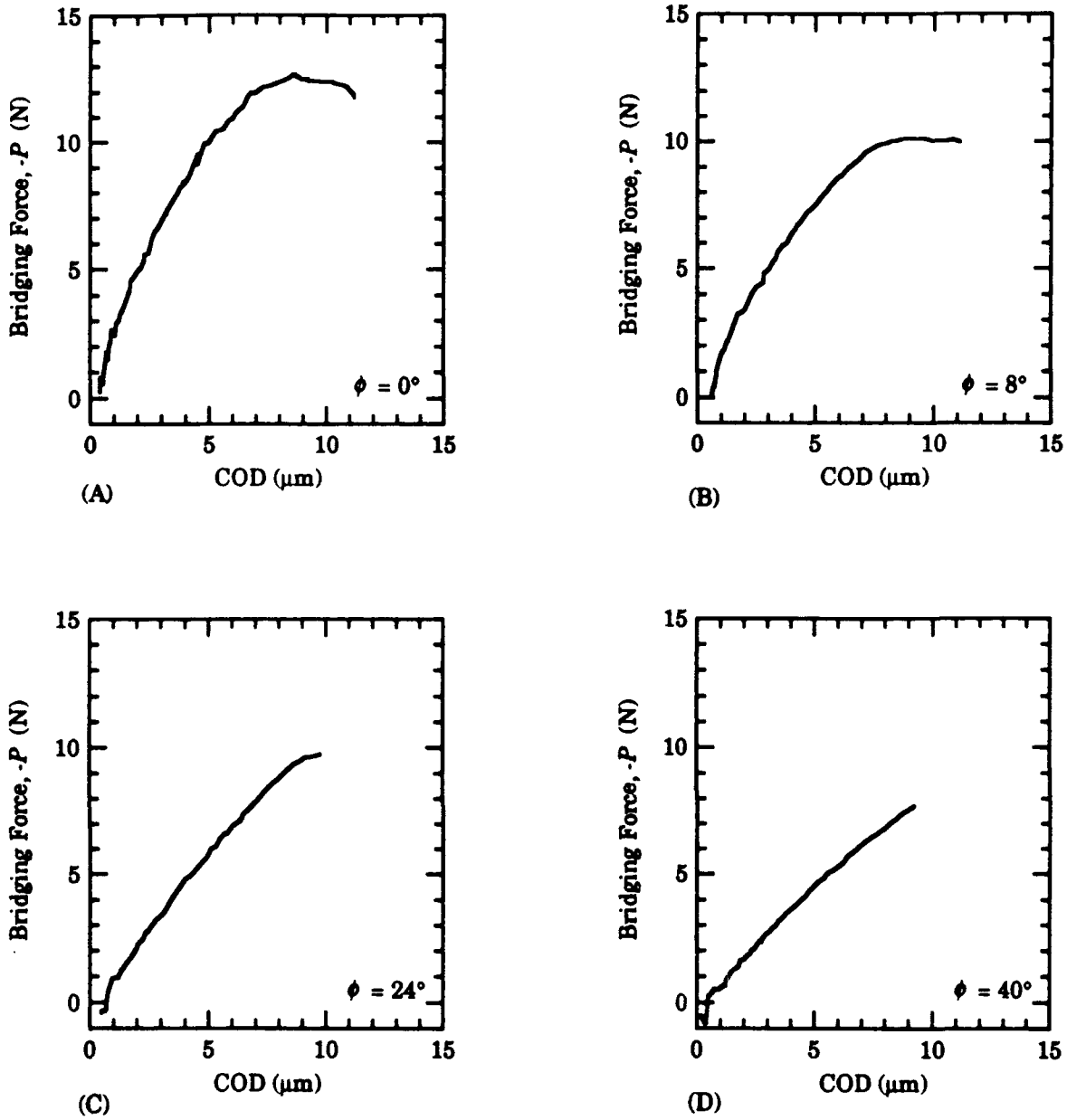

Fig. 6

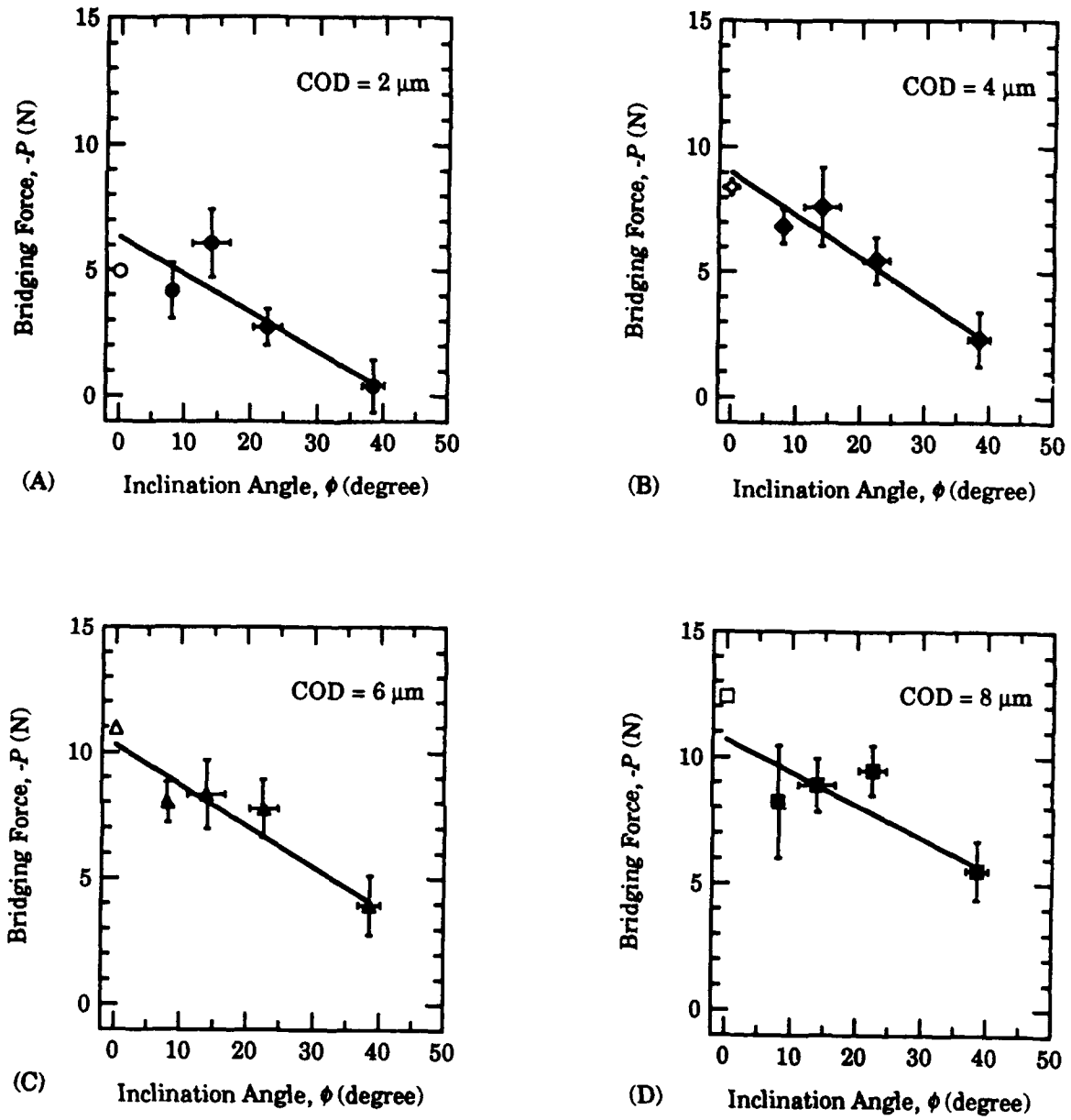
COD = 2 μm
COD = 4 μm
COD = 6 μm
COD = 8 μm
Bridging Force, -P (N)
Inclination Angle, φ (degree)
(A)
(B)
(C)
(D)

Fig. 7

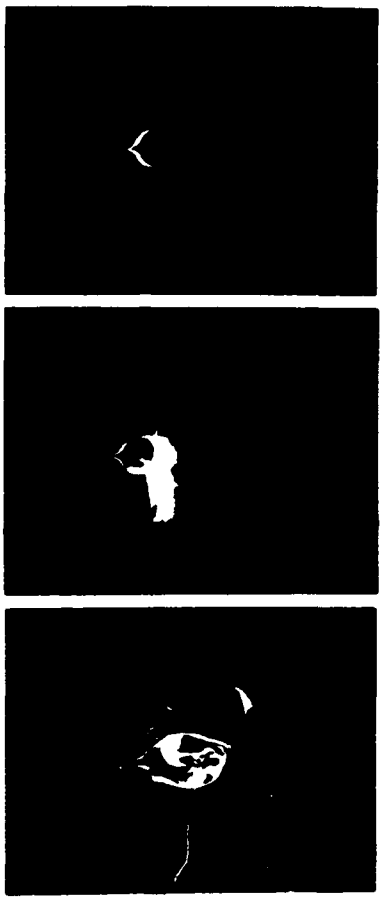

(A) (B) (C)

Fig. 8

Presented at the 16th Annual Conference on Composites and Advanced Ceramics
sponsored by the American Ceramic Society
Cocoa Beach, FL, January 7-10, 1992

FIBER DEBONDING AND PULLOUT PROCESSES IN CERAMIC COMPOSITES

D.R. Mumm and K.T. Faber
Northwestern University
Department of Materials Science and Engineering
Evanston, IL 60208–3108

The fiber debonding and pullout behavior in a model ceramic composite system has been investigated using a novel single-fiber pullout technique. Stable, progressive debonding was observed prior to fiber fracture and frictional fiber pullout. Interfacial parameters were calculated from single load-displacement curves using a recent analysis of the fiber debonding and pullout process. The interfacial parameters extracted from these experiments are consistent with independent measurements reported in the literature. The morphology of the fiber surface appears to play a significant role in determining the fiber debonding and sliding behavior.

INTRODUCTION

It is now acknowledged that the mechanical properties of fiber-reinforced ceramic composites are controlled primarily by the interfacial properties.[1,2] Recognition of the importance of the interfacial properties has prompted the development of a number of techniques to evaluate these parameters, including the fiber pullout[3,4] and pushdown[5] tests. The work described here utilizes a variant of the fiber pullout technique.

Extraction of interfacial properties from single-fiber pullout tests requires fitting of the experimental data to appropriate micro-mechanics based models of the fiber debonding and pullout process. A number of such analytical models have been developed recently with varying assumptions and approximations. A recent analysis by Kerans and Parthasarathy,[2] which has been used to analyze fiber push-down data,[6] is also applicable for the fiber pullout experiment. The model is based on progressive debonding of the fiber and accounts for the thermal mismatch of the fiber and matrix, including the residual axial stress, and specifically addresses the role of fiber surface asperities.

The model[2] considers a fiber of radius r embedded in a cylinder of infinite radius of the matrix with a length l_o protruding from the matrix. The response load P_a is

related to the displacement at the end of the fiber during progressive debonding as follows:

$$\delta = \frac{l_o P_a}{\pi r^2 E_f} + \frac{1 - 2\nu_f k}{2\mu k \pi r E_f}\left[P_d + P_r - P_a + (P^* - P_r)\ln\left\{\frac{P^* - (P_d + P_r)}{P^* - P_a}\right\}\right] \quad (1)$$

where k is given as:

$$k = \frac{E_m \nu_f}{E_f(1 + \nu_m) + E_m(1 - \nu_f)} \quad (2)$$

and E_f and E_m are the elastic moduli of the fiber and matrix, ν_f and ν_m are the respective Poisson's ratios and μ is the friction coefficient. The parameter P_r is the residual axial load on the fiber due to thermal expansion mismatch between the fiber and matrix:

$$P_r = -(\Delta\alpha\Delta T)\pi r^2 E_f \left\{\frac{1 + 2k}{1 - 2\nu_f k}\right\} \quad (3)$$

where $\Delta\alpha$ is the thermal expansion coefficient difference for the matrix and fiber $(\alpha_m - \alpha_f)$ and ΔT is the change in temperature over which the residual stresses develop.

The term P_d corresponds to the critical axial load in the fiber at the debond crack tip necessary to propagate the debond crack. It is directly related to the critical strain energy release rate of the interface according to:

$$G_c^i = \frac{(1 - 2\nu_f k)\, P_d^2}{4\pi^2 r^3 E_f} \quad (4)$$

P^* is a critical axial load on the fiber at which Poisson's contraction completely counteracts the residual normal stress and the surface asperity effects such that there is no frictional resistance to sliding. When the response load P_a equals P^*, the debond crack will propagate through the specimen at constant load with a fixed length frictional sliding zone behind the debond crack tip. P^* is directly related to the effective normal stress at the interface, σ_n^{eff}, as follows:

$$P^* = -\frac{\sigma_n^{eff}\, \pi r^2}{k} \quad (5)$$

It is our intent in this study to use a unique single-fiber pullout technique to experimentally investigate the progressive debonding behavior in a model ceramic composite. The role of the interfacial friction, interfacial debond energy, residual stress state and fiber surface morphology will be explored. The results are to be analyzed with the model discussed above to extract interfacial properties from the progressive debonding portion of individual load-displacements curves.

EXPERIMENTAL PROCEDURES

For this investigation, single-fiber composite specimens were fabricated from SiC monofilaments* embedded in a soda-borosilicate glass†. The SiC monofilaments are produced by chemical vapor deposition (CVD) of SiC onto a 33μm diameter carbon core. The CVD process results in a high degree of surface roughness, which has been shown to have a profound effect on the fiber debonding and sliding behavior.[7] The surface of the monofilament consists of two carbon rich layers which are believed to provide the weak interface necessary for fiber debonding and pullout.

The samples were prepared by hot-pressing in an argon atmosphere at temperatures of approximately 750°C for 15 minutes under a stress of 5.0 MPa. To fabricate samples with the geometry discussed below, it is necessary to have the embedded fiber parallel to the faces of the hot-pressed disk. To accomplish this, one half of the glass frit was cold pressed into the hot-press die under a stress of approximately 3.0 MPa. The top ram was removed and a segment of the monofilament was placed into the die. The remaining glass frit was then cold pressed into the die at an equivalent stress. The die was then loaded into the hot-press and processed according to the conditions outlined above.

The sample geometry that was developed and adopted for use in these experiments is shown in Figure 1. A rectangular block of the matrix contains a single fiber running down the axis of the sample. The sample was notched to have a greatly reduced cross-section at the midpoint of the sample.

This modified single fiber pullout geometry was chosen to provide a more realistic modeling of the fiber debonding and pullout process during composite fracture relative to the standard single fiber pullout geometry used in previous studies.[4,8] During the testing procedure, a crack is propagated through the matrix leaving the fiber as a bridging element. Therefore, an artificial surface is not used to model the matrix crack and any artificial barrier to debond initiation is avoided. The interaction of the matrix crack with the fiber to initiate debonding is more clearly represented.

The machined samples were directly bonded to the load train of a standard mechanical test frame‡ using a cyanoacrylate based adhesive§, taking care not to bond the exposed fiber ends, as indicated in Figure 2.

During the pullout test, the matrix crack opening displacement (COD) was measured using a traveling microscope attached to a digital micrometer.¶ The micrometer was interfaced to a data acquisition system which simultaneously recorded the load. The crosshead speed was held constant at 10μm/min.

---

*SCS-6 SiC Monofilament, Textron Specialty Materials, Lowell, MA

†Pyrex #7740, Corning Glass Works, Corning, NY

‡Instron 4505 testing machine, Instron Corporation, Canton, MA

§Duro Quick Gel, Loctite Corporation, Cleveland OH

¶Mitutoyo digimatic micrometer head, MTI Corporation, Paramus, NJ

RESULTS AND DISCUSSION

Representative data for these experiments are shown in Figure 3, where two sets of data are superimposed. The load increases continuously with the crack opening displacement until fiber fracture. The non-linearity in the initial portion of the data is expected as the compliance of the sample increases with progressive debonding. After the sharp drop in load, the load decreases further with decreasing embedded length as the debonded fiber is frictionally pulled out of the matrix.

It is interesting to note that, although the peak loads and the COD's at the peak load for the two data sets are very different, the final pullout lengths are nearly equal. Furthermore, the magnitude of the peak loads and the large load drop with fiber fracture indicate that the debond crack had progressed far ahead of the eventual fiber fracture point.

Figure 4 demonstrates the application of the Kerans and Parthasarathy model[2] to the data, showing the saturation load P^* as well as the debond propagation load P_d. Fiber fracture occurs well before the saturation load P^* is reached.

The Kerans and Parthasarathy model (Equation 1) was fit to individual data sets using a three-parameter non-linear least squares[‖] fitting routine. For the sample geometry used herein, the initial length l_o is zero and the first term of Equation 1 is omitted. The fitted parameters μ, P_d, and P^* for each of the data sets shown in Figure 3 are reported in Table 1. From these fitted parameters, the effective normal stress and the interfacial strain energy release rate were calculated, and are also reported in Table 1.

Table 1: Fitted parameters

Data Set	μ	P_d (N)	P^* (N)	σ_n^{eff} (MPa)	G_i ($\frac{J}{m^2}$)
1	0.144	1.17	104.9	201.0	0.24
2	0.138	0.89	100.4	192.4	0.14

The strain energy release rate is found to be very low, consistent with the weak interface expected in these materials. The friction coefficient agrees well with the measurements of Parthasarathy, et al.[6] for fiber pushdown experiments in similar materials and the measurement of μ for graphite sliding on glass by Gupta.[9]

The calculated effective normal stress accounts for both the residual thermal mismatch stress and the fiber surface asperity effects, according to the following relation:[2]

$$\sigma_n^{eff} = \frac{-E_m E_f}{E_f(1+\nu_m) + E_m(1-\nu_f)} \left(\Delta\alpha \Delta T + \frac{A}{r} \right) \tag{6}$$

where A is the fiber surface asperity amplitude. The radial thermal expansion

[‖]Downhill Simplex Optimisation Method

coefficient for the SiC monofilament has been measured by Goettler and Faber[4] to be $2.63 \times 10^{-6}/°C$. Taking ΔT to be the strain point of the glass minus ambient, and with a thermal expansion coefficient for the borosilicate glass of $3.5 \times 10^{-6}/°C$, the residual normal stress for this system is calculated from the first term of Equation 6 to be 20.7 MPa. The fiber surface asperity amplitude can then be determined from Equation 6. The asperity amplitudes calculated for data sets 1 and 2 are 0.26 and 0.25μm, respectively. These values agree very well with the independent measurements of Jero, et al.[10] who used an optical interference technique to directly measure the surface roughness. Their results indicate that the average fiber surface asperity amplitude is 0.09–0.18μm with larger asperities up to 0.36μm.

The frictional pullout portion of the load-displacement curve can be used to check the consistency of the fitted parameters obtained from the progressive debonding portion of the data. The post-fiber-fracture embedded length is related to μ, P^*, and the applied load P_a by the following relation:[2]

$$l_e = \frac{r}{2\mu k} \ln\left(\frac{P^*}{P^* - P_a}\right) \tag{7}$$

If the friction coefficient is taken to be equal to that measured from the progressive debonding data, the effective normal stress at the debonded sliding interface can be calculated. The embedded length during pullout is approximately equal to the final pullout length, measured after the test is complete, minus the matrix crack opening displacement. The measured pullout lengths and the P^* values calculated from the data immediately following fiber fracture are reported in Table 2. The P^* values obtained from the parameter fit of the progressive debonding are shown for comparison. As P^* is a direct measure of the effective normal stress, very good agreement is found in the interfacial parameters obtained from the progressive debonding data and the frictional pullout data.

Table 2: Post-fiber-fracture analysis

Data Set	Pullout Length (μm)	P^*_{prog} (N)	P^*_{frict} (N)
1	762	109.4	104.9
2	728	116.5	100.4

SUMMARY

A novel modified single-fiber pullout technique was utilized to investigate the fiber debonding and sliding behavior in a model ceramic composite system. Progressive debonding was observed, consistent with recent analytical models. The morphology of the fiber surface appears to have a significant effect on the fiber sliding behavior, both during progressive debonding prior to fiber failure and during frictional fiber pullout following fiber fracture.

The Kerans and Parthasarathy analysis[2] was used to extract interfacial parameters from the progressive debonding portion of single load-displacement curves. The data from these experiments agree with the model predictions, and the interfacial parameters calculated from the experimental data are consistent with independent measurements reported in the literature.

References

1. A.G. Evans and D.B. Marshall, "The Mechanical Behavior of Ceramic Matrix Composites", *Acta Metall.*, **37**[10] 2567–83 (1989).
2. R.J. Kerans and T.A. Parthasarathy, "Theoretical Analysis of the Fiber Pull-out and Pushout Tests", *J. Am. Ceram. Soc.*, **74**[7] 1585–96 (1991).
3. C.W. Griffin, et al., "Evaluation of Interfacial Properties in Borosilicate SiC Composites Using Pull-out Tests", *Ceram. Eng. Sci. Proc.*, **12**[7-8] 671–78 (1988).
4. R.W. Goettler and K.T. Faber, "Interfacial Shear Stresses in SiC and Al_2O_3 Fiber-Reinforced Glasses", *Ceram. Eng. Sci. Proc.*, **9**[7-8] 861–70 (1988).
5. D.B. Marshall, "An Indentation Method for Measuring Matrix/Fiber Frictional Stresses in Ceramic Composites", *J. Am. Ceram. Soc.*, **67**[12] C259–60 (1984).
6. T.A. Parthasarathy, P.D. Jero, and R.J. Kerans, "Extraction of Interfacial Properties from a Fiber Push-out Test", *Scr. Metall. Mater.*, **25** 2457–62 (1991).
7. P.D. Jero and R.J. Kerans, "The Contribution of Interfacial Roughness to Sliding Friction of Ceramic Fibers in a Glass Matrix", *Scr. Metall. Mater.*, **24** 2315–18 (1990).
8. E.P. Butler, J. E. R. Fuller, and H.M. Chan, "Interface Properties for Ceramic Composites From a Single-Fiber Pull-Out Test", in Interfaces in Composites, edited by C. G. Pantano and E. J. H. Chen, MRS Symp. Proc., **170** (MRS, Pittsburgh, PA, 1990) 17–24.
9. P.K. Gupta, "Simple Method for Measuring the Friction Coefficient of Thin Fibers", *J. Am. Ceram. Soc.*, **74**[7] 1692–94 (1991).
10. P.D. Jero, R.J. Kerans, and T.A. Parthasarathy, "Effect of Interfacial Roughness on the Frictional Stress Measured Using Pushout Tests", *J. Am. Ceram. Soc.*, **74**[11] 2793–801 (1991).

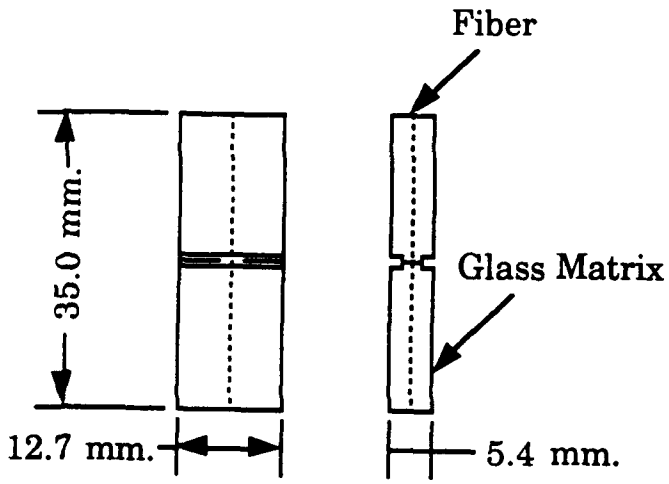

Figure 1: Modified single-fiber pullout specimen geometry.

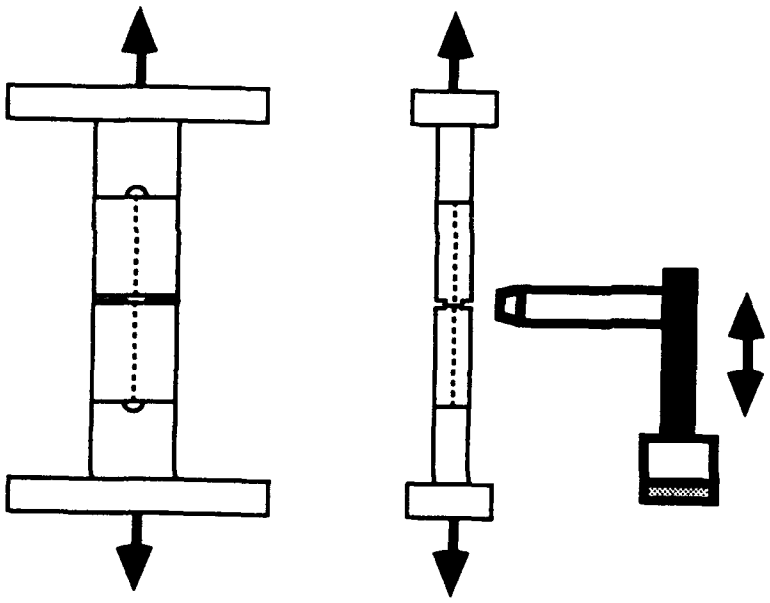

Figure 2: Modified single-fiber pullout test setup.

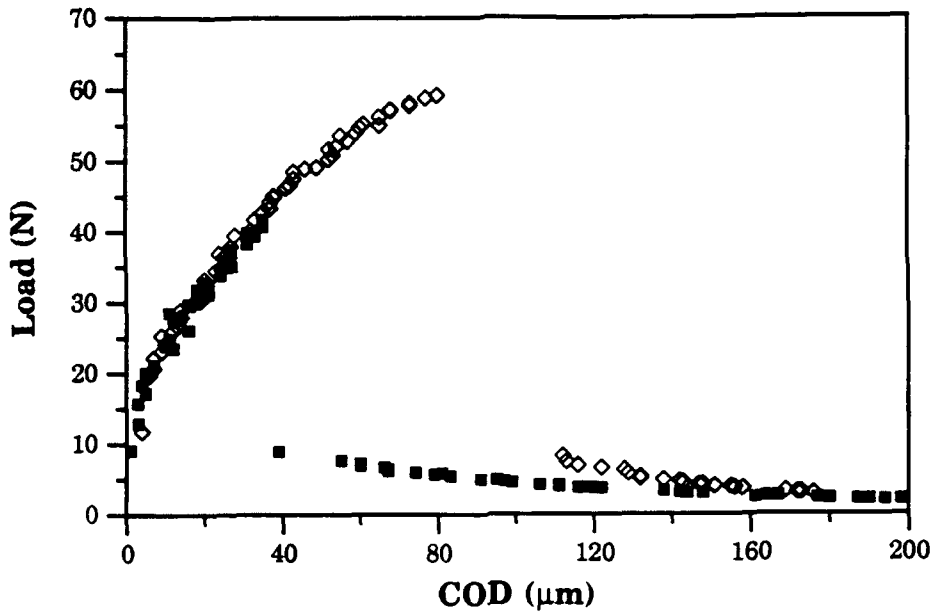

Figure 3: Load-displacement data for the modified single fiber pullout test.

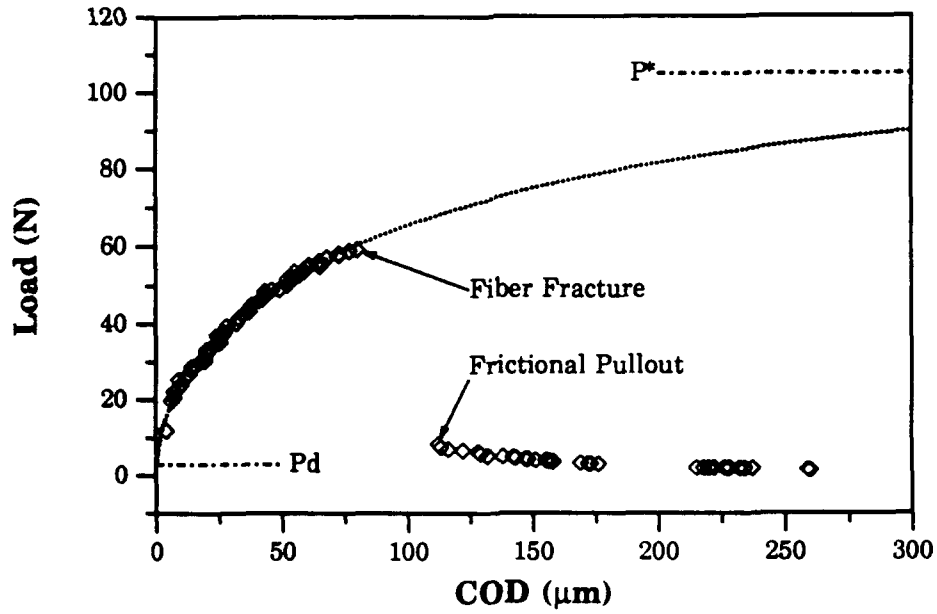

Figure 4: Application of the Kerans and Parthasarathy model[2] to the experimental load-displacement data.

TENSILE FRACTURE OF FIBER-REINFORCED COMPOSITES: INFLUENCE OF THERMAL RESIDUAL EFFECT

W. B. Tsai and T. Mura
Department of Civil Engineering and Theoretical and Applied mechanics,
Northwestern University, Evanston, IL 60208, U.S.A.

Abstract-The inclusion model is used to analyze the tensile fracture of fiber-reinforced brittle-matrix composites containing many unidirectionally aligned continuous fibers with uniform strength. During the debonding of fiber-matrix interfaces, the fibers slide against the friction which is caused by Poisson effect and thermal expansion mismatch. In general, three fracture mechanisms including interfacial debonding, matrix cracking and fiber failure may occur in some sequence. The sequences are strongly influenced by the thermal residual effect due to temperature change ΔT. The analysis provides explicit crack length/applied stress relation for each mechanism. Fracture maps are constructed to analyze the influence of thermal residual effect on the fracture sequences and final composite strength. Two categories of fracture transitions are defined analytically for the large crack limit.

1. INTRODUCTION

In a brittle matrix composite containing unidirectionally aligned fibers, three fracture mechanisms are commonly expected, including debonding of fiber-matrix interfaces, matrix cracking and fiber failure. Using the standard fracture mechanics approach, Marshall et al. (1985, 1987), Budiansky et al. (1986) and McCartney (1987) analyzed the influence of material parameters such as frictional shear stress, fiber strength and interfacial fracture toughness on the fracture mechanisms. The mechanics of the crack bridged by fibers can be also analyzed by the inclusion method (Mura, 1987). Mori and Mura (1984, 1988) investigated the effect of fibers on the arrest of a crack for the complete bridging and complete sliding cases. Yang et al. (1991) extended this analysis to the case of partially debonded fiber-matrix interfaces assuming a constant

friction was present in the debond region. Tsai and Mura (1991) further considered the origin of friction which is the Poisson effect and thermal expansion mismatch. Similar subjects were studied by Gao et al. (1988), Sigl and Evans (1989), Hutchinson and Jensen (1990). In this paper, the authors emphasize the influence of thermal residual effect on each fracture mechanism. For instance, the threshold stress for debonding initiation increases as the thermal residual effect is reduced. The reason will be discussed later.

The present analysis also provides the fracture criterion and the unique relation between crack length and critical applied stress for each kind of fracture mechanism. Consequently, it is possible to construct the fracture maps shown in Fig.8 and Fig.9. Sequences of fracture mechanisms and final composite strength are easily obtained by drawing crack extension paths in the fracture maps. Also, the large crack limit will be discussed at the end of this paper. Two categories of fracture transitions will be defined and critical conditions are given in terms of material properties.

2. MODEL AND ANALYSIS

2.1 Inclusion model and stress analysis

Consider a composite containing many aligned and randomly distributed continuous fibers of radius r and average spacing λ. Perpendicular to the fiber direction is a matrix crack (Fig.1). The shape of the matrix crack is approximated by a thin oblate spheroid as

$$\Omega_0: \quad \frac{X_1^2+X_2^2}{a^2}+\frac{X_3^2}{c_0{}^2}\le 1 \quad , \quad \frac{c_0}{a}<<1. \tag{1}$$

a is the radius of a penny shape crack. c_0 is the half of the fictitious thickness of the crack. The absolute value of c_0 does not appear in the relevant equations to be derived later. The cross section of a fiber in the crack is also approximated as

$$\Omega: \quad \frac{X_1^2+X_2^2}{r^2}+\frac{X_3^2}{c_0{}^2}\le 1 \quad , \quad \frac{c_0}{r}<<1. \tag{2}$$

When an uniform tensile stress σ_A at infinity is applied in the direction normal to the crack surface, the eigenstrain ε_{33}^* for the equivalent inclusion method is introduced to simulate the bridged crack. Specially

$$\varepsilon_{33}^* = \varepsilon_P \qquad \text{in } \Omega_0 - \Omega's \tag{3}$$

$$\varepsilon_{33}^* = \alpha\varepsilon_P \qquad \text{in } \Omega's. \tag{4}$$

Here, α is the parameter characterizing the frictional sliding of fibers along the fiber-matrix interfaces. There are two extreme cases illustrating the physical meaning of α. First, complete bridging ($\alpha = 0$, no sliding of fibers) occurs. Second, complete sliding of fibers ($\alpha = 1$) takes place. The general expression of α will be derived later when we discuss the crack wake frictional sliding of fibers. According to the averaging processes employed by Mori et al. (1983), one obtains the average internal stresses in $\Omega_0 - \Omega's$ and $\Omega's$, given as

$$\langle\sigma_{33}\rangle_{\Omega_0 - \Omega's} = \frac{-\bar{\mu}\pi c_0\varepsilon_P}{2(1-\bar{\nu})a} - \frac{f\bar{\mu}\pi c_0(1-\alpha)\varepsilon_P}{2(1-\bar{\nu})r} \tag{5}$$

$$\langle\sigma_{33}\rangle_{\Omega's} = \frac{-\bar{\mu}\pi c_0\varepsilon_P}{2(1-\bar{\nu})a} + \frac{\bar{\mu}\pi c_0(1-\alpha)\varepsilon_P}{2(1-\bar{\nu})r} - \frac{f\bar{\mu}\pi c_0(1-\alpha)\varepsilon_P}{2(1-\bar{\nu})r}. \tag{6}$$

Here, < > denotes the average defined in the respective domain. $\bar{\mu}$ is the shear modulus and $\bar{\nu}$ is the Poisson ratio of the composite. f is the volume fraction of fibers and equals to $\pi r^2/\lambda^2$. To satisfy the traction free condition on the crack surface

$$\sigma_A + \langle\sigma_{33}\rangle_{\Omega_0 - \Omega's} = 0, \tag{7}$$

ε_p is obtained as

$$\varepsilon_P = \frac{2(1-\bar{\nu})\sigma_A\, a}{\bar{\mu}\pi c_0\left\{1 + (1-\alpha)\frac{a}{r}f\right\}}. \tag{8}$$

The total stress of the fiber in $\Omega's$ (bridged domain), sum of the external and internal stresses, is written as

$$\sigma_T = \sigma_A + \langle\sigma_{33}\rangle_{\Omega's}. \tag{9}$$

Using Eq.(5), (8) and (9), the total stress (bridging stress) is given below:

$$\sigma_T = \frac{\sigma_A (1-\alpha)\frac{a}{r}}{1+(1-\alpha) f \frac{a}{r}}. \tag{10}$$

2.2 Analysis of frictional sliding of fibers (determination of a)

In this section, the authors investigate the mechanism of frictional sliding of fibers to determine α. For simplicity, one considers a rod-cylinder model consisting of a rod (fiber) embedded in a cylinder (matrix), Fig.2. In the debond region with length l_d, there exists a frictional shear stress τ which is proportional to the normal pressure p at the interface. Through the detail derivation in Appendix A, the stress fields in the debond region are evaluated as follows:

$$\sigma_{33}^f = c\left[\exp\left(\beta x_3/r\right)-1\right]+\sigma_T \tag{11}$$

$$\sigma_{33}^m = -c\left[\exp\left(\beta x_3/r\right)-1\right]\left(\frac{f}{1-f}\right) \tag{12}$$

$$\tau = -\left(\beta c/2\right)\exp\left(\beta x_3/r\right) \tag{13}$$

$$p = \left(\beta c/2\mu\right)\exp\left(\beta x_3/r\right) \tag{14}$$

where

$$\beta = 2\mu\eta\zeta$$

$$c = \left[\Delta\Omega + \left(\nu_f \sigma_T/E_f\right)\right]\eta^{-1}.$$

η and ζ are expressed in terms of Young's modulus E_f, E_m, Poisson ratio ν_f, ν_m and fiber volume fraction f in Appendix A. μ is the friction coefficient. $\Delta\Omega$ is the residual thermal strain defined as

$$\Delta\Omega = \left(\alpha_m - \alpha_f\right)\Delta T \tag{15}$$

where α_f and α_m are the thermal expansion coefficients of fiber and matrix respectively, $\Delta T(<0)$ is the temperature change from the stress-free temperature of matrix to the operating temperature. The interface is subject to compression only when p is negative. According to Eq.(14), following condition must be satisfied

$$\Delta\Omega + \left(\nu_f \sigma_T / E_f\right) < 0. \tag{16}$$

Through the whole paper, condition (16) is always assumed. Now, one can calculate the crack opening at the bridged domain due to the elastic extension of the fiber out of the matrix. The crack opening displacement is defined as

$$\delta = 2\left(u_f - u_m\right)_{/x_3 = 0}. \tag{17}$$

One can integrate ε_f and ε_m given in Appendix B from 0 to l_d such that u_f and u_m at the crack plane are obtained. The crack opening displacement is found to be

$$\delta = \frac{rc}{E_f \mu \zeta}\left[\exp\left(\beta l_d / r\right) - 1\right] + 2l_d\left[\frac{\sigma_T}{E_f} - \left(\frac{1}{E_f} + \frac{f}{E_m(1-f)}\right)c - \Delta\Omega\right]. \tag{18}$$

From the eigenstrain approach, the crack opening is defined as

$$\delta = 2c_0 \alpha \varepsilon_p = 4r\left(\frac{1-\bar{\nu}}{\bar{\mu}\pi}\right)\left(\frac{\alpha}{1-\alpha}\right)\sigma_T \tag{19}$$

at the bridged domain Ω_s. By setting Eq.(18) equal to Eq.(19), α is determined and expressed as

$$\alpha = \left\{1 + \frac{2(1-\bar{\nu})}{\bar{\mu}\pi}\sigma_T\left[\left(\frac{\sigma_T}{E_f} - \left(\frac{1}{E_f} + \frac{f}{E_m(1-f)}\right)c - \Delta\Omega\right)\frac{l_d}{r} + \frac{c}{2E_f \mu \zeta}\left[\exp\left(\beta l_d / r\right) - 1\right]\right]^{-1}\right\}^{-1}. \tag{20}$$

It is clear that $\alpha = 0$ as $l_d = 0$ (no sliding), $\alpha = 1$ as $l_d \to \infty$ (complete sliding for a continuous fiber).

2.3 Analysis of debond length

The debond length l_d be determined by using the energy balance approach. If the debond crack extends by an incremental amount dl at

constant σ_T, several different kinds of energy change will occur and reach to the equilibrium state. The strain energy is increased by dE_s, work is done by traction stress σ_T, with magnitude dw_T, frictional energy dw_f is dissipated, debonding energy dw_d is absorbed during interfacial debonding. The energy balance condition, at $l = l_d$, can be formulated as below:

$$dw_T - dE_s - dw_d - dw_f = 0. \tag{21}$$

Dividing each term by the incremental debond length dl, one can change Eq.(21) into the following expression:

$$\frac{dw_T}{dl} - \frac{dE_s}{dl} = \frac{dw_d}{dl} + \frac{dw_f}{dl}. \tag{22}$$

Each energy term is derived in Appendix B. For small exponent index $\beta l_d/r$, Eq.(22) is used to obtain the approximate value of l_d:

$$l_d \cong \frac{r}{\beta}\left[\frac{g(\sigma_\tau) - \left(2E_f G_s/r\right)}{h(\sigma_\tau)}\right] \tag{23}$$

where

$$g(\sigma_\tau) = D_2 \sigma_T{}^2 + D_1 \sigma_T$$

$$D_2 = \frac{1}{2} - 2\eta\zeta v_f + \frac{\zeta v_f^2}{E_f}$$

$$D_1 = E_f \Delta\Omega\left[-1 - 2\eta\zeta + \frac{\zeta v_f}{E_f} + \frac{\alpha_f}{2\left(\alpha_f - \alpha_m\right)}\right]$$

$$h(\sigma_\tau) = \tilde{D}_2 c^2 + \tilde{D}_1 c\sigma_T + \tilde{D}_0 c$$

$$\tilde{D}_2 = \rho - \eta\zeta\left[v_f + \frac{v_m E_f}{E_m}\left(\frac{f}{1-f}\right)^2\right]$$

$$\tilde{D}_1 = -1 + 2\eta^2\zeta E_f - \frac{fE_f}{(1-f)E_m}$$

$$\tilde{D}_0 = \frac{E_f \Delta T}{2}\left[\left(\frac{2-3f}{1-f}\right)\alpha_m - \alpha_f\right].$$

Here, ρ is defined in Appendix B. Furthermore, substituting Eq.(23) into Eq.(20), one can obtain the approximate value of α for small $\beta l_d/r$ as

$$\alpha \cong 1-\left\{1+\frac{\bar{\mu}\pi}{4\mu\eta\zeta(1-\bar{\nu})\sigma_T}\left[\frac{g(\sigma_\tau)-\left(2E_f G_s/r\right)}{h(\sigma_\tau)}\right]\left(\frac{\sigma_T}{E_f}-2\eta^2\zeta c-\Delta\Omega\right)\right\}^{-1}. \tag{24}$$

In Eq.(24), α is a function of bridging stress σ_T and several material constants.

2.4 Energy calculation for a bridged crack

2.4.1 Elastic and external potential energies

In order to calculate the energy release rate during the crack growth, the Gibbs free energy of the composite under an applied stress is evaluated when the configuration of Fig.1 is simulated by inclusion Ω_0 and inclusions Ω_s. Also, the matrix is approximated by the homogeneous medium with the composite moduli $\bar{\mu}$ and $\bar{\nu}$. According to the definition (Mura, 1987), the Gibbs free energy is

$$F=-\frac{1}{2}\int_{\Omega_0}\sigma_{33}\varepsilon_{33}^{*}\,dv-\int_{\Omega_0}\sigma_A\varepsilon_{33}^{*}\,dv \tag{25}$$

where σ_{33} is given by Eq.(5) and Eq.(6), ε_{33}^{*} is given by Eq.(3) and Eq.(4). Substituting them into Eq.(25), F is evaluated as

$$F=-\frac{4(1-\bar{\nu})a^3\left(\sigma_A\right)^2}{3\bar{\mu}}\frac{1+\left(1-\alpha^2\right)\frac{a}{r}f}{\left[1+(1-\alpha)\frac{a}{r}f\right]^2}. \tag{26}$$

By definition, the energy release rate of a crack is written as

$$G=-\frac{\partial F}{\partial \pi a^2} \tag{27}$$

which is evaluated below:

$$G=\frac{G_0}{3\left[1+(1-\alpha)\frac{a}{r}f\right]^3}\left\{\begin{array}{l}3+\left[(1-\alpha)(5+4\alpha)+2(1-\alpha)a\frac{\partial\alpha}{\partial a}\right]\frac{a}{r}f\\+\left[2(1-\alpha)^2(1+\alpha)+2(1-\alpha)a\frac{\partial\alpha}{\partial a}\right]\left(\frac{a}{r}f\right)^2\end{array}\right\} \tag{28}$$

where

$$G_0=2(1-\bar{v})(\sigma_A)^2 a/\pi\bar{\mu}.$$

G_0 is the energy release rate of a penny-shaped crack in the homogeneous medium without fibers. $(\partial\alpha/\partial a)$ can be evaluated by the following procedures: First, one can substitute Eq.(24) into Eq.(10) and obtain

$$a\cong\frac{r\sigma_T}{\sigma_A-f\sigma_T}\left\{1+\frac{\bar{\mu}\pi}{4\mu\eta\zeta(1-\bar{v})\sigma_T}\left[\frac{g(\sigma_\tau)-\left(2E_fG_s/r\right)}{h(\sigma_\tau)}\right]\left(\frac{\sigma_T}{E_f}-2\eta^2\zeta c-\Delta\Omega\right)\right\} \tag{29}$$

Second, $(\partial\alpha/\partial a)$ is equal into $(\partial\alpha/\partial\sigma_T)/(\partial a/\partial\sigma_T)$. Using Eq.(24) and Eq.(29) to obtain $(\partial\alpha/\partial\sigma_T)$ and $(\partial a/\partial\sigma_T)$ individually, one can calculate $(\partial\alpha/\partial a)$ analytically or numerically.

2.4.2 Dissipation energy and debonding energy

The crack opening in Ω_s is achieved when the fiber extends out of the matrix. This is an inelastic deformation, confirming to the definition of eigenstrain $\alpha\varepsilon_p$. Before the fiber begins to slide, interfacial debonding must initiate at first. Therefore, dissipation energy due to the work against friction and debonding energy needed to create new surface at the interface can contribute to the increase of crack resistance. One can define the total dissipation energy and the total debonding energy as follows:

$$W_{dis.}=2N\left[2\pi r\int_0^{l_d}\tau\left(u_f-u_m\right)dx_3\right] \tag{30}$$

$$W_{deb.}=2N\left(2\pi r l_d G_s\right) \tag{31}$$

where

$$N = \frac{\pi a^2}{\lambda^2} = f\frac{a^2}{r^2}.$$

N is the amount of fibers bridging the matrix crack. $2N$ represents the amount of debond lengths on the both sides of the matrix crack. Using Eq.(B7)and Eq.(B8), one obtains

$$\frac{\partial W_{dis.}}{\partial \pi a^2} \cong \frac{f\beta}{rE_f}\left\{I(\sigma_T)\left[(l_d)^2 + al_d\left(\frac{\partial l_d}{\partial a}\right)\right] + \frac{a}{2}(l_d)^2\left(\frac{\partial I(\sigma_T)}{\partial a}\right)\right\} \tag{32}$$

$$\frac{\partial W_{deb.}}{\partial \pi a^2} \cong \frac{2fG_s}{r}\left[2l_d + a\left(\frac{\partial l_d}{\partial a}\right)\right] \tag{33}$$

where

$$I(\sigma_T) = \left(\rho c^2 - c\sigma_T + cE_f\Delta\Omega\right). \tag{34}$$

One can do $(\partial l_d/\partial\sigma_T)$, $(\partial a/\partial\sigma_T)$ and $(\partial I(\sigma_T)/\partial\sigma_T)$ using Eq.(23), (29) and (34). Then, $(\partial l_d/\partial a)$ and $(\partial I(\sigma_T)/\partial a)$ are calculated by applying the chain rules of differentiation. The total crack resistance is defined as

$$R = G_c + \frac{\partial W_{dis.}}{\partial \pi a^2} + \frac{\partial W_{deb.}}{\partial \pi a^2} \tag{35}$$

where G_c is the inherent fracture toughness of the matrix, the second and third terms on the right-hand side of Eq.(35) are the additional crack resistances due to frictional sliding and interfacial debonding, respectively.

3. DISCUSSION

In this section, we are going to discuss how the thermal residual effect influences fracture mechanisms such as interfacial debonding, fiber failure and matrix cracking. Following parameters are used for numerical calculation: $E_f = 580\,GPa$, $E_m = 410\,GPa$, $\nu_f = 0.23$, $\nu_m = 0.19$, $\alpha_f = 4.8\times10^{-6}$, $\alpha_m = 8.9\times10^{-6}$, $f = 0.2$, $\mu = 0.1$, $r = 0.4\,\mu m$, $G_c = 30\,J/m^2$.

3.1 Fracture mechanisms

3.1.1 Interfacial debonding

It follows from Eq.(23) that $l_d \to 0$ as σ_T approaches to Σ. Accordingly, Σ is a threshold stress for debonding initiation. One can obtain Σ by solving the following equation:

$$g(\sigma_T) - \frac{2E_f G_s}{r} = 0 \tag{36}$$

which has the solution

$$\sigma_T = \Sigma = \frac{1}{2D_2}\left[-D_1 + \sqrt{\left(D_1\right)^2 + D_2 \frac{8E_f G_s}{r}}\right]. \tag{37}$$

In Fig.3, it clearly shows that Σ increases as G_s increases for the same ΔT. Also, for the same G_s, Σ decreases as $|\Delta T|$ increases. The reason is before debonding, when $|\Delta T|$ becomes larger, the fiber is under higher residual compression in x_3 direction and the surrounding matrix is under higher residual tension. After debonding, the fiber tends to extend and matrix tends to shrink naturally because of relaxation of axial residual stresses. So, debonding initiation is easier to occur. The same tendency was also predicted by Hsueh (1991) for the case of isotropic thermal expansion coefficients of the fiber. Eq.(37) reconfirms the previous conclusion that Σ is lower as r is larger (Yang et al., 1991). Replacing σ_T in Eq.(10) by Σ and letting $\alpha = 0$ for $l_d \to 0$, one obtains

$$\frac{a}{r} = \left(\sigma_A / \Sigma - f\right)^{-1} \tag{38}$$

where Σ is a function of ΔT and G_s. For given ΔT and G_s , curve of Eq.(38), debonding initiation, is shown in Fig.4. As $a/r >> 1$, σ_A has an asymptotic value:

$$\sigma_A = f\Sigma. \tag{39}$$

If the Poisson effect and thermal expansion mismatch are ignored by setting $\nu_f = 0$ and $\Delta T = 0$, one obtains $D_2 = 1/2$ and $D_1 = 0$. The threshold stress is expressed as

$$\Sigma = \sqrt{\frac{4E_f G_s}{r}} \tag{40}$$

which is exactly identical to that of the frictionless case studied by Outwater and Murphy (1969).

3.1.2 Fiber failure

It is assumed that fibers have the averaged uniform strength S. Fiber failure occurs when bridging stress reaches fiber strength. i.e.

$$\sigma_T = S. \tag{41}$$

Substituting Eq.(41) into Eq.(10), one obtains

$$\frac{a}{r} = \left(\sigma_A / S - f\right)^{-1}\left(1 - \alpha_s\right)^{-1} \tag{42}$$

where

$$\alpha_s = \begin{cases} 0 \ , & S \le \Sigma \\ \alpha(S) \ , & \Sigma < S < -E_f \Delta\Omega / v_f \end{cases}.$$

Replacing σ_T by S, $\alpha(S)$ is obtained from Eq.(24). Fig.5 is the plot of Eq.(42) for two different ΔT and S . Obviously, as S increases, σ_A must increase to cause fiber failure for the same crack length at the same ΔT. It is worth noting that there is a critical value of strength S_c to separate the opposite effects of ΔT through α_s in Eq.(42). As $S < S_c$, larger $|\Delta T|$ (larger α_s) causes fiber failure at larger applied stress. As $S > S_c$, larger $|\Delta T|$ (smaller α_s) results in fiber failure at smaller applied stress. Only when $S = S_c$, these two ΔT has the same effect on fiber failure mechanism. Fig.6 shows the relation between α_s and S for two different ΔT. From Eq.(42), one obtains the asymptotic value of σ_A as $a/r >> 1$:

$$\sigma_A = fS. \tag{43}$$

3.1.3 Matrix cracking

During crack growth equilibrium between energy release rate (crack driving force) and the crack resistance can be expressed by

$$G = R \tag{44}$$

Substituting Eq.(28) and Eq.(35) into Eq.(44), one obtains the critical value of σ_T causing matrix cracking. σ_T is expressed as a function of σ_A and a. This function can be substituted into Eq.(29) to plot the curve of matrix cracking in Fig.7. One can also prove numerically that

$$\frac{\partial G}{\partial \pi a^2} > \frac{\partial R}{\partial \pi a^2} \tag{45}$$

which is satisfied for any given critical applied stress σ_c. Therefore, the matrix crack always grows unstably at σ_c. As $a/r >> 1$, the asymptotic values of G and R are written below:

$$G_\infty = \frac{4(1-\bar{\nu})r(\sigma_A)^2}{3\pi\bar{\mu}f}\left(\frac{1+\alpha}{1-\alpha}\right) \tag{46}$$

$$R_\infty = G_c + \left(\frac{\partial W_{dis.}}{\partial \pi a^2}\right)_\infty + \left(\frac{\partial W_{deb.}}{\partial \pi a^2}\right)_\infty \tag{47}$$

where

$$\left(\frac{\partial W_{dis.}}{\partial \pi a^2}\right)_\infty \cong \frac{rf\beta}{E_f} I(\sigma_T)(l_d/r)^2 \tag{48}$$

$$\left(\frac{\partial W_{deb.}}{\partial \pi a^2}\right)_\infty \cong 4fG_s(l_d/r). \tag{49}$$

According to Eq.(29), as $a/r \to \infty$, σ_T approaches to σ_A/f. Therefore, one can replace σ_T by σ_A/f to obtain the asymptotic expressions of l_d, α and $I(\sigma_T)$ from Eq.(23), (24) and (34), respectively. Generally, fracture criterion, $G_\infty = R_\infty$, yields an algebraic equation for critical applied stress σ_c^∞. For complete bridging case ($\alpha = 0$), G and R can be evaluated analytically as follows:

$$G_{\alpha=0} = G_0 \frac{3+2fa/r}{3(1+fa/r)^2} \tag{50}$$

$$R_{\alpha=0} = G_c. \tag{51}$$

The asymptotic values of $G_{\alpha=0}$ and $R_{\alpha=0}$, respectively, are given by

$$\left(G_{\alpha=0}\right)_\infty = \frac{2G_0}{3fa/r} \tag{52}$$

$$\left(R_{\alpha=0}\right)_\infty = G_c. \tag{53}$$

Letting Eq.(52) be equal to Eq.(53), the asymptotic value of critical applied stress is given as

$$\left(\sigma_c^\infty\right)_{\alpha=0} = \sqrt{\frac{3\pi\bar{\mu}fG_c}{4(1-\bar{\nu})r}}. \tag{54}$$

For the given material parameters in the section of discussion, Fig.7 shows the curves of matrix cracking for two different ΔT. For the same crack length, smaller $|\Delta T|$ makes matrix cracking occur at slightly lower applied stress. One can not see much difference between these two curves. However, if one uses the curves of Eq.(38), Eq.(42) and matrix cracking to construct the fracture map as a (a/r *vs* σ_A) diagram, ΔT will show its influence on the crack extension paths and final failure mode of a composite. Fig.8 and Fig.9 are the fracture maps for larger and smaller $|\Delta T|$, respectively. For a large crack, path (A) shown in Fig.8 hits the curve of interfacial debonding first. Further increase of σ_A to point A will result in matrix cracking through whole matrix with no fiber failure. It is a non-catastrophic type of failure and a precursor of multiple matrix cracking causing larger nonlinear strain. The final composite strength can be defined as fS from Eq.(43). For smaller $|\Delta T|$ (smaller residual effect), path (A) shown in Fig.9 also passes the curve of interfacial debonding but increasing σ_A causes fiber failure directly without matrix cracking. It is a catastrophic type of failure. The composite strength is determined by point A obtained from Eq.(42). For intermediate and small cracks, path (B) and (C) in Fig.8 indicate that debonding, matrix cracking and fiber failure occur in sequence. The composite fails catastrophically at stress level of point B and C for intermediate and small cracks, respectively. Composite strength is predicted by substituting initial crack length into Eq.(44). In Fig.9, there is a critical point O associated with initial crack length a_0. For an intermediate crack, $a > a_0$, path (B) passes through the curve of debonding initiation and reaches the curve of fiber failure. It implies that the whole composite fails catastrophically at point B which is determined by Eq.(42). For a small crack, $a < a_0$, path (C) is similar to that in Fig.8. From the comparison between Fig.8 and Fig.9, one can discuss how ΔT changes the fracture mechanisms of a composite as well as the final composite strength for a given initial crack length. Generally, the fracture map is also useful to discuss the effects of other parameters such as G_s, μ, f and r on the fracture mechanisms of a composite.

3.2 Fracture transition for a large crack (a/r>>1)

Two categories of fracture transitions will be discussed in this section. The critical conditions of transitions are also defined.

3.2.1 Complete bridging versus interfacial debonding

Using Eq.(39) and Eq.(54), one can define a characteristic constant:

$$\kappa = \frac{4(1-\bar{\nu})rf\Sigma^2}{3\pi\bar{\mu}G_c}. \tag{55}$$

As $\kappa < 1$, debonding occurs at the interface before the matrix crack extends. As $\kappa > 1$, debonding can not occur during the matrix cracking through whole matrix. Therefore, $\kappa = 1$, it is the critical condition for interfacial debonding.

3.2.2 Catastrophic failure versus non-catastrophic failure

First, $\kappa < 1$, non-catastrophic failure is predicted under the condition:

$$f\Sigma < \sigma_c^{\infty} < fS. \tag{56}$$

Using inequality (56), one can find the range of certain parameter such as ΔT, f, r et al. to facilitate non-catastrophic type of failure. Second, $\kappa > 1$, the following inequality

$$\left(\sigma_c^{\infty}\right)_{\alpha=0} < fS \tag{57}$$

ought to be satisfied for non-catastrophic failure of a composite. Inequality (57) can be rewritten as

$$\sqrt{\frac{3\pi\bar{\mu}fG_c}{4(1-\bar{\nu})r}} < fS. \tag{58}$$

It is noticeable that ΔT does not involve in inequality (58). It means if interfacial debonding does not occur, residual thermal effect has no influence on the transition between catastrophic and non-catastrophic failure. Take the crack paths (A) in Fig.8 and Fig.9 as examples. For Fig.8, $\kappa = 0.28$. For Fig.9, $\kappa = 0.50$. Both values of κ are smaller than one so that interfacial debonding always initiates before the matrix crack extends. For Fig.8, $f\Sigma = 0.82GPa$, $\sigma_c^{\infty} = 1.06GPa$, and $fS = 1.10GPa$ satisfy inequality (56). For Fig.9, $f\Sigma = 1.08GPa$, $\sigma_c^{\infty} = 1.03GPa$ and $fS = 1.10GPa$ do not satisfy

inequality (56). Therefore, non-catastrophic failure is only expected for path (A) in Fig.8.

4. CONCLUSION

The thermal residual effect on the fracture mechanisms including interfacial debonding, matrix cracking and fiber failure are investigated in this paper. Combining Eshelby's inclusion method and fracture criteria of fracture mechanics, the fracture mechanisms are governed by Eq.(38) for debonding, Eq.(42) for fiber failure and Eq.(44) for matrix cracking. The fracture maps like Fig.8 and Fig.9 are used to analyze the crack extension paths and final composite strength. Comparing Fig.8 with Fig.9, one can conclude that ΔT has the strong influence on the crack extension paths and final composite strength. For the given material parameters in the section of discussion, decreasing $|\Delta T|$ (decreasing thermal residual effect) undergoes the transition from non-catastrophic type to catastrophic type of failure for a large crack in a fiber-reinforced brittle matrix composite. In general, the conditions of fracture transitions for a large crack are defined in section 3.2. These conditions may provide some useful guidelines to prevent undesirable fracture mechanisms when a composite is designed.

Acknowledgement-This research was supported by the U.S. Airforce, AFOSR-89-0269.

REFERENCES

Budiansky, B., Hutchinson, J. W. and Evans, A. G. (1986). Matrix fracture in fiber-reinforced ceramics. *J. Mech. Phys. Solids*, **34**, 167-189.

Gao, Y. C., Mai, Y. W. and Cotterell, B. (1988). Fracture of fiber-reinforced materials. *J. Appl. Math. Phys.* **39**, 550-572.

Hsueh, C.-H. (1991). Interfacial debonding and fiber pull-out stress of fiber-reinforced composites III: With residual radial and axial stresses. *Mater. Sci. Eng.* A, **145**, 135-142.

Hutchinson, J. W. and Jensen, H. M. (1990). Models of fiber debonding and pullout in brittle composites with friction. *Mech. Mater.* **9**, 139-163.

Marshall, D. B., Cox, B. N. and Evans, A. G. (1985). The mechanics of matrix cracking in brittle-matrix composites. *Acta metall.* **33**, 2013-2021.

Marshall, D. B. and Cox, B. N. (1987). Tensile fracture of brittle matrix composites: Influence of fiber strength. *Acta metall.* **35**, 2607-2619.

McCartney, L. N. (1987). Mechanics of matrix cracking in brittle-matrix fiber-reinforced composites. *Proc. R. Soc. Lond.* A **409**, 329-350.

Mori, T. and Mura, T. (1984). An inclusion model for crack arrest in fiber-reinforced materials. *Mech. Mater.* **3**, 193-198.

Mori, T., Saito, K. and Mura, T. (1988). An inclusion model for crack arrest in a composite reinforced by sliding fibers. *Mech. Mater.* **7**, 49-58.

Mori, T., Koda, M., Monzen, R. and Mura, T. (1983). Particle blocking in grain boundary sliding and associated internal friction. *Acta metall.* **31**, 275-283.

Mura, T. (1987). *Micromechanics of Defects in Solids*, 2nd edn. Matinus Nijhoff, Dordrecht.

Outwater, J. D. and Murphy, M. C. (1969). Paper 11c, 24th Annual Techn. *Conference on Composites. Soc. of Plastics Industry*, New York.

Sigl, L. S. and Evans, A. G. (1989). Effects of residual stress and frictional sliding on cracking and pull-out in brittle matrix composites. *Mech. Mater.* **8**, 1-12.

Tsai, W. B. and Mura, T. (1991). Fracture of a brittle matrix composite with strong long fibers. *Proc. of the Am. Soc. for Composites, Sixth Technical Conf.,* Albany, N.Y.. 538-547.

Yang, C. C., Tsai, W. B., Qin, S., Mura, T., Shibata, S. and Mori, T. (1991). Crack arrest by strong, long fibers in a brittle matrix composite. *Composites Engineering*. **1**, 113-125.

Appendix A

Consider the schematic of Fig.2. Assuming zero radial stress on the outside of the composite cylinder and using a modified shear lag model (Sigl and Evans, 1989), the stress fields satisfy the Lame' relationships:

$$\sigma_{rr}^{f} = \sigma_{\theta\theta}^{f} = p \quad , \quad p < 0 \tag{A1}$$

$$\sigma_{rr}^{m} = \left(\frac{p}{1-f}\right)\left[\left(r/r'\right)^2 - f\right] \quad , \quad f = \left(r/r_0\right)^2 \tag{A2}$$

$$\sigma_{\theta\theta}^{m} = \left(\frac{-p}{1-f}\right)\left[\left(r/r'\right)^2 + f\right] \tag{A3}$$

where r_0 is the radius of the cylinder composite, r is the fiber radius, r' is the distance from the center of the fiber to the point in the matrix and superscripts f and m denote fiber and matrix, respectively. The corresponding strains including thermal residual strains are

$$\varepsilon_{rr}^{f} = \varepsilon_{\theta\theta}^{f} = \left[\left(1-\nu_f\right)p - \nu_f \sigma_{33}^{f}\right]\frac{1}{E_f} + \alpha_f \Delta T \tag{A4}$$

$$\varepsilon_{33}^{f} = \left[\sigma_{33}^{f} - 2\nu_f p\right]\frac{1}{E_f} + \alpha_f \Delta T \tag{A5}$$

$$\varepsilon_{rr}^{m} = \left\{\frac{fp}{1-f}\left[\frac{1+\nu_m}{f}\left(\frac{r}{r'}\right)^2 + \left(1-\nu_m\right)\right] - \nu_m \sigma_{33}^{m}\right\}\frac{1}{E_m} + \alpha_m \Delta T \tag{A6}$$

$$\varepsilon_{\theta\theta}^{m} = \left\{\frac{-fp}{1-f}\left[\frac{1+\nu_m}{f}\left(\frac{r}{r'}\right)^2 - \left(1-\nu_m\right)\right] - \nu_m \sigma_{33}^{m}\right\}\frac{1}{E_m} + \alpha_m \Delta T \tag{A7}$$

$$\varepsilon_{33}^{m} = \left[\sigma_{33}^{m} + 2\nu_m\left(\frac{fp}{1-f}\right)\right]\frac{1}{E_m} + \alpha_m \Delta T. \tag{A8}$$

The requirement of continuity of radial displacements at the interface $r' = r$:

$$\varepsilon_{\theta\theta}^{f} = \varepsilon_{\theta\theta}^{m} \tag{A9}$$

yields the relation between normal pressure and axial stresses as

$$p = \zeta\left(-\frac{\nu_m}{E_m}\sigma_{33}^{m} + \frac{\nu_f}{E_f}\sigma_{33}^{f} + \Delta\Omega\right) \tag{A10}$$

where

$$\zeta = E_f\left[1-\nu_f+\frac{fE_f}{(1-f)E_m}\left(\frac{1+\nu_m}{f}+1-\nu_m\right)\right]^{-1}.$$

Assume that the interfacial friction is governed by Coulomb's friction law

$$\tau = -\mu p \tag{A11}$$

where μ is a constant friction coefficient. Moreover, the equilibrium equations in the x_3 direction must be satisfied within the debond region, $0 < x_3 < l_d$. They are written as

$$\frac{\partial \sigma_{33}^f}{\partial x_3} = -\frac{2}{r}\tau \tag{A12}$$

$$\frac{\partial \sigma_{33}^m}{\partial x_3} = \frac{2}{r}\left(\frac{f}{1-f}\right)\tau. \tag{A13}$$

Combining Eqs. (A10), (A11), (A12) and (A13), one obtains the following differential equation

$$\frac{\partial^2 \sigma_{33}^f}{\partial x_3{}^2} - (\beta/r)\frac{\partial \sigma_{33}^f}{\partial x_3} = 0 \tag{A14}$$

where

$$\beta = 2\mu\eta\zeta \quad , \quad \eta = \left[\nu_f + \frac{\nu_m f E_f}{(1-f)E_m}\right]\frac{1}{E_f}.$$

When boundary conditions

$$\sigma_{33}^f = \sigma_T\,, \quad \sigma_{33}^m = 0 \quad at \;\; x_3 = 0$$

are applied into Eq.(A14), the solutions are shown as below:

$$\sigma_{33}^f = c\left[\exp(\beta x_3/r) - 1\right] + \sigma_T \tag{A15}$$

$$\sigma_{33}^m = -c\left[\exp(\beta x_3/r) - 1\right]\left(\frac{f}{1-f}\right) \tag{A16}$$

$$\tau = -(\beta c/2)\exp(\beta x_3/r) \tag{A17}$$

where

$$c = \left(\frac{\nu_f}{E_f} \sigma_T + \Delta\Omega \right) \eta^{-1}.$$

Appendix B

Using the stresses and strains obtained in Appendix A, one can calculate strain energy E_s, energy dissipation w_f due to frictional sliding, debonding energy w_d absorbed by the interface and work w_T done by the traction stress σ_T. The elastic strain energies in the fiber and matrix are associated with σ_{33} and ε_{33}. This estimation gives

$$E_s = \frac{\pi r^2}{2}\int_0^l \left(\sigma_{33}^f \varepsilon_{33}^f + \sigma_{33}^m \varepsilon_{33}^m\right) dx_3 . \tag{B1}$$

The debonding energy is

$$w_d = 2\pi r l G_s \tag{B2}$$

where G_s is the fracture toughness of the interface.

The energy dissipation due to frictional sliding is

$$w_f = 2\pi r \int_0^l \tau\left(u_f - u_m\right) dx_3 . \tag{B3}$$

The work done by the traction stress is

$$w_T = \pi r^2 \sigma_T \left(u_f - u_m\right)_{x_3 = 0} \tag{B4}$$

where u_f and u_m are obtained by integrating ε_{33}^f and ε_{33}^m in Appendix A, respectively. For small $(\beta l/r)$, each energy term can be simplified as

$$E_s \cong \frac{\pi r^3}{2E_f}\left\{\begin{array}{l} \dfrac{l}{r}\left[\left(1-\dfrac{2\nu_f^2\zeta}{E_f}\right)\sigma_T^2 + \left(\dfrac{-2\nu_f\zeta}{E_f} + \dfrac{\alpha_f}{\alpha_m - \alpha_f}\right)E_f \Delta\Omega\sigma_T\right] \\ + \dfrac{\beta l^2}{2r^2}\left\{\dfrac{\beta}{\mu}\left[\nu_f + \nu_m \dfrac{E_f}{E_m}\left(\dfrac{f}{1-f}\right)^2\right]c^2 - 2c\sigma_T + cE_f\left(\dfrac{f\alpha_m}{1-f} - \alpha_f\right)\Delta T\right\} \end{array}\right\} \tag{B5}$$

$$w_T \cong \frac{\pi r^3}{E_f}\left\{\left[\left(1-2\eta\zeta\nu_f\right)\sigma_T^2 - \left(1+2\eta\zeta\right)E_f\Delta\Omega\sigma_T\right]\frac{l}{r} + \sigma_T c\left(\rho + 2E_f\eta^2\zeta\right)\frac{\beta l^2}{2r^2}\right\} \tag{B6}$$

$$w_f \cong \frac{\pi r^3}{E_f}\left(\rho c^2 - c\sigma_T + cE_f \Delta\Omega\right)\frac{\beta l^2}{2r^2} \quad , \quad \rho = 1 + \frac{fE_f}{(1-f)E_m} - 4E_f \eta^2 \zeta \tag{B7}$$

$$w_d = \frac{\pi r^3}{E_f}\left(\frac{2E_f G_s}{r}\right)\frac{l}{r} \tag{B8}$$

where $c, \beta, \eta \& \zeta$ are defined in Appendix A.

FIGURE LEGENDS

Fig.1 Inclusion model for the crack and the cross sections of fibers at the crack.

Fig.2 The rod-cylinder model: bridging stress σ_T is balanced by the frictional stress τ caused by the normal pressure p acting at the debond interface.

Fig.3 Threshold stress Σ for debonding plotted as a function of interfacial fracture toughness G_s for two different temperature change ΔT.

Fig.4 Curves of debonding initiation plotted in a crack length vs applied stress diagram.

Fig.5 Curves of fiber failure plotted in a crack length vs applied stress diagram.

Fig.6 Sliding parameter α_s plotted as a function of fiber strength.

Fig.7 Curves of matrix cracking plotted in a crack length vs applied stress diagram.

Fig.8 Fracture map for $\Delta T = -980\,^0c$. Dash lines (A), (B) and (C), respectively, represent the extension paths for large, intermediate and small cracks.

Fig.9 Fracture map for $\Delta T = -490\,^0c$. Critical point O is associated with initial crack length a_0.

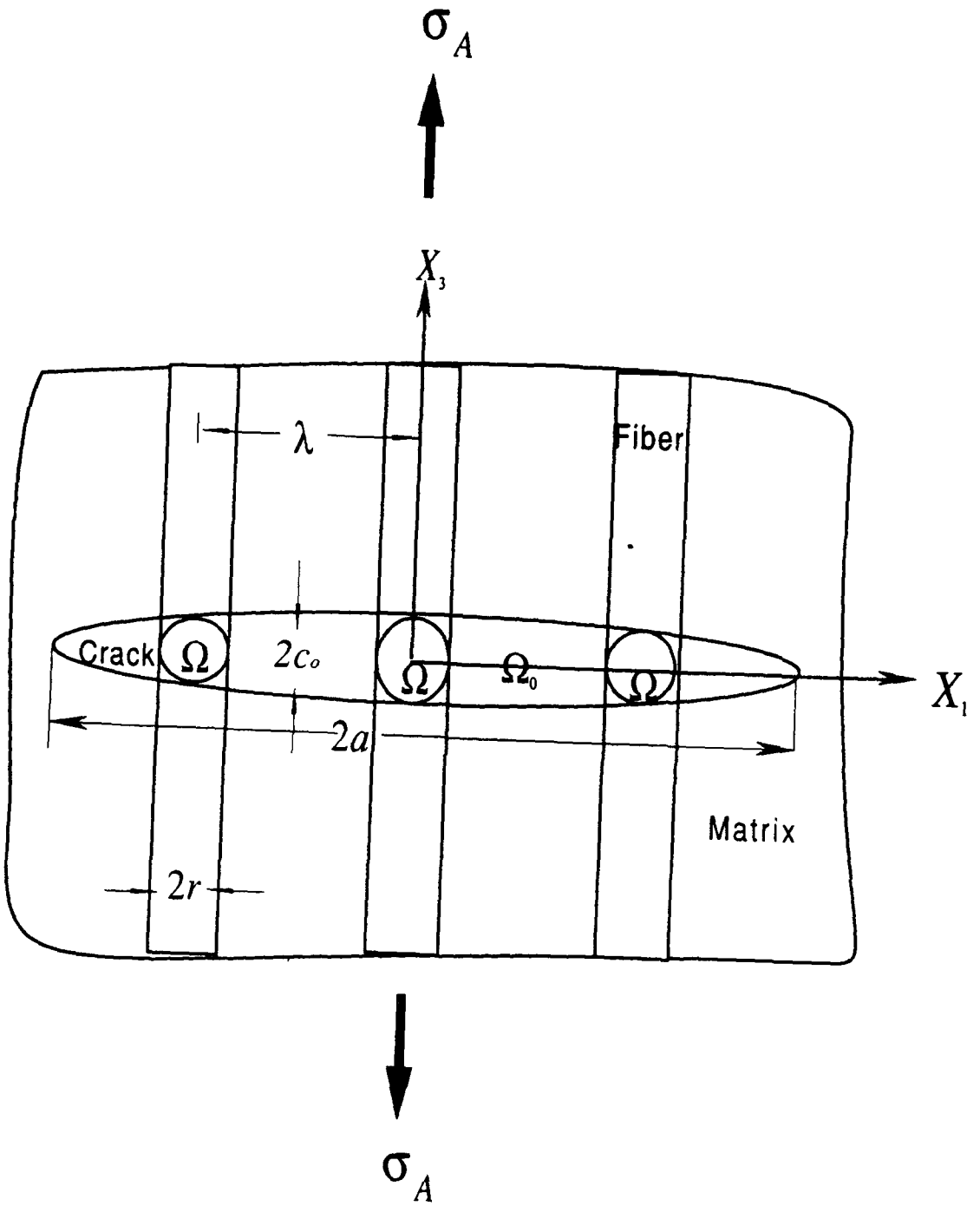

Fig.1

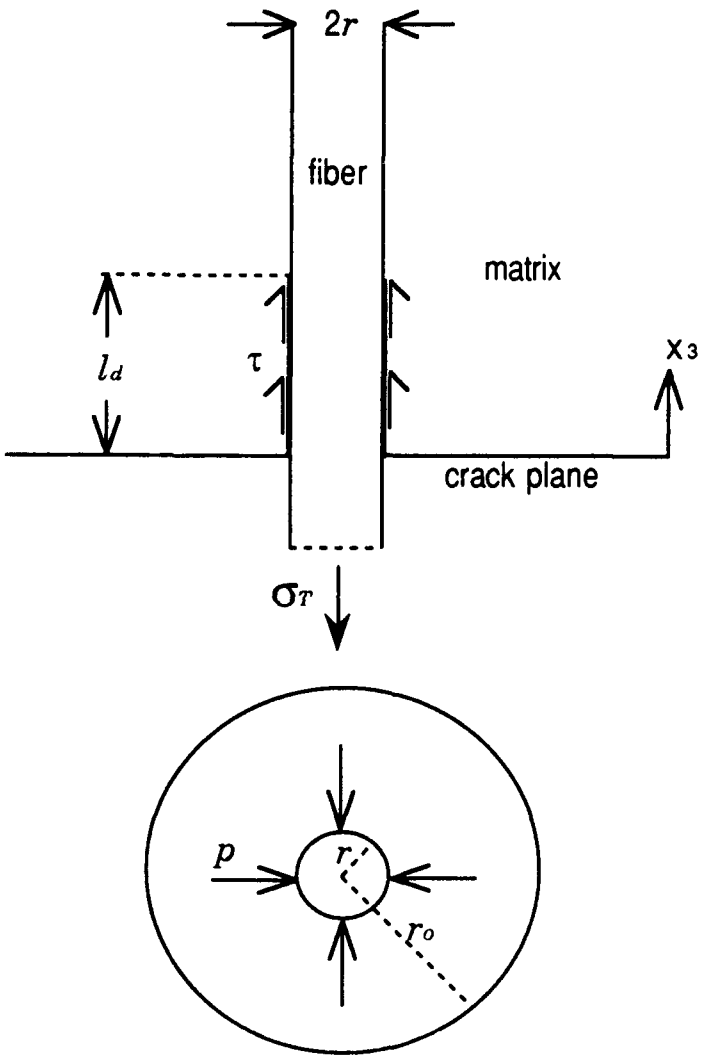

Fig.2

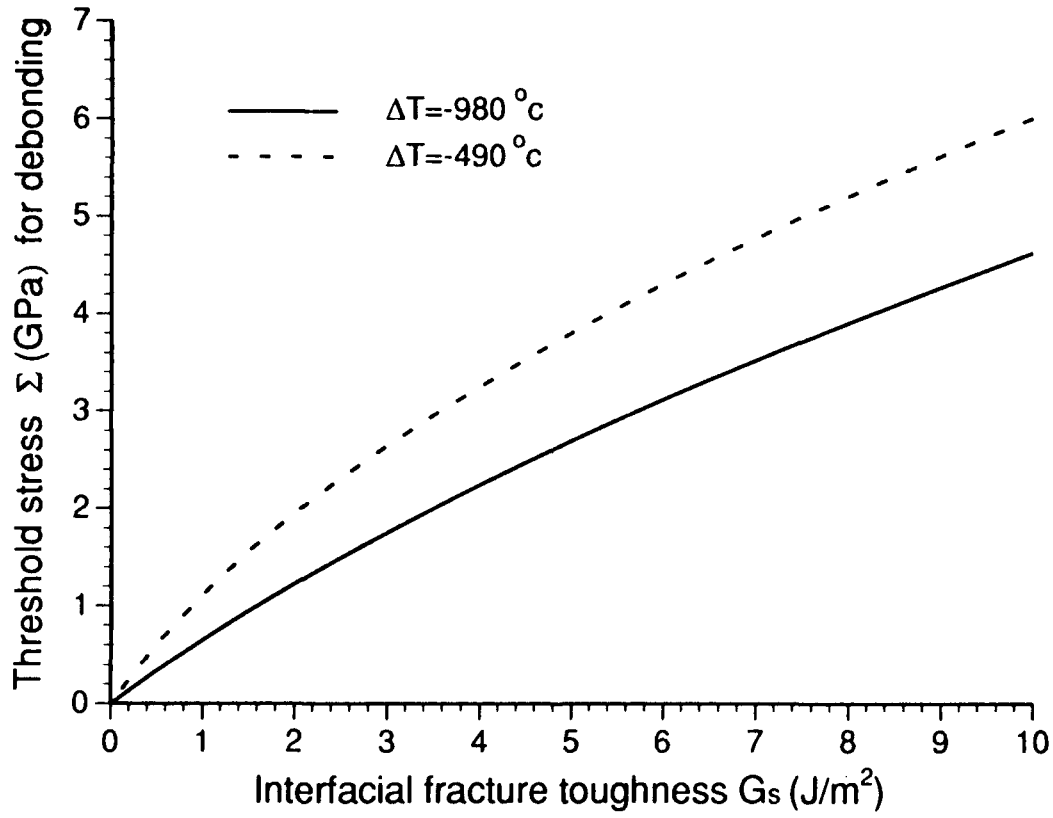
Threshold stress Σ (GPa) for debonding
Interfacial fracture toughness Gs (J/m²)
ΔT=-980 °c
ΔT=-490 °c
0
1
2
3
4
5
6
7
8
9
10

Fig.3

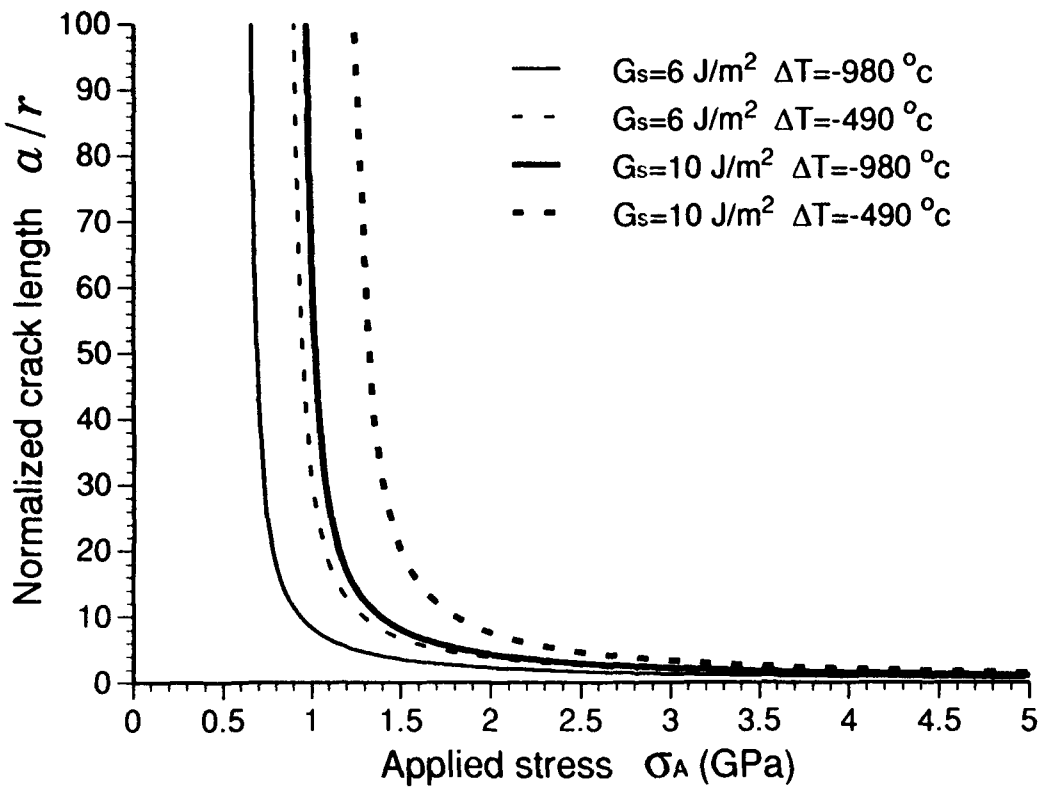
Normalized crack length a/r
100
90
80
70
60
50
40
30
20
10
0
0
0.5
1
1.5
2
2.5
3
3.5
4
4.5
5
Applied stress σ_A (GPa)
Gs=6 J/m² ΔT=-980 °c
Gs=6 J/m² ΔT=-490 °c
Gs=10 J/m² ΔT=-980 °c
Gs=10 J/m² ΔT=-490 °c

Fig.4

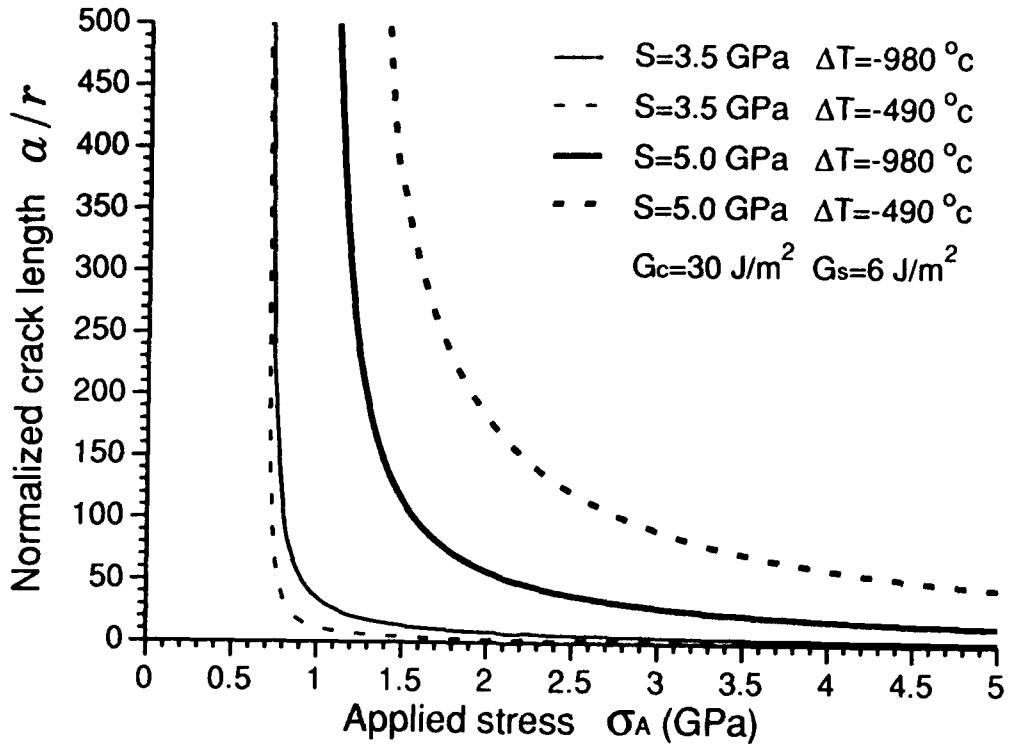
Normalized crack length a/r
500
450
400
350
300
250
200
150
100
50
0
0
0.5
1
1.5
2
2.5
3
3.5
4
4.5
5
Applied stress σ_A (GPa)
S=3.5 GPa ΔT=-980 °c
S=3.5 GPa ΔT=-490 °c
S=5.0 GPa ΔT=-980 °c
S=5.0 GPa ΔT=-490 °c
Gc=30 J/m2 Gs=6 J/m2

Fig.5

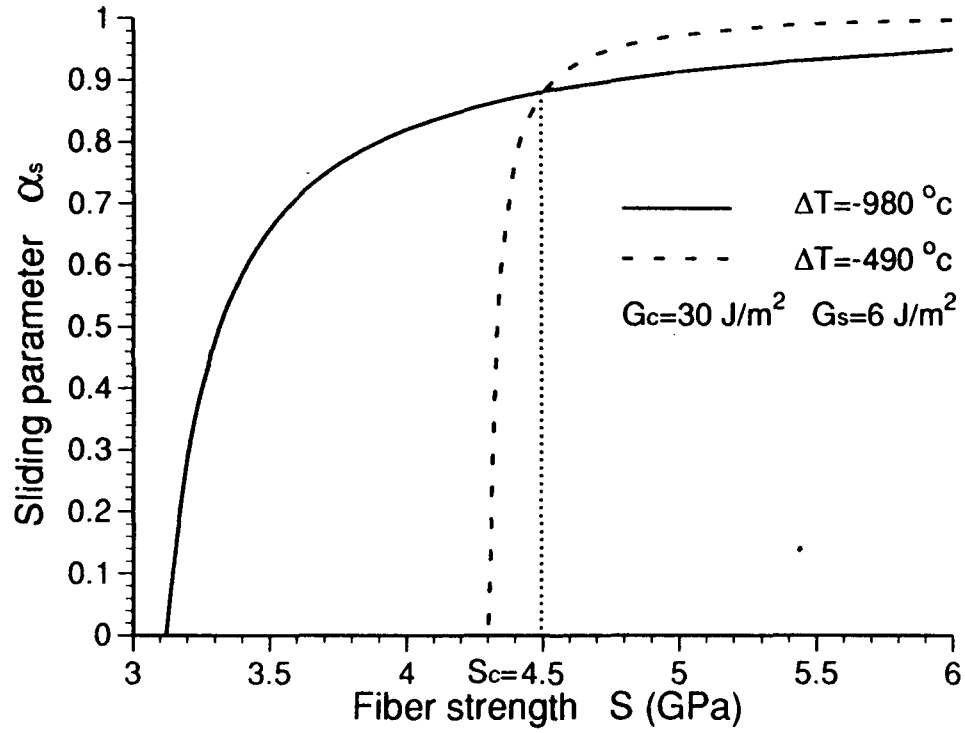
Sliding parameter α_s
1
0.9
0.8
0.7
0.6
0.5
0.4
0.3
0.2
0.1
0
3
3.5
4
Sc=4.5
5
5.5
6
Fiber strength S (GPa)
ΔT=-980 °c
ΔT=-490 °c
Gc=30 J/m² Gs=6 J/m²

Fig.6

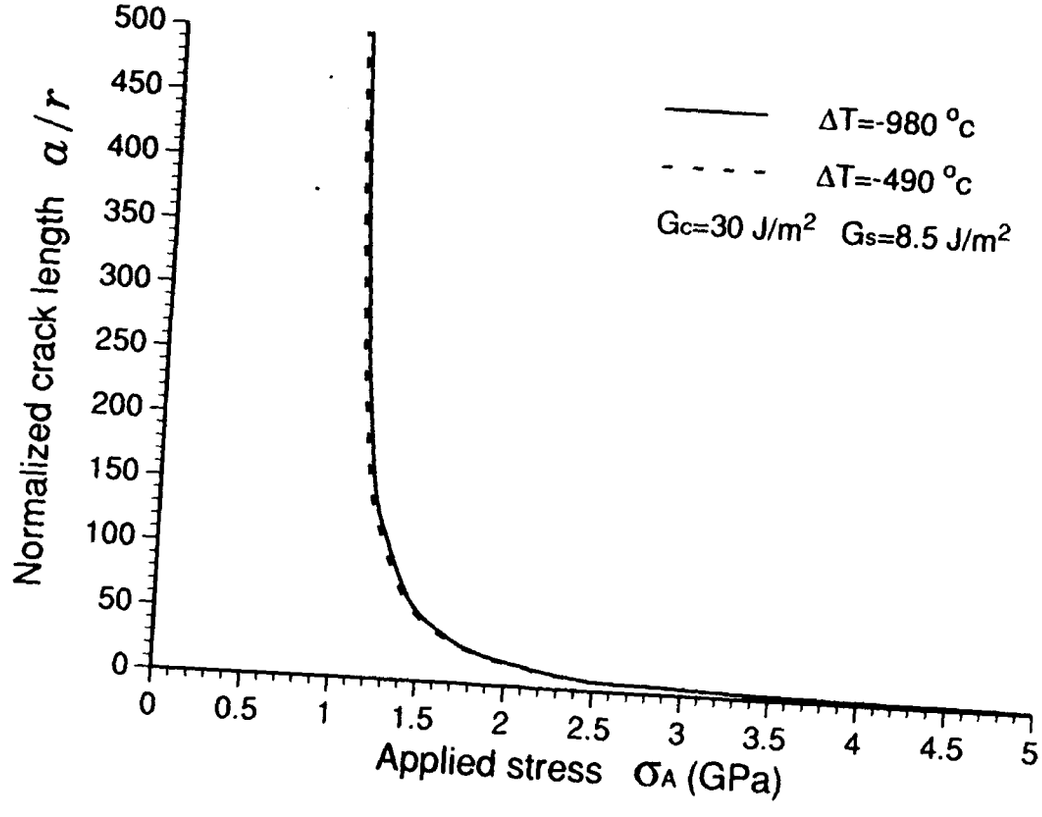
Normalized crack length a / r
500
450
400
350
300
250
200
150
100
50
0
0
0.5
1
1.5
2
2.5
3
3.5
4
4.5
5
Applied stress σA (GPa)
ΔT=-980 °c
ΔT=-490 °c
Gc=30 J/m2 Gs=8.5 J/m2

Fig.7

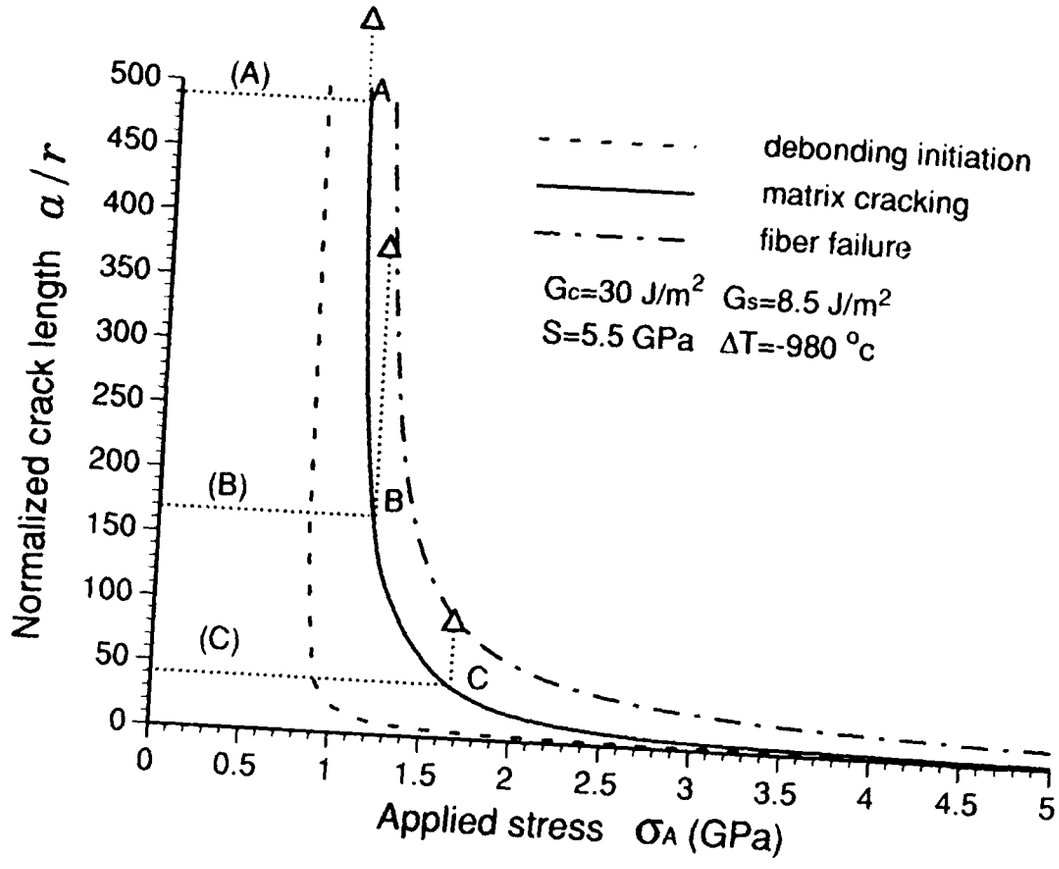
Normalized crack length a/r
500
450
400
350
300
250
200
150
100
50
0
(A)
(B)
(C)
A
B
C
debonding initiation
matrix cracking
fiber failure
G_c=30 J/m^2 G_s=8.5 J/m^2
S=5.5 GPa ΔT=-980 °c
0
0.5
1
1.5
2
2.5
3
3.5
4
4.5
5
Applied stress σ_A (GPa)

Fig.8

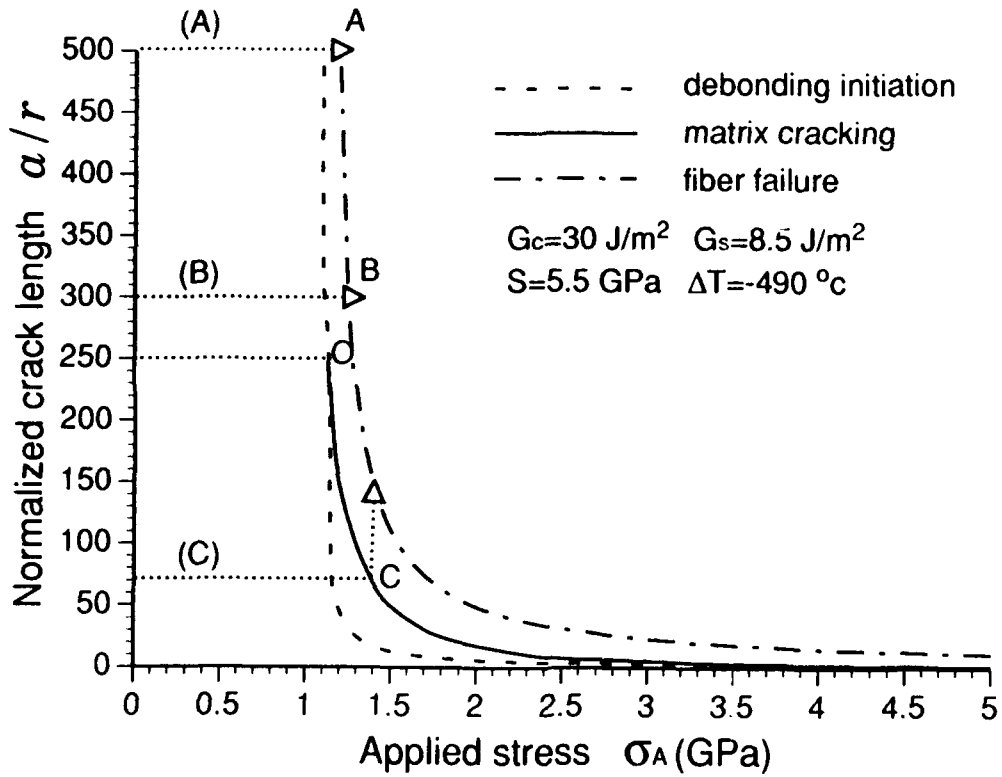
(A)
A
(B)
B
(C)
C
D
Δ
debonding initiation
matrix cracking
fiber failure
Gc=30 J/m2 Gs=8.5 J/m2
S=5.5 GPa ΔT=-490 °c
Normalized crack length a / r
Applied stress σA (GPa)
0
50
100
150
200
250
300
350
400
450
500
0
0.5
1
1.5
2
2.5
3
3.5
4
4.5
5

Fig.9

For: *Materials Science and Engineering, Part A* 2/15/92

Comparison of two loading configurations in fiber pullout tests

H. CAI,† Y. MAKITA†† AND K.T. FABER

Department of Materials Science and Engineering

Northwestern University

Evanston, IL 60208 (U.S.A.)

Abstract

In single fiber pullout experiments typical configurations of loading include support of the matrix on the side of the protruding fiber and support of the matrix from the opposite end. Single fiber pullout experiments have been conducted using these two configurations, and the experimental results are compared. The comparison shows that the difference in the measured fiber pullout frictional stresses between the two loading configurations is minimal for small embedded lengths. However, the difference increases with the fiber embedded length. Theoretical analysis predicts the same trends with loading configuration change.

1. Introduction

Fiber-reinforced composites offer the potential to meet the demands of materials that are light, strong and reliable. The mechanical properties of these materials are sensitive to the fiber/matrix interfacial properties, in addition to the

---

† Present address: Ceramics Division, National Institute of Standards and Technology, Gaithersburg, MD 20899. On leave from Department of Materials Science and Engineering, Lehigh University, Bethlehem, PA.

†† Present address: Futaba Corporation, Electronic Components Division, Chiba 297, Japan.

intrinsic properties of the fibers and the matrices [1,2]. Recognizing the importance of interfacial properties has resulted in numerous studies to characterize the debonding and frictional sliding phenomena [3-8]. Fiber pullout and push-down (indentation) are the two most frequently used experimental techniques for measuring the interfacial debonding stress and frictional stress in fiber composites. Detailed analyses of these two different methods of loading of the fiber show substantial differences between fiber pullout and push-down due to the Poisson effect in the fiber [9]. In fiber pullout testing, different methods of matrix loading have also been used, including support of the matrix opposite the side of the protruding fiber and support of the matrix on the side of the protruding fiber, as illustrated in Fig. 1. Such a difference in loading methods for fiber pullout may also result in different measured interfacial properties due to different boundary conditions. The objective of this work is to compare the frictional pullout stresses obtained using these two methods of matrix loading during pullout.

2. Experimental procedure

The specimen geometry and loading fixtures are shown in Fig. 2 for loading configurations A and B, respectively. In both fixtures, a self-aligning mechanism was used to ensure good alignment for fiber pullout. In the specimen geometry for loading configuration A, the fiber was pre-notched so that the fiber failed at the notch upon loading and was subsequently pulled out.

The single fiber composite consisted of steel piano wire in an acrylic[§] matrix. The acrylic fails in a brittle manner at room temperature. The steel wire has a diameter of 0.23 mm, and has a yield strength of 3 GPa, and fails with a very small degree of yielding. Debonding and pullout of the steel wire took place at stresses

---

[§] Acrylite FF, CYRO Industries, Mt. Arlington, NJ.

well below the yield point. The steel wire was cleaned with acetone and methyl alcohol, and the acrylic was cleaned with methyl alcohol before being used for specimen preparation. The pullout specimens were fabricated by sandwiching the steel wire between two acrylic plates and hot pressing at 155±2°C. The pullout specimens then were machined from the hot pressed samples.

Pullout experiments were performed using an Instron universal testing machine‡ at a constant crosshead speed of 0.5 mm/min. The load and crosshead displacement were recorded using a computer data acquisition system. Stick-slip behavior was observed as the fiber was pulled out the matrix. The pullout load was taken from the peak load of each stick-slip section. The corresponding fiber embedded length was determined from the load-displacement curve after subtracting the displacement due to the load train compliance.

4. Results and discussion

The results of frictional pullout stress, σ_p, vs. fiber embedded length, l_e, for the two loading configurations are shown in Fig. 3 for fiber embedded lengths ranging from 2 to 12 mm. Results are shown for five pullout tests for each configuration. The dashed line and the solid line are the curve fits to the data using function $\sigma_p = c_o\,[1 - \exp(c_1\, l_e)]$ for results of loading configurations A and B where c_o and c_1 are constants. While there is a scatter in the data, a comparison of the curves shows a difference in pullout stresses in the upper range of the fiber embedded lengths examined, with the pullout stress for loading configuration B lower than that for loading configuration A. The difference in the pullout stresses between the two loading configurations increases with the fiber embedded length. It is expected that the difference would further increase with the fiber embedded length.

‡ Instron Model 1125, Instron, Corp., Canton, MA.

The difference in the pullout stress between the two loading configurations can be understood physically as follows. In loading configuration B, the matrix is in axial compression. Due to the Poisson effect, axial compression increases the diameter of the matrix hole that holds the fiber. Therefore, a lower pullout stress is expected. In loading configuration A, axial tension in the matrix decreases the diameter of the matrix hole that holds the fiber, and thus, a greater pullout stress is anticipated. The Poisson effect in the matrix as observed is considerably smaller than that in the fiber because the axial stress in the matrix is significantly lower than that in the fiber as the matrix size is many times that of the fiber in typical single fiber pullout tests.

The experimental results of the present study are compared with the the theoretical analysis by Hsueh [10] (see Appendix A for more details of the analysis). It is assumed that both the matrix and the fiber display linear elastic behavior, and that the interfacial pullout may be described by Coulomb friction. In order to compare experiment with theory , two parameters which describe the Coulomb friction at the interface are needed: the normal residual stress (σ_c) and a coefficient of friction (μ). This two parameters were obtained experimentally using a technique described by Takaku and Arridge [11]. In this experiment, the dependence of the pullout stress (σ_p) on the initial tensile stress on the fiber (σ_f^0) was determined and analyzed using the following equation to obtained residual normal compressive stress and the coefficient of friction:

$$\sigma_p = \left(\frac{\sigma_0}{k} - \sigma_f^0\right)\left[1 - \exp\left(-\frac{2\,k\,\mu\,l_e}{a}\right)\right] \tag{1}$$

where l_e is the fiber embedded length, a is the radius of the fiber, $k = (E_m \nu_f)/[E_f(1+\nu_m)]$, E_m, E_f, ν_m, and ν_f are the Young's moduli and the Poisson's ratios of the matrix and fiber. For the steel wire-acrylic system, the residual normal compressive stress was determined to be 8 MPa with a coefficient of friction $\mu = 0.5$.

With the measured normal compressive stress and the coefficient of friction, the predicted pullout stresses for the two loading configurations are computed as a function of the embedded length, and are compared with experimental results in Fig. 4(a). Although the experimental and theoretical results do not agree well, the effect of the loading configurations demonstrates the same trend, that is, the pullout stress determined via loading configuration A is greater than that from loading configuration B for a given embedded length.

An alternative way to compare the experimental and theoretical results is to fit the experimental data for one loading configuration to obtain the normal compressive stress and the coefficient of friction and to compute the expected behavior for the second loading configuration. These results may then be compared with the experimental results for the latter loading configuration. Such a comparison is shown in Fig. 4(b), in which the experimental results for loading configuration A is fit into eqn. (1) in Ref. 10 with the coefficients A_1 and A_2 in Appendix A, giving a normal compressive stress of 2.2 MPa and a friction coefficient of 2.3. The theoretical prediction for loading configuration B is computed using eqn. (8) in Ref. 10 and is plotted along with the experimental results for the same loading configuration. The comparison now shows good qualitative agreement between the experiment and the theory. A difficulty with this approach is that the coefficient of friction obtained is unreasonably high. Furthermore, the obtained values of the coefficient of friction and normal compressive stress are inconsistent with those obtained using Takaku and Arridge technique.

In order to gain a better understanding of the problem, the fiber surface and the matrix surface at the interface before and after fiber sliding were examined using scanning electron microscopy [12]. The observation shows that the matrix surface at the interface changes significantly after fiber sliding. Loose debris was observed on the interface matrix surface after sliding. At the same time,

the matrix surface was roughened. Therefore, the coefficient of friction at the interface changes with sliding and with sliding distance of fiber pullout. The normal compressive stress might have changed also due to the matrix wearing. These changes in the coefficient of friction and normal compressive stress with sliding distance could explain the poor agreement between the experiment and theory, the latter of which assumes a constant coefficient of friction and normal compressive stress. This observation has a strong implication for extracting the interfacial properties from single fiber pullout tests: misleading values can result from fitting the data to models which assume constant coefficient of friction and normal compressive stress if in reality. these parameters change with fiber pullout.

5. Summary

The fiber frictional pullout stresses of two matrix loading configurations have been compared experimentally. The difference of results between the two matrix loading configuration is minimal for short fiber embedded lengths. The difference increases with fiber embedded length, indicating the need to consider the matrix loading condition for fiber pullout with long fiber embedded lengths. A comparison between theory and experiment was complicated by changing coefficient of friction and probably changing normal compressive stress with fiber pullout. However, the comparison shows a qualitative agreement, that is, the pullout stress for loading the matrix face opposite the protruding fiber is greater than that obtained from supporting the matrix on the side of the protruding fiber.

Acknowledgements

Support of this work has been provided by the Air Force Office of Scientific Research under Funding No. G-AFOSR-89-0269. Support for Y.M. has been provided

in part by Futaba Corporation, Chiba, Japan. The authors would like to thank Drs. C.H. Hsueh and J.O. Brittain for useful discussions.

References

1 D. B. Marshall and A. G. Evans, Failure Mechanisms in Ceramic-Fiber/Ceramic-Matrix Composites, *J. Am. Ceram. Soc.*, *68* (1985) 225-231.

2 P. F. Becher, C.-H. Hsueh, P. Angelini and T. N. Tiegs, Toughening Behavior in Whisker-Reinforced Ceramic Matrix Composites, *J. Am. Ceram. Soc.*, *71* (1988) 1050-1061.

3 D. B. Marshall, An Indentation Method for Measuring Matrix-Fiber Frictional Stresses in Ceramic Composites, *J. Am. Ceram. Soc.*, *69* (1984) C259-C260.

4 D. H. Grande, J. F. Mandell and K. C. C. Hong, Fibre-Matrix Bond Strength Studies of Glass, Ceramic, and Metal Matrix Composites, *J. Mat. Sci.*, *23* (1988) 311-328.

5 T. P. Weihs, C. M. Dick and W. D. Nix, The Frictional Resistance to Sliding of a SiC Fiber in a Brittle Matrix, pp.247-252 in *High Temperature/High Performance Composites*, Vol.120, F. D. Lemkey, S. G. Fishman, A. G. Evans and J. R. Strife, eds., Materials Research Society, Pittsburgh, PA, 1988.

6 J. D. Bright, D. K. Shetty, C. W. Griffin and S. Y. Limaye, Interfacial Bonding and Friction in Silicon Carbide (Filament)-Reinforced Ceramic- and Glass-Matrix Composites, *J. Am. Ceram. Soc.*, *72* (1989) 1891-1898.

7 R. W. Goettler and K. T. Faber, Interfacial Shear Stresses in Fiber-Reinforced Glasses, *Comp. Sci. Tech.*, *37* (1989) 129-147.

8 E. P. Butler, E. R. Fuller, Jr. and H. M. Chan, Interface Properties for Ceramic Composites from a Single-Fiber Pullout Test, pp.17-24 in *Tailored Interfaces in Composite Materials*, C. G. Pantano and E. J. H. Chen, eds., MRS, Pittsburgh, PA, 1990.

9 C.-H. Hsueh, Fibre Pullout Against Push-down for Fibre-reinforced Composites with Frictional Interfaces, *J. Mater. Sci.*, *25* (1990) 811-817.

10 C.-H. Hsueh, Theoretical Comparison of Two Loading Fixtures in Fiber Pull-Out Tests, *Mater. Sci. Eng.*, *A130* (1990) L11-L15.

11 A. Takaku and R. G. C. Arridge, The Effect of Interfacial Radial and Shear Stress on Fibre Pull-out in Composite Materials, *J. Phys. D: Appl. Phys.*, *6* (1973) 2038-2047.

12 Y. Makita, *Determination of the Interfacial Properties in Fiber-Reinforced Composites via Model Single Fiber Pullout Tests*, M.S. Thesis, Northwestern University, Evanston, Illinois, 1991.

13 C.-H. Hsueh, Personal Communication, 1991.

Appendix A. Theoretical analysis of fiber frictional pullout

Hsueh [10] analyzed the two loading configurations (Fig. 1) for pullout tests using an idealized model for a single fiber pullout consisting of a fiber located in the center of a co-axial cylindrical matrix. The pullout stresses for the two loading configurations are given by Hsueh in Ref. 10. Due to the length of the equations, they are not reproduced here.

In Hsueh's work [10], an approximation of the shear stress distribution in the matrix results in a finite value of shear stress at the outer surface of the matrix. Hsueh [13] improved the original analysis by introducing an alternative shear stress distribution in the matrix which satisfies the boundary conditions of zero tractions on the cylindrical surface of the matrix. The results of the pullout stress are the same as those given in the original work [10], with the exception of changes in coefficient A_1 and A_2, which are given as [13]:

$$A_1 = \frac{a\,(1 - b^2/a^2)\,D}{2\,\mu\,\nu_m\,(1 + \nu_m)\,\dfrac{b^2}{b^2 - a^2}\left[\,b^2 \ln(b/a) - \dfrac{(b^2 - a^2)\,(3\,b^2 - a^2)}{4b^2}\right]} \tag{A1}$$

$$A_2 = \frac{(1 - b^2/a^2)\,(E_m\,\nu_f\,/\,E_f\,\nu_m) - 1}{2\,\mu\,\nu_m\,(1 + \nu_m)\,\dfrac{b^2}{b^2 - a^2}\left[\,b^2 \ln(b/a) - \dfrac{(b^2 - a^2)\,(3\,b^2 - a^2)}{4b^2}\right]} \tag{A2}$$

The effects of this change on the pullout stress is very small. However, the new solutions are used because they satisfy the boundary conditions of free tractions on the outer cylindrical surface of the matrix.

Figure Captions

Fig. 1. Schematic of the two matrix loading configurations used in fiber pullout tests: (a) support of the matrix opposite the side of the protruding fiber and (b) support of the matrix on the side of the protruding fiber.

Fig. 2. Schematic of specimen geometry and loading fixture for: (a) loading configuration A and (b) loading configuration B.

Fig. 3. Experimental results comparing frictional pullout stress for the two different loading configurations examined.

Fig. 4. (a) A comparison of experimental results and theoretical predictions based on an independent measurement of the normal compressive stress and coefficient of friction; (b) A comparison of experimental results and theoretical prediction for configuration B. The normal compressive stress and coefficient of friction were obtained by curve fitting the experimental results to Hsueh's theory [10,13] for configuration A.

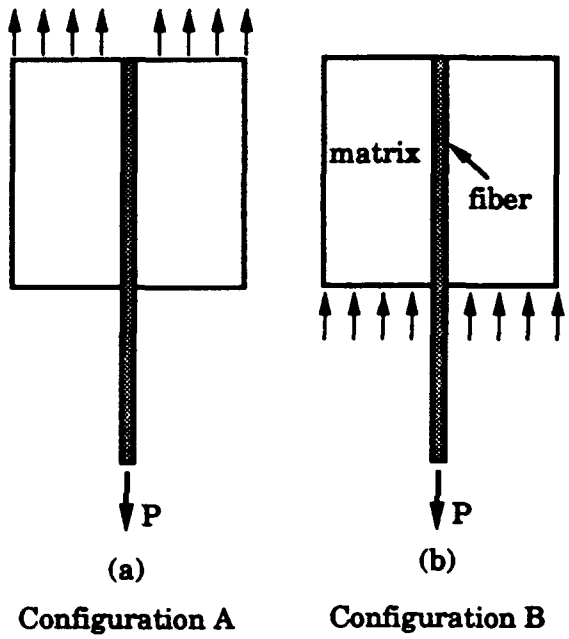

Fig. 1

MDII047.2

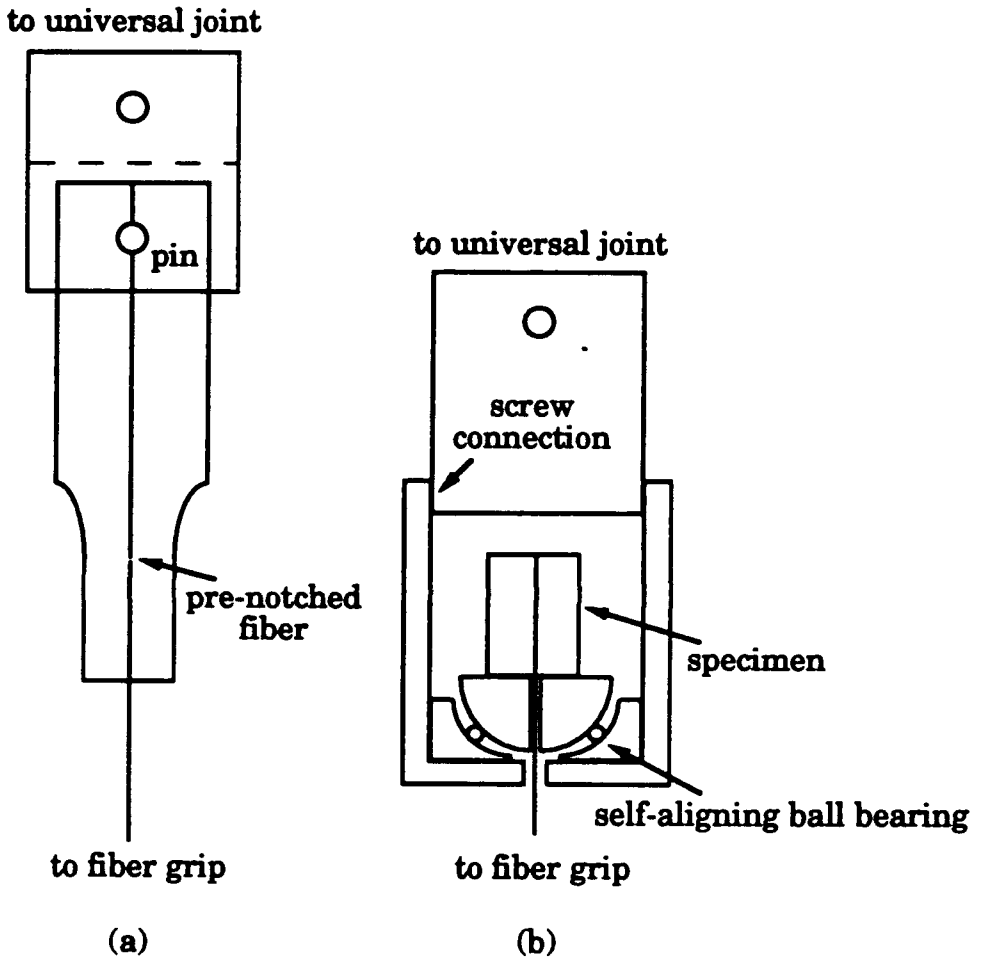

Fig. 2

MDII053.4

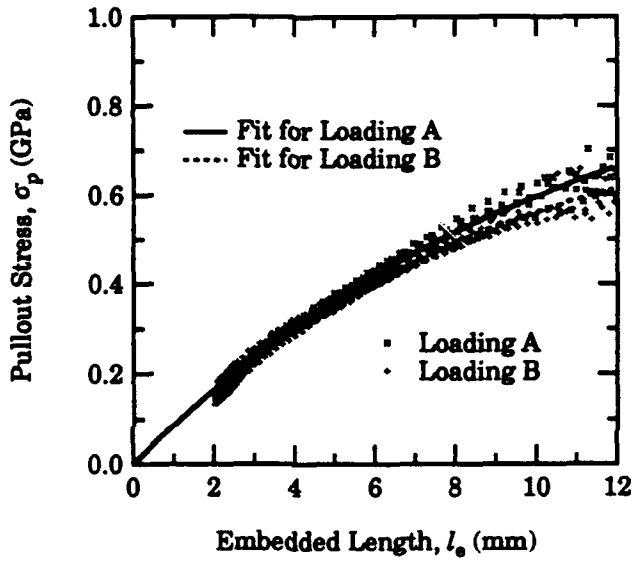

Fig. 3

IG186(L0:G0)

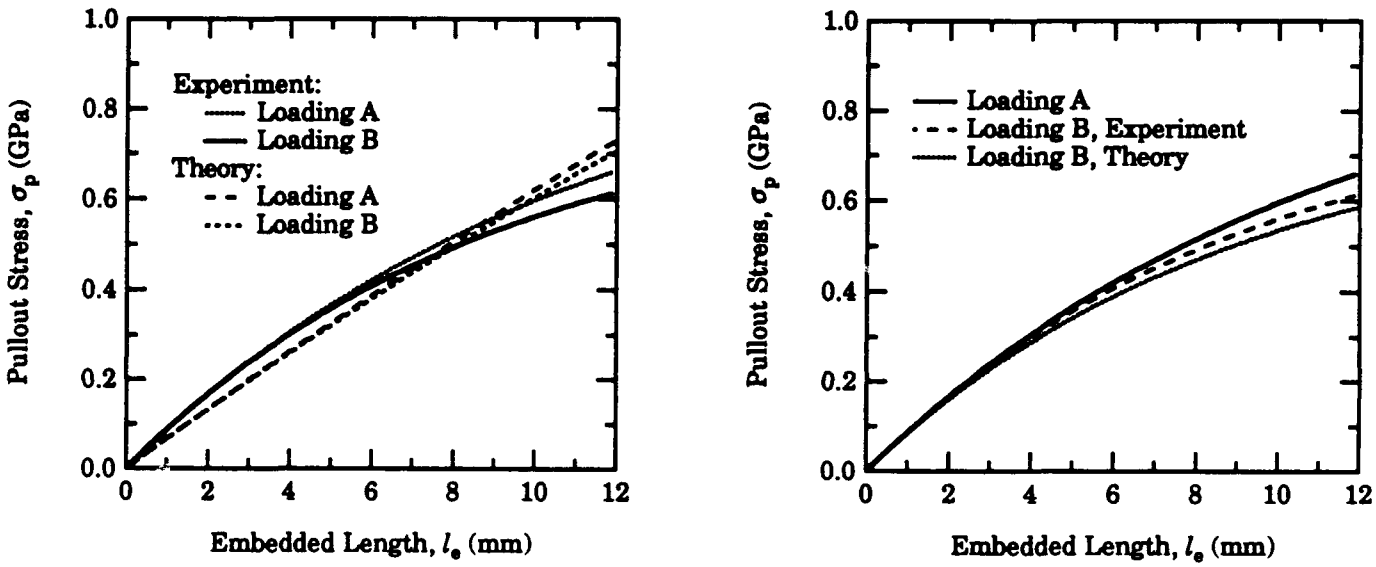

(a) (b)

Fig. 4

IG186(L1:G1,G3)

APPENDIX 5

Inverse Problems in Linear Elasticity

by

Tatsuhito Koya
and
Toshio Mura

Department of Civil Engineering
Northwestern University
Evanston, Illinois 60201

Abstract

Some inverse problems in linear isotropic elasticity are considered. The problems of interest in this paper are Cauchy problems (see [1]) that cannot be solved directly; therefore, special techniques involving transformations are required. The regularization method employed by Gao and Mura [2] and Yeih, et. al. [3, 4] are examined in order to improve efficiency and computer implementation. At the same time, an alternative method based on the classical least-squares method is proposed.

1. Introduction

Consider the following problem. A thin rectangular plate is maintained at zero temperature along the three edges $x = 0$, $x = a$, and $y = 0$. The fourth edge $y = b$ is

subjected to a temperature distribution $f(x)$ (see Fig. 1). We would like to calculate the temperature distribution when steady-state is reached.

This is a typical Laplace problem. The temperature distribution is governed by the Laplace equation,

$$\nabla^2\varphi = \frac{\partial^2\varphi}{\partial x^2} + \frac{\partial^2\varphi}{\partial y^2} = 0, \tag{1}$$

and the solution is

$$\varphi(x,y) = \sum_{n=1}^{\infty} c_n \sin\frac{n\pi x}{a}\frac{\sinh(n\pi y/a)}{\sinh(n\pi b/a)}, \tag{2}$$

where

$$c_n = \frac{2}{a}\int_0^a f(x)\sin\frac{n\pi x}{a}dx, \tag{3}$$

assuming this series is convergent.

Now, consider the following problem. Instead of prescribing temperatures along all edges, we prescribe a temperature $f(x)$ **and** a flux $\partial\varphi/\partial y|_{y=b} = g(x)$ along $y = b$, and keep the remaining edges free (see [5]) as shown in Fig. 2. We would like to calculate the temperature distribution.

Unlike the first boundary-value problem, the second one is categorized as a Cauchy (initial-value) problem (see [1]), and it is a type of inverse problem. The given data (boundary conditions) in this problem are called the Cauchy data. Tikhonov, one of the first pioneers of the inverse problem, stated that to solve an inverse problem means to discover the cause of a known result. Therefore, he continued that all problems of the interpretation of observed data are actually inverse [6].

Although his description seems to indicate that both first and second problems are inverse; however, in almost all cases, we distinguish the first one from the second one and call the first one a forward (regular) problem and the second one an inverse problem. The inverse problem usually involves drawing of a conclusion (cause) from incomplete information. Only incomplete information may be obtained because the points of interest are visually hidden, or the sensors cannot simply reach those points.

Two of the first classical works on the inverse problem may be attributed to Legendre [7] and Gauss [8] when they independently calculated the trajectory of Halley's comet from discrete observed data by means of the least-squares method. Today, the inverse problem is receiving more attention, particularly in the field of design optimization (e.g., Sobieczky [9] and Staniz [10]).

2. Inverse Problems in Linear Elasticity

Let us see how the inverse problem fits in linear elasticity. Historically, inverse problems in elasticity date back as far as 1907 to Alamansi [11]. A more recent work was done by Gao and Mura [2] and Yeih, et. al. [3, 4].

Consider the following problem. An thin circular disc of a radius $r = 1.0\text{m}$ and elasticity constants $E = 500\text{MPa}$ and $\nu = 0.3$ is subjected to a radial load $p = 2.0\text{MPa}$ as shown in Fig. 3. If we eliminate rigid body motion, the x and y displacements along the edge are

$$\begin{cases} u_x = \dfrac{0.7}{250}\cos(\theta), \\ u_y = \dfrac{0.7}{250}\sin(\theta). \end{cases} \tag{4}$$

Now, consider the following problem. The same disc is subjected to the same radial load **and** displacements given by (4) along the edge ranging $0 \le \theta \le \pi$ as shown in Fig. 4. Can we find the tractions and displacements along the remaining edge $\pi < \theta < 2\pi$ assuming that the disc is in static equilibrium? Obviously, the solutions are

$$\begin{cases} p_x = 2\cos(\theta), \\ p_y = 2\sin(\theta), \\ u_x = \dfrac{0.7}{250}\cos(\theta), \\ u_y = \dfrac{0.7}{250}\sin(\theta). \end{cases} \tag{5}$$

This inverse problem is simple because of the problem's simple geometry and loading condition; however, how can we treat inverse problems that have complicated shapes and loading conditions?

3. Numerical Approach

When a body has a complicated geometry and is subjected to complex displacement and loading conditions, there is very little hope to solve the problem analytically. In general, such a problem is solved numerically by means of the finite element method (FEM) or the boundary element method (BEM):

$$\begin{cases} \displaystyle\int_\Omega \mathbf{B}^T\mathbf{D}\mathbf{B}\mathbf{u}\,d\Omega = \int_\Omega \mathbf{N}\mathbf{f}\,d\Omega, & \text{FEM} \\ \displaystyle\frac{1}{2}\mathbf{N}\mathbf{u} + \int_\Gamma \mathbf{T}\mathbf{N}\mathbf{u}\,d\Gamma = \int_\Gamma \mathbf{U}\mathbf{N}\mathbf{t}\,d\Gamma, & \text{BEM} \end{cases} \tag{6}$$

normal derivative, Ω is the body, and Γ is its boundary which is assumed to be smooth in this case (the presence of ½ coefficient). Two major differences between these methods is that FEM solves a domain integral equation whereas BEM solves a boundary integral equation, and FEM solves for displacements only whereas BEM solves for both displacements and tractions. Both methods employ discretization of the domain of integration; consequently, FEM requires to discretize the entire body whereas BEM requires to discretize its boundary only when body forces are neglected.

At the first glance, because FEM requires prescribing of the conditions inside the body, this method is not suitable for our purpose. On the other hand, because BEM requires prescribing of the conditions along the boundary only, we will employ this method to solve Cauchy problems.

4. The General Numerical Procedure to Solve Integral Equations

Before proceeding to solve Cauchy problems, we first look into the procedure to solve an integral equation numerically. Consider the following integral equation,

$$\int_0^1 x' x u(x) dx - \frac{1}{2} u(x') = \cos(\pi x'), \quad 0 \le x' \le 1. \tag{7}$$

The exact solution is

$$\frac{24x}{\pi^2} - 2\cos(\pi x), \tag{8}$$

and we would like to approximate this solution numerically.

We use the 3-pt Gauss-Legendre quadrature to evaluate the integral in (7). The formula is

We use the 3-pt Gauss-Legendre quadrature to evaluate the integral in (7). The formula is

$$\int_a^b f(x)dx \cong J\sum_{i=1}^{3} f(c+J\xi_i)w_i, \tag{9}$$

where

$$\begin{aligned} J &= (b-a)/2, \\ c &= (b+a)/2, \\ \xi &= \{-\sqrt{3/5},\ \ 0,\ \ \sqrt{3/5}\}, \\ w &= \{5/9\ \ \ 8/9\ \ \ 5/9\}. \end{aligned} \tag{10}$$

We do not know the values of u at the points of evaluation (sample points). Therefore, we have three unknowns and require three equations to solve for them. We choose the same points for x' in order to create three equations. In essence, we have transformed an integral equation into a system of simultaneous equations,

$$\begin{bmatrix} 0.0278 & -0.4965 & 0.0250 \\ 0.1232 & 0.1565 & -0.3889 \\ -0.2813 & 1.1517 & 0.1972 \end{bmatrix} \begin{Bmatrix} u_1 \\ u_2 \\ u_3 \end{Bmatrix} = \begin{Bmatrix} 0.9380 \\ 0 \\ -0.9380 \end{Bmatrix}. \tag{11}$$

The solution is

$$u = \{-1.6030\ \ \ 1.2101,\ \ \ 4.0248\} \tag{12}$$

which is in good agreement with the exact solution,

$$u = \{-1.6019,\ \ 1.2159,\ \ 4.0336\}. \tag{13}$$

As the number of points increases, the accuracy of solution increases as shown in Fig. 5. The rate of convergence depends on the numerical integration

scheme. Fig. 5 uses the trapezoidal rule, which is not a powerful scheme, in order to illustrate this point. This method of solving integral equations is called the Nystrom method (see [12]).

5. The Compatibility Condition of the Cauchy Data

In Section 4, we saw how an ordinary integral equation can be solved by the Nystrom method. Now we look into the Cauchy problem and pay special attention to Laplace-type problems as shown in Figs. 1 and 2. But, first, we list here 3 types of boundary-value problem (see [1, 13]):

i. Dirichlet Problem: *Only φ is prescribed along the boundary. There exists a unique solution.*

ii. Neumann Problem: *Only the normal derivative $\partial\varphi/\partial n$ is prescribed along the boundary. The solution may not exist, or even if it does, it is not unique by an arbitrary constant.*

iii. Mixed Problem: *Either φ or $\partial\varphi/\partial n$ are prescribed along the boundary. There exists a unique solution.*

Bearing in mind the above problem types, we recall Green's second identity (see [1]),

$$\varphi(x') = \int_{\Gamma} \left[\frac{\partial G(x,x')}{\partial n} \varphi(x) - G(x,x') \frac{\partial \varphi(x)}{\partial n} \right] d\Gamma(x) \tag{14}$$

where G is the Green's function for the Laplace equation. This identity states that when both φ and $\partial\varphi/\partial n$ are prescribed along the boundary, φ inside the

domain can be uniquely determined. However, this statement is in contradiction to the uniqueness of solution of the Dirichlet problem. If we already know φ everywhere along the boundary, cannot we determine φ uniquely without necessitating the knowledge of $\partial\varphi/\partial n$? For this reason, we cannot arbitrarily prescribe φ and $\partial\varphi/\partial n$ on the same boundary (Cauchy data) and solve the Cauchy problem directly. This difficulty raises the compatibility condition which must be imposed on φ and $\partial\varphi/\partial n$.

Let us assume that the boundary Γ, φ, and $\partial\varphi/\partial n$ are parametrically representable by the variable s, so that we can write $\Gamma(s), \varphi(s)$ and $\partial\varphi(s)/\partial n$. In two dimension, the normal derivative $\partial\varphi(s)/\partial n$ is written as

$$\frac{\partial\varphi}{\partial n} = \nabla\varphi \cdot \mathbf{n} = \frac{\partial\varphi}{\partial x} n_x + \frac{\partial\varphi}{\partial y} n_y, \tag{15}$$

where

$$\begin{aligned} n_x &= \frac{\partial y}{\partial s}, \\ n_y &= -\frac{\partial x}{\partial s}. \end{aligned} \tag{16}$$

Also, we can write

$$\frac{\partial\varphi}{\partial s} = \frac{\partial\varphi}{\partial x}\frac{\partial x}{\partial s} + \frac{\partial\varphi}{\partial y}\frac{\partial y}{\partial s}. \tag{17}$$

Therefore, the only unknowns are $\partial\varphi/\partial x$ and $\partial\varphi/\partial y$; consequently we can form a system of simultaneous equations,

$$\begin{bmatrix} \dfrac{\partial x}{\partial s} & \dfrac{\partial y}{\partial s} \\ \dfrac{\partial y}{\partial s} & -\dfrac{\partial x}{\partial s} \end{bmatrix} \begin{Bmatrix} \dfrac{\partial\varphi}{\partial x} \\ \dfrac{\partial\varphi}{\partial y} \end{Bmatrix} = \begin{Bmatrix} \dfrac{\partial\varphi}{\partial s} \\ \dfrac{\partial\varphi}{\partial n} \end{Bmatrix}. \tag{18}$$

The above system is solvable as long as the coefficient matrix is nonsingular.

We then proceed to compute the second derivatives,

$$\begin{aligned} \frac{\partial^2 \varphi}{\partial x^2} &= \frac{\partial}{\partial x}\frac{\partial \varphi}{\partial x}, \\ \frac{\partial^2 \varphi}{\partial y^2} &= \frac{\partial}{\partial y}\frac{\partial \varphi}{\partial y}. \end{aligned} \tag{19}$$

We take advantage of the chain rule again to form,

$$\begin{bmatrix} \frac{\partial x}{\partial s} & \frac{\partial y}{\partial s} \\ \frac{\partial y}{\partial s} & -\frac{\partial x}{\partial s} \end{bmatrix} \begin{Bmatrix} \frac{\partial}{\partial x} \\ \frac{\partial}{\partial y} \end{Bmatrix} = \begin{Bmatrix} \frac{\partial}{\partial s} \\ \frac{\partial}{\partial n} \end{Bmatrix} \tag{20}$$

whence

$$\begin{Bmatrix} \frac{\partial}{\partial x} \\ \frac{\partial}{\partial y} \end{Bmatrix} = \frac{1}{J} \begin{bmatrix} \frac{\partial x}{\partial s} & \frac{\partial y}{\partial s} \\ \frac{\partial y}{\partial s} & -\frac{\partial x}{\partial s} \end{bmatrix} \begin{Bmatrix} \frac{\partial}{\partial s} \\ \frac{\partial}{\partial n} \end{Bmatrix}, \tag{21}$$

where

$$J = \left(\frac{\partial x}{\partial s}\right)^2 + \left(\frac{\partial y}{\partial s}\right)^2. \tag{22}$$

The computed second derivatives must satisfy the Laplace equation,

$$\frac{\partial^2 \varphi}{\partial x^2} + \frac{\partial^2 \varphi}{\partial y^2} = 0. \tag{23}$$

The Cauchy data are then compatible.

6. Numerical Difficulties in Solving Cauchy Problems

Consider a domain Ω which is bounded by a boundary Γ. The Laplace equation holds inside this domain. Denote a part of the boundary as Γ_1 and the remaining part as Γ_2, so that $\Gamma = \Gamma_1 + \Gamma_2$. Suppose the Cauchy data (potential and flux) are prescribed along Γ_1. We would like to compute the potential and flux along Γ_2.

For the simplicity sake, we assume that the Cauchy data are compatible, and with the Cauchy data, we can carry out the integrations along Γ_1 in (14) and denote the sum as $b(x')$,

$$b(x') = \int_{\Gamma_1} \left[G(x,x') \frac{\partial \varphi(x)}{\partial n} - \frac{\partial G(x,x')}{\partial n} \varphi(x) \right] d\Gamma. \tag{24}$$

Consequently, Green's second identity is reduced to

$$\varphi(x') + \int_{\Gamma_2} \left[\frac{\partial G(x,x')}{\partial n} \varphi(x) - G(x,x') \frac{\partial \varphi(x)}{\partial n} \right] d\Gamma = b(x'), \quad x' \in \Omega. \tag{25}$$

We do not wish to keep x' inside Ω since we do not have any information as to the value of φ. When x' is placed on the boundary Γ and if the boundary is smooth, (25) can be rewritten as

$$\frac{1}{2} \varphi(x') + \int_{\Gamma_2} \left[\frac{\partial G(x,x')}{\partial n} \varphi(x) - G(x,x') \frac{\partial \varphi(x)}{\partial n} \right] d\Gamma = b(x'), \quad x' \in \Gamma. \tag{26}$$

We apply the Nystrom method here. Let us use the Nth order numerical integration scheme to rewrite (26) as

$$\frac{1}{2} \varphi(x_i') + \sum_{j=1}^{N} \left[\frac{\partial G(x_j, x_i')}{\partial n} \varphi(x_j) - G(x_j, x_i') \frac{\partial \varphi(x_j)}{\partial n} \right] w_j = b(x_i'), \quad x' \in \Gamma, \quad i = 1, \ldots N. \tag{27}$$

From (27), we see that we can construct one equation at each sample point. However, there are 2 unknown quantities, φ and $\partial\varphi/\partial n$ at each sample point, so that there are more unknown than the number of equations. In general, we cannot solve this system of equation directly. The dimensions of the coefficient matrix are N by $2N$, and even if all the equations are independent, there is an $2N - N = N$ different dimensional family of solutions. There is no known method to determine the correct solution directly.

There is a way to reduce the order of dimensional family of solutions, however. Since there is nothing to prevent us from placing x' in (27) on Γ_1, we can increase the number of equations without increasing the number of unknowns. In the present case, if we choose N points on Γ_1, we can have an $2N \times 2N$ system of equations which we may be able to solve directly. It should be pointed out here that although we seem to construct a well-balanced system of equations by this scheme, it is not always the case as we will see later.

7. The Regularization Method

When a system of simultaneous equations is ill-conditioned, that is, the coefficient matrix is nonsquare or singular, we cannot solve it by means of Gaussian elimination for example. In general, we cannot expect an extremely good solution from an ill-conditioned system; however, we can obtain a probable solution by imposing extra conditions as to the nature of the solution. Gao and Mura [2] introduced the regularization method by applying an integral transformation to the original integral equation (e.g., (26)). Although their transformation is theoretically valid, computer implementation of the resulting multiple integral equation is difficult and not numerically efficient. It is more

convenient if we apply a linear algebraic transformation to the numerical equation (e.g., (27)). Let us write (27) in the linear algebraic form,

$$\mathbf{A}\mathbf{x} = \mathbf{b} \tag{28}$$

where the vector $\mathbf{x}$ contains the unknown φ and $\partial\varphi/\partial n$. Because $\mathbf{A}$ is either nonsquare or singular, its inverse does not exist. The approach Gao and Mura [2] took was to minimize the L_2 norm of $\mathbf{x}$ subject to (28) or

$$\text{minimize} \|\mathbf{x}\|_2 \tag{29}$$

$$\text{subject to} \|\mathbf{A}\mathbf{x} - \mathbf{b}\|_2 < \varepsilon, \tag{30}$$

where

$$\|\mathbf{x}\|_2 = \sqrt{\mathbf{x}^T\mathbf{x}}. \tag{31}$$

The constant ε is user-defined. The Lagrangian function for this problem is

$$L(\mathbf{x};\alpha) = \alpha\mathbf{x}^T\mathbf{x} - (\mathbf{A}\mathbf{x} - \mathbf{b})^T(\mathbf{A}\mathbf{x} - \mathbf{b}). \tag{32}$$

The corresponding Euler equation (see [14]) is

$$\left(\mathbf{A}^T\mathbf{A} + \alpha\mathbf{I}\right)\mathbf{x} = \mathbf{A}^T\mathbf{b}, \tag{33}$$

so that the solution is

$$\mathbf{x} = \left(\mathbf{A}^T\mathbf{A} + \alpha\mathbf{I}\right)^{-1}\mathbf{A}^T\mathbf{b}. \tag{34}$$

The value of α has to be determined recursively until (30) is fulfilled.

The computer implementation of (34) is far easier than that of Gao and Mura's multiple integral equation. However, computing $\mathbf{A}^T\mathbf{A}$ is susceptible to numerical roundoff errors and not generally recommended. If $\mathbf{A}$ is a full rank

matrix, the QR decomposition (see [15]) may be helpful, but we would like to consider a more general case. We introduce here the singular-value decomposition (SVD) technique (see [15]). Basically, the SVD decomposes **A** into

$$\mathbf{A} = \mathbf{U}\boldsymbol{\Sigma}\mathbf{V}^T, \tag{35}$$

where the elements of the diagonal matrix $\boldsymbol{\Sigma}$ are called the singular values of **A**. The matrices **U** and **V** are unitary matrices, that is,

$$\begin{aligned} \mathbf{U}^T\mathbf{U} &= \mathbf{I}, \\ \mathbf{V}^T\mathbf{V} &= \mathbf{I}. \end{aligned} \tag{36}$$

After substituting (35) into (33), we obtain

$$\left(\boldsymbol{\Sigma} + \alpha\boldsymbol{\Sigma}^{-T}\right)\mathbf{V}^T\mathbf{x} = \mathbf{U}^T\mathbf{b}, \tag{37}$$

and the solution (34) becomes

$$\mathbf{x} = \mathbf{V}\left(\boldsymbol{\Sigma} + \alpha\boldsymbol{\Sigma}^{-T}\right)^{-1}\mathbf{U}^T\mathbf{b}. \tag{38}$$

The solution by (38) is easier to control because we are tampering with the singular values only which directly affect the condition number of **A**. Also, although two matrix inversion are involved in (38), because the matrix $\boldsymbol{\Sigma}$ is a diagonal matrix so that it is a matter of inverting the diagonal elements. The regularization method coupled with the SVD is recommended to deal with all kinds of Cauchy problem.

8. The Least-Squares Method

The least-squares method has been used for many inverse and optimization problems. Legendre [7] and Gauss [8] used this method to solve one of the first inverse problems. We employ this method here coupled with the SVD introduced in the previous section.

Given an equation $\mathbf{Ax} = \mathbf{b}$, the least-squares method is derived as follows. We would like to minimize (extremize)

$$\|\mathbf{Ax} - \mathbf{b}\|_2 \tag{39}$$

with respect to $\mathbf{x}$. This gives rise to

$$\frac{d}{d\mathbf{x}}\left(\mathbf{x}^T\mathbf{A}^T\mathbf{Ax} - 2\mathbf{x}^T\mathbf{A}^T\mathbf{b} + \mathbf{b}^T\mathbf{b}\right) = 0, \tag{40}$$

or

$$\mathbf{A}^T\mathbf{Ax} = \mathbf{A}^T\mathbf{b}. \tag{41}$$

This equation is known as the **normal equation.** Commonly, (41) is solved by means of the QR decomposition (see [15]) because of the suceptability of the $\mathbf{A}^T\mathbf{A}$ computation to roundoff error. The decomposed normal equation becomes

$$\mathbf{Rx} = \mathbf{Q}^T\mathbf{b}. \tag{42}$$

The above equation is merely a backsubstitution operation.

The use of the QR decomposition is valid as long as an $m \times n$ matrix $\mathbf{A}$ has a rank n, so that $\mathbf{A}^T\mathbf{A}$ is a full rank matrix. However, many inverse problems have a less than rank n matrix. Consequently, the QR decomposition cannot be used.

In these cases, we employ the singular value decomposition technique. The SVD decomposes A into

$$\mathbf{A} = \mathbf{V}\boldsymbol{\Sigma}\mathbf{U}^T, \tag{43}$$

where

$$\begin{aligned} \mathbf{V}^T\mathbf{V} &= \mathbf{I}, \\ \mathbf{U}^T\mathbf{U} &= \mathbf{I}. \end{aligned} \tag{44}$$

Then (41) is reduced to

$$\boldsymbol{\Sigma}\mathbf{V}^T\mathbf{x} = \mathbf{U}^T\mathbf{b}. \tag{45}$$

Consequently,

$$\mathbf{x} = \mathbf{V}\boldsymbol{\Sigma}^{-1}\mathbf{U}^T\mathbf{b}. \tag{46}$$

Notice the resemblance between (38) and (46). If we let α in (38) go to zero, the two equations are the same. Therefore, the regularization method and the least-squares method are very similar; however, they are not the same. While the regularization method attempts to balance the order of singular values, the least-squares method cuts off numerically negligible singular values. Therefore, the regularization method is a full expansion whereas the least-squares method is a tuncated expansion.

9. Linear Elasticity Problems

We now apply the least-squares method to some two dimensional isotropic linear elasticity problems. The basic equation we use here is known as Somigliana's boundary integral equation (see [16]),

$$\frac{1}{2}u_i(x') + \int_\Gamma T_{ij}(x,x')u_j(x)ds(x) - \int_\Gamma U_{ij}(x,x')t_j(x)ds(x), \tag{47}$$

where $U_{ij}(x,x') = \dfrac{-1}{8\pi(1-\nu)G}\left\{(3-4\nu)\ln(r)\delta_{ij} - r_{,i}r_{,j}\right\},$

$$T_{ij}(x,x') = \frac{-1}{4\pi(1-\nu)r}\left\{\left[(1-2\nu)\delta_{ij} + 2r_{,i}r_{,j}\right]\frac{\partial r}{\partial n} - (1-2\nu)\left(r_{,i}n_j - r_{,j}n_i\right)\right\},$$

$$\begin{aligned} r &= \left(x_i - x_i'\right)^{1/2}, \\ r_i &= x_i - x_i', \\ r_{,i} &= \frac{\partial r}{\partial x_i} = \frac{r_i}{r}, \\ n_i &= \text{Normal vector}, \\ \delta_{ij} &= \text{Kronecker delta}, \\ G &= \text{Shear modulus}, \\ \nu &= \text{Poisson's ratio}. \end{aligned} \tag{48}$$

The boundary Γ is assumed to be smooth as shown in Fig. 6 because the constant ½ depends on the smoothness of the boundary.

Let us consider a mixed boundary-value problem first. For the sake of simplicity, let us suppose that displacements are prescribed along a part of Γ denoted by Γ_1 and tractions are prescribed along the remaining boundary denoted by Γ_2, so that $\Gamma = \Gamma_1 + \Gamma_2$. After we move the unknown displacement and traction terms on the left side of (47) and the known displacement and traction terms on the right, we obtain

$$\begin{aligned} &\frac{1}{2}u_i(x') + \int_{\Gamma_2} T_{ij}(x,x')u_j(x)ds(x) - \int_{\Gamma_1} U_{ij}(x,x')t_j(x)ds(x) \\ &\qquad = -\int_{\Gamma_1} T_{ij}(x,x')u_j(x)ds(x) + \int_{\Gamma_2} U_{ij}(x,x')t_j(x)ds(x), \end{aligned} \tag{49}$$

where the position of the first term on the left-hand side is not necessarily on this side. If x' is on Γ_1, this term moves over to the right-hand side.

In general, these integrations are carried out numerically, and the one of the most common techniques associated with integration is to discretize (subdivide) the domain of integration into smaller subdomains or elements. Then (49) is rewritten as

$$\frac{1}{2}u_i(x') + \sum_{n=M+1}^{M+N} \int_{\Gamma_2^{(n)}} T_{ij}\left(x_{(n)}, x'\right) u_j\left(x_{(n)}\right) ds\left(x_{(n)}\right) - \sum_{n=1}^{M} \int_{\Gamma_1^{(n)}} U_{ij}\left(x_{(n)}, x'\right) t_j\left(x_{(n)}\right) ds\left(x_{(n)}\right)$$
$$= -\sum_{n=1}^{M} \int_{\Gamma_1^{(n)}} T_{ij}\left(x_{(n)}, x'\right) u_j\left(x_{(n)}\right) ds\left(x_{(n)}\right) + \sum_{n=M+1}^{M+N} \int_{\Gamma_2^{(n)}} U_{ij}\left(x_{(n)}, x'\right) t_j\left(x_{(n)}\right) ds\left(x_{(n)}\right), \qquad (50)$$

in which Γ_1 and Γ_2 are divided into M and N elements, respectively. We apply a Qth order numerical integration technique to (50), but instead of giving the values of the displacements and the tractions at each sample point exactly, we approximate these values by based on P values in each element, that is, we appriximate the displacements and tractions in each element by

$$\begin{aligned} u_i\left(x(\xi)\right) &= \sum_{m=1}^{P} S^{(m)}(\xi) u_i\left(x^{(m)}\right), \\ t_i\left(x(\xi)\right) &= \sum_{m=1}^{P} S^{(m)}(\xi) t_i\left(x^{(m)}\right), \qquad -1 \le \xi \le 1, \end{aligned} \qquad (51)$$

where the function S is called the shape function. After we substitute (51) into (50), we carry out the integration and obtain

$$
\begin{aligned}
\frac{1}{2}u_i(x') &+ \sum_{n=M+1}^{M+N}\sum_{k=1}^{Q}\sum_{m=1}^{P} T_{ij}\left(x_{(n)}\left(\xi^{(k)}\right),x'\right)S^{(m)}\left(\xi^{(k)}\right)u_j\left(x_{(n)}^{(m)}\right)J\left(x_{(n)}\left(\xi^{(k)}\right)\right) \\
&-\sum_{n=1}^{M}\sum_{k=1}^{Q}\sum_{m=1}^{P} U_{ij}\left(x_{(n)}\left(\xi^{(k)}\right),x'\right)S^{(m)}\left(\xi^{(k)}\right)t_j\left(x_{(n)}^{(m)}\right)J\left(x_{(n)}\left(\xi^{(k)}\right)\right) \\
&= -\sum_{n=1}^{M}\sum_{k=1}^{Q}\sum_{m=1}^{P} T_{ij}\left(x_{(n)}\left(\xi^{(k)}\right),x'\right)S^{(m)}\left(\xi^{(k)}\right)u_j\left(x_{(n)}^{(m)}\right)J\left(x_{(n)}\left(\xi^{(k)}\right)\right) \\
&\quad + \sum_{n=M+1}^{M+N}\sum_{k=1}^{Q}\sum_{m=1}^{P} U_{ij}\left(x_{(n)}\left(\xi^{(k)}\right),x'\right)S^{(m)}\left(\xi^{(k)}\right)t_j\left(x_{(n)}^{(m)}\right)J\left(x_{(n)}\left(\xi^{(k)}\right)\right). \qquad (52)
\end{aligned}
$$

In the case of the constant approximation ($P=1$), there are $2(M+N)$ unknowns (displacements and tractions) as shown in Fig. 7, and we require the same number of equations in order to solve for them. Because at each x' we can construct two equations, we choose x' at the same points as x (see Fig. 7). Moreover, because the displacements and tractions are given on the right-hand side of (52), we can simplify the right-hand side terms. If we write (52) in matrix form it becomes

$$
[\mathbf{T} \quad -\mathbf{U}]\begin{Bmatrix}\mathbf{u}\\ \mathbf{t}\end{Bmatrix} = \mathbf{b}, \qquad (53)
$$

or even more simply,

$$
\mathbf{A}\mathbf{x} = \mathbf{b}, \qquad (54)
$$

where

$$
\begin{aligned}
\mathbf{A} &= [\mathbf{T} \quad -\mathbf{U}], \\
\mathbf{x} &= \{\mathbf{u} \quad \mathbf{t}\}^T.
\end{aligned} \qquad (55)
$$

If the coefficient matrix **A** is well-conditioned, **x** can be solved by a simple technique like the Gauss elimination. This is the starndard boundary element method solution.

10. Cauchy Problems in Linear Elasticity

We now examine some Cauchy problems in isotropic linear elasticity. Let us first consider a general problem. We can modify the problem in the previous section and state that both displacements and tractions are prescribed along Γ_1 and no values are prescribed along Γ_2 (free boundary). Then we have to modify (49) as

$$\frac{1}{2}u_i(x') + \int_{\Gamma_2} T_{ij}(x,x')u_j(x)ds(x) - \int_{\Gamma_2} U_{ij}(x,x')t_j(x)ds(x)$$
$$= -\int_{\Gamma_1} T_{ij}(x,x')u_j(x)ds(x) + \int_{\Gamma_1} U_{ij}(x,x')t_j(x)ds(x). \qquad (56)$$

When (56) is discretized as (49) was discretized into (52) then into (54), it again becomes the same form as (54). However, under the constant assumption the total number of unknowns in this case is $4N$ (2 displacements and 2 tractions at each point), and the total number of equations is still $2(M+N)$. Therefore, the coefficient matrix **A** is nonsquare, and we cannot employ a simple technique to solve the simultaneous equations.

We might be tempted to choose $M = N$ so that the coefficient matrix to be square, but this scheme usually does not work for the following reason. Suppose Γ_1 covers only 1% of the entire boundary and the free boundary Γ_2 covers the rest. In this case, even if we construct a square coefficient matrix by taking $M = N$, it is still highly singular unless the elastic domain and the loading have a high degree of symmetry. In general, however, this is not the case.

To overcome the difficulty of constructing a nonsingular square matrix we require special techniques such as the regularization method and the least-squares method. Once the integral equation (56) has been converted into the form (54), the procedure is identical as explained in Sections 7 and 8.

Sample Problem 1

We employ the least-squares method discussed in Section 8 to solve the following problem. The upper half of a circular disk of radius 1m is under radial pressure of 2MPa as shown in Fig. 4. The center of the disk is fixed and its Young's modulus and Poisson's ratio are 500MPa and 0.3, respectively. The displacements along the upper half boundary are given as

$$\begin{aligned} u_x &= \frac{1}{325}\cos(\theta)\,\mathrm{m}, \\ u_y &= \frac{1}{325}\sin(\theta)\,\mathrm{m}, \qquad (0 \le \theta \le \pi). \end{aligned} \tag{58}$$

From these information, we would like to compute the displacements and tractions along the boundary of the lower half of the disk.

The exact solutions are

$$\begin{aligned} u_x &= \frac{1}{325}\cos(\theta)\,\mathrm{m}, \\ u_y &= \frac{1}{325}\sin(\theta)\,\mathrm{m}, \\ t_x &= 2\cos(\theta)\,\mathrm{MPa}, \\ \mathrm{t}_y &= 2\sin(\theta)\,\mathrm{MPa}, \qquad (\pi \le \theta \le 2\pi). \end{aligned} \tag{59}$$

We use 40 equal length constant elements for the prescribed and free boundaries. The prescribed boundary Γ_1 is along $(0 \le \theta \le \pi)$ and the free boundary Γ_2 is along $(\pi < \theta < 2\pi)$. After we substitute them into (56) and convert into a form of (54), and apply the least-squares method, we obtain the results as shown in Figs. 8–11.

We notice that even though the solutions seem to agree with the exact solutions, there are still significant discrepancies between them. We investigate

cause of this discrepancies a little further. Suppose we solve a mixed boundary-value problem of the same elastic body with the following boundary conditions:

$$\begin{aligned} u_x &= 0 \text{ at } \theta = \pi/2 \text{ and } 3\pi/2, \\ u_y &= 0 \text{ at } \theta = 0 \text{ and } \pi, \\ t_x &= 2\cos(\theta)\,\text{MPa}, \\ t_y &= 2\sin(\theta)\,\text{MPa}, \qquad (0 \le \theta < 2\pi). \end{aligned} \tag{60}$$

We use the same discretization as before. Then we obtain the results as shown in Fig. 12. It seems to indicate that for the current discretization the displacements in (58) are not compatible with the given tractions. It seems to make more sense to prescribe the displacements obtained from this mixed boundary-value problem in place of (58). The results of solving this Cauchy problem are shown in Figs. 13–16. The results are in better agreement.

Sample Problem 2

A side $(x = 1/2)$ of a thin square plate of side 1m is pulled by a uniform traction of 10,000Pa as shown in Fig. 17. The displacements along this side is measured Young's modulus and Poisson's ratio are 30MPa and 0.25, respectively. We would like to compute the displacements and tractions along the remaining sides.

In this problem, the measured displacements are the displacement solutions for the mixed boundary-value problem in which the boundary conditions are given by

$$
\begin{aligned}
&u_x = 0 \text{ at } x = 0, \\
&u_y = 0 \text{ everywhere} \\
&t_x = 100 \text{ Pa at } (x = \pm 1/2, -1/2 \le y \le 1/2), \\
&t_x = 0 \text{ at } (-1/2 < x < 1/2, y = \pm 1/2), \\
&t_y = 0 \text{ at } (x = \pm 1/2, -1/2 \le y \le 1/2).
\end{aligned} \tag{61}
$$

Unlike the circular disk in the previous problem, this plate has sharp corners (geometric singularities). We would like to see how the least squares method works with this type of irregularity (discontinuity). Figs. 18–21 show the results, and we see that the results are not as good as ones for the previous problem. The farther away is the point of interest, the worse become the solutions.

Sample Problem 3

A circular elastic disc embedded in another thin elastic body and loaded as shown in Fig. 22. The boundary of the outer elastic body is composed of straight lines denoted by ①, ②, ③, ④, and ⑤. Suppose the Cauchy data (displacements and tractions) are prescribed along ① and ⑤. We would like to compute the remaining boundary values. The Cauchy data are the displacements and tractions computed by solving the corresponding mixed boundary-value problem. A total of 144 constant boundary elements are used. The resulting deformation is shown in Fig. 23. The Cauchy solution agree with the mixed boundary-value solution.

Conclusions

Cauchy problems in linear isotropic elasticity are solvable although not directly by means of the regularization method as well as the least-squares method coupled with the singular value decomposition. Unlike the regular boundary-value problem, the Cauchy problem is very sensitive to compatibility

among the Cauchy data. Feeding the exact solution does not necessarily guarantee a good solution. The accuracy depends heavily on how the body in equation is discretized. The Nystrom type solution simplifies implementation on computer and improves performance.

Acknowledgments

The authors would like to thank Prof. Z. Gao of Clarkson University, Pro. W. D. Yeih of National Ocean University in Taiwan, and Mr. S. C. Hsieh for their valuable advice and discussions. The authors would also like to express gratitude to the editors for their cooperation and patience. This research is supported by U. S. Air Force under Grant no. AFOSR-89-0269.

References

[1] I Stakgold, Mathematical Physics, Vol. 1, Macmillan (1967).

[2] Z. Gao and T. Mura, Inversion of residual stress from surface displacements, J. Appl. Mech., 54 (1989) 508–513.

[3] W. Yeih, T. Koya, and T. Mura, "An inverse problems in elasticity with partially overprescribed boundary conditions, Part I: Theoretical Approach, To be published from J. Appl. Mech.

[4] W. Yeih, T. Koya, and T. Mura, "An inverse problems in elasticity with partially overprescribed boundary conditions, Part II: Numerical details, To be published from J. Appl. Mech.

[5] R. Courant and D. Hilbert, Methods of Mathematical Physics, Vol. 1, Interscience (1953).

[6] A. N. Tikhonov and A. V. Goncharsky (eds.) Ill-Posed Problems in the Natural Sciences, MIR (1987).

[7] A. M. Legendre, Nouvelles Methodes pour la Determination des Orbites des Cometes, Courcier, Paris, (1806).

[8] C. F. Gauss, Theorie motus corporum coelestium in sectionibus conicis solem ambientium, F. Perthes et I. H. Besser, Hamburgi, (1809).

[9] H. Sobieczky, Research on inverse design and optimization in Germany, Appl. Mech. Rev., 41 (1988) 239–246.

[10] H. Stanitz, A review of certain inverse problem methods for the design of ducts with 2- or 3- dimensional potential flow, Appl. Mech. Rev., 41 (1988) 217–238.

[11] E. Alamansi, Un teorema sulle deformazioni elastiche dei solidi isotropi," Atti R. Accad. Lincei Rend. Cl. Sci. Fis. Mat. Natur. (Ser 5) 16 (1907), 865–867.

[12] L. M. Delves and J. L. Mohamed, *Computational Methods for Integral Equations,* Cambridge Univ. Press (1985).

[13] M. Tsuji, *Potential Theory in Modern Function Theory,* Maruzen, Tokyo (1959).

[14] T. Mura and T. Koya, *Variation Methods in Mechanics,* Oxford Univ. Press (1992).

[15] G. H. Golub, C. F. van Loan, *Matrix Computations,* 2nd ed., Johns Hopkins Univ. Press (1989).

[16] C. A. Brebbia, J. C. F. Telles, and L. C. Wrobel, *Boundary Element Techniques,* Springer-Verlag (1984).

Figure Captions

Figure 1. A regular boundary-value problem.
Figure 2. A Cauchy problem.
Figure 3. A regular elasticity boundary-value problem.
Figure 4. A elasticity Cauchy problem.
Figure 5. The Nystrom solution comparison.
Figure 6. The parameters in Somigliana's boundary integral equation.
Figure 7. A discretized boundary.
Figure 8. The Cauchy solution for the x displacement.
Figure 9. The Cauchy solution for the y displacement.
Figure 10. The Cauchy solution for the x traction.
Figure 11. The Cauchy solution for the y traction.
Figure 12. The inherent errors in discretization.
Figure 13. A more compatible Cauchy solution for the x displacement.
Figure 14. A more compatible Cauchy solution for the y displacement.
Figure 15. A more compatible Cauchy solution for the x traction.
Figure 16. A more compatible Cauchy solution for the x traction.
Figure 17. A thin square plate under load.
Figure 18. The Cauchy solution for the x displacement.
Figure 19. The Cauchy solution for the y displacement.
Figure 20. The Cauchy solution for the x traction.
Figure 21. The Cauchy solution for the y traction.
Figure 22. A more complicated problem.
Figure 23. The Cauchy solution for deformation.

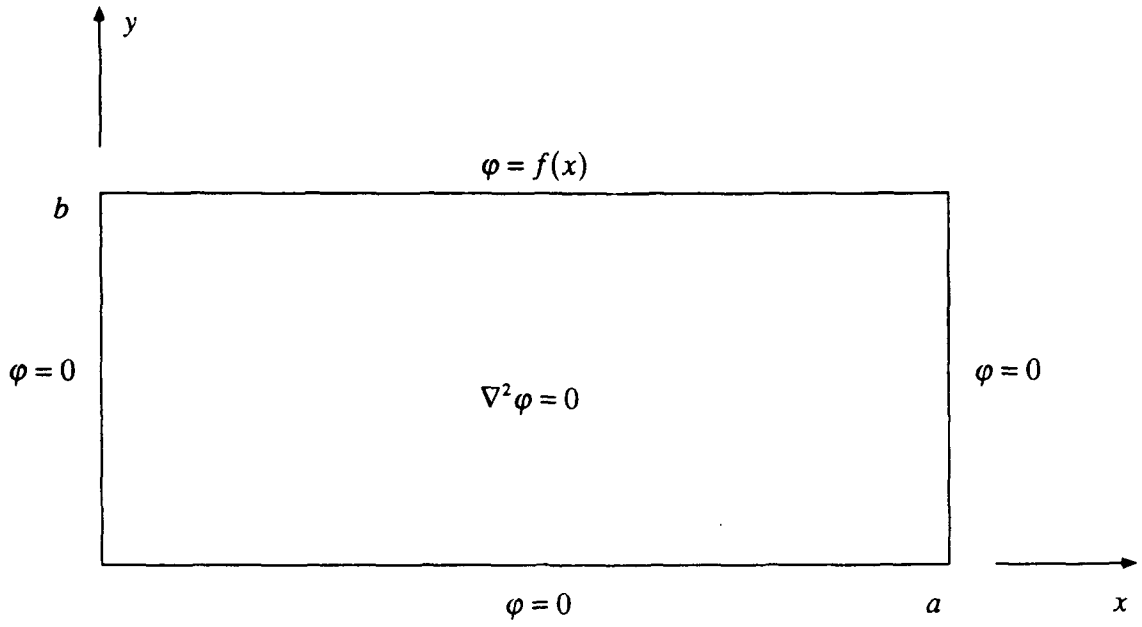

Figure 1

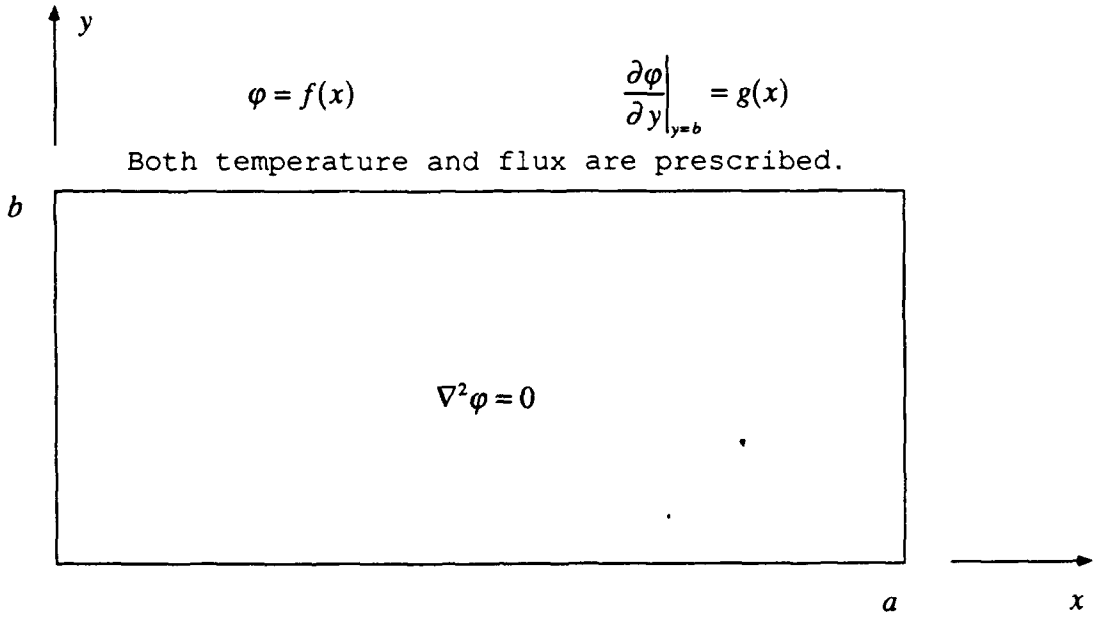
y
$\varphi = f(x)$
$\left.\frac{\partial \varphi}{\partial y}\right|_{y=b} = g(x)$
Both temperature and flux are prescribed.
b
$\nabla^2 \varphi = 0$
a
x

Figure 2

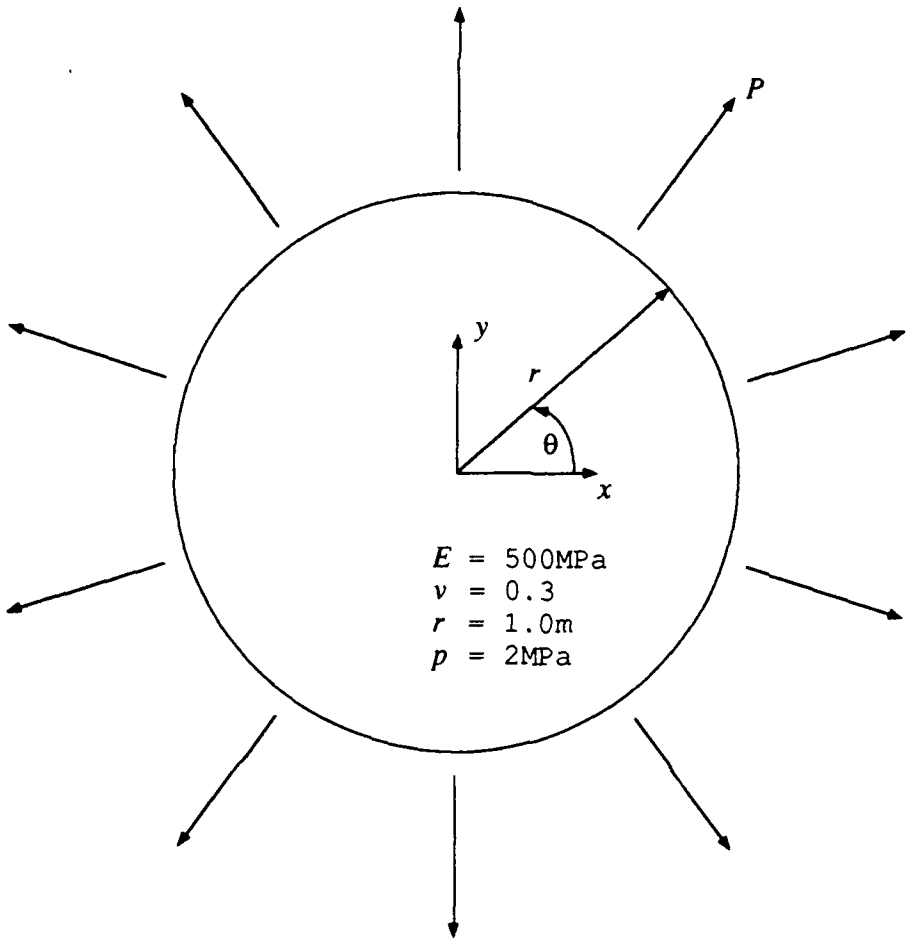

Figure 3

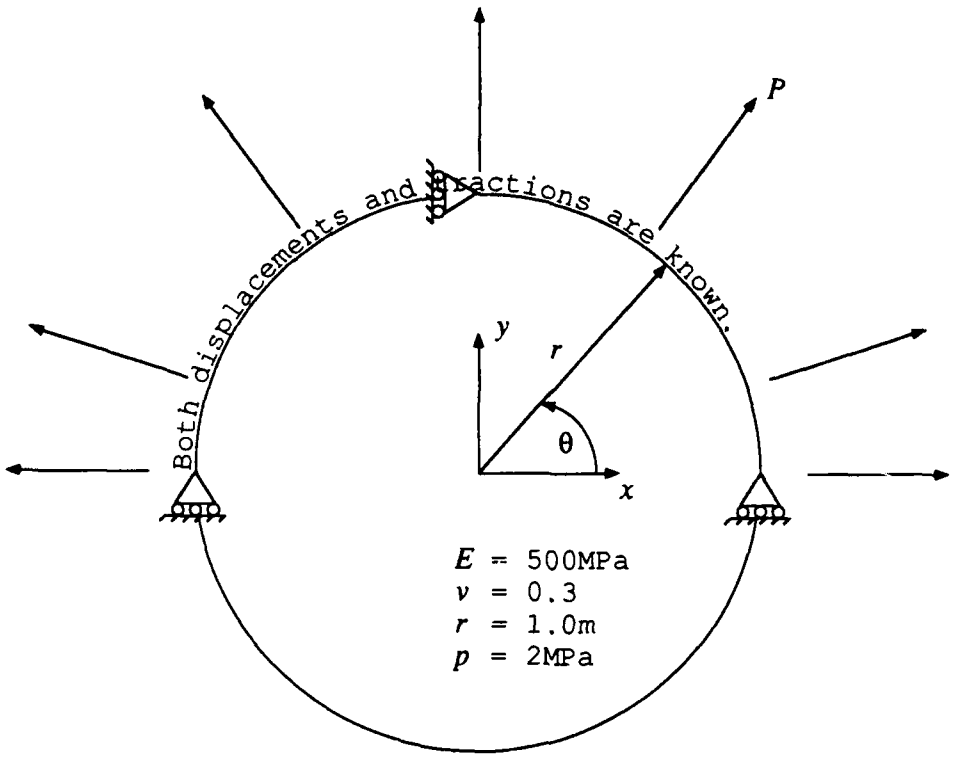
P
Both displacements and tractions are known.
y
r
θ
x
E = 500MPa
ν = 0.3
r = 1.0m
p = 2MPa

Figure 4

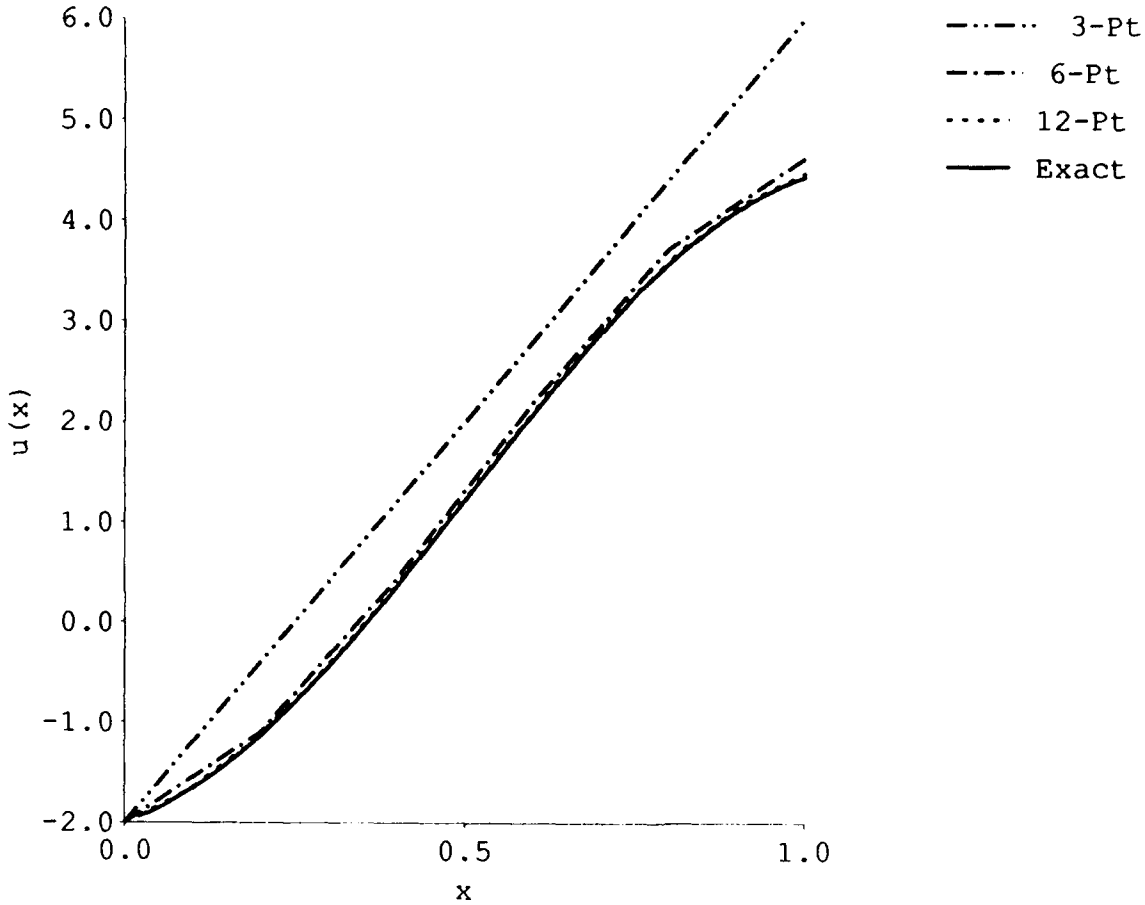

Figure 5

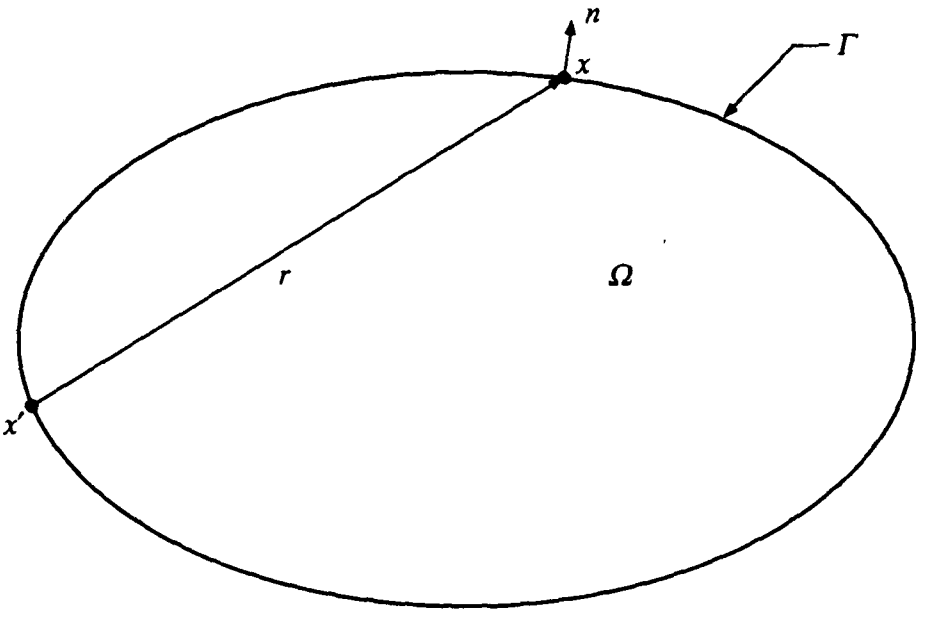

Figure 6

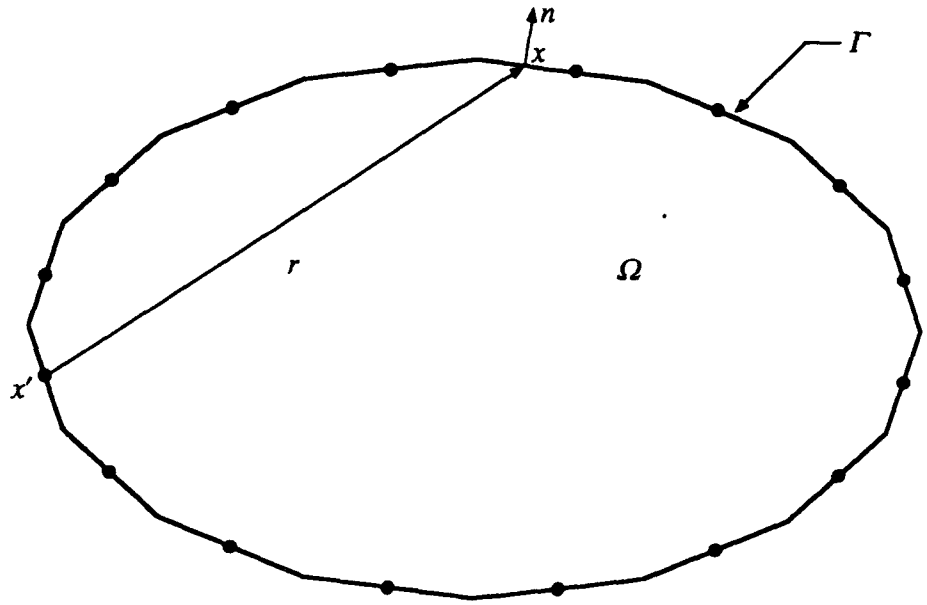

Figure 7

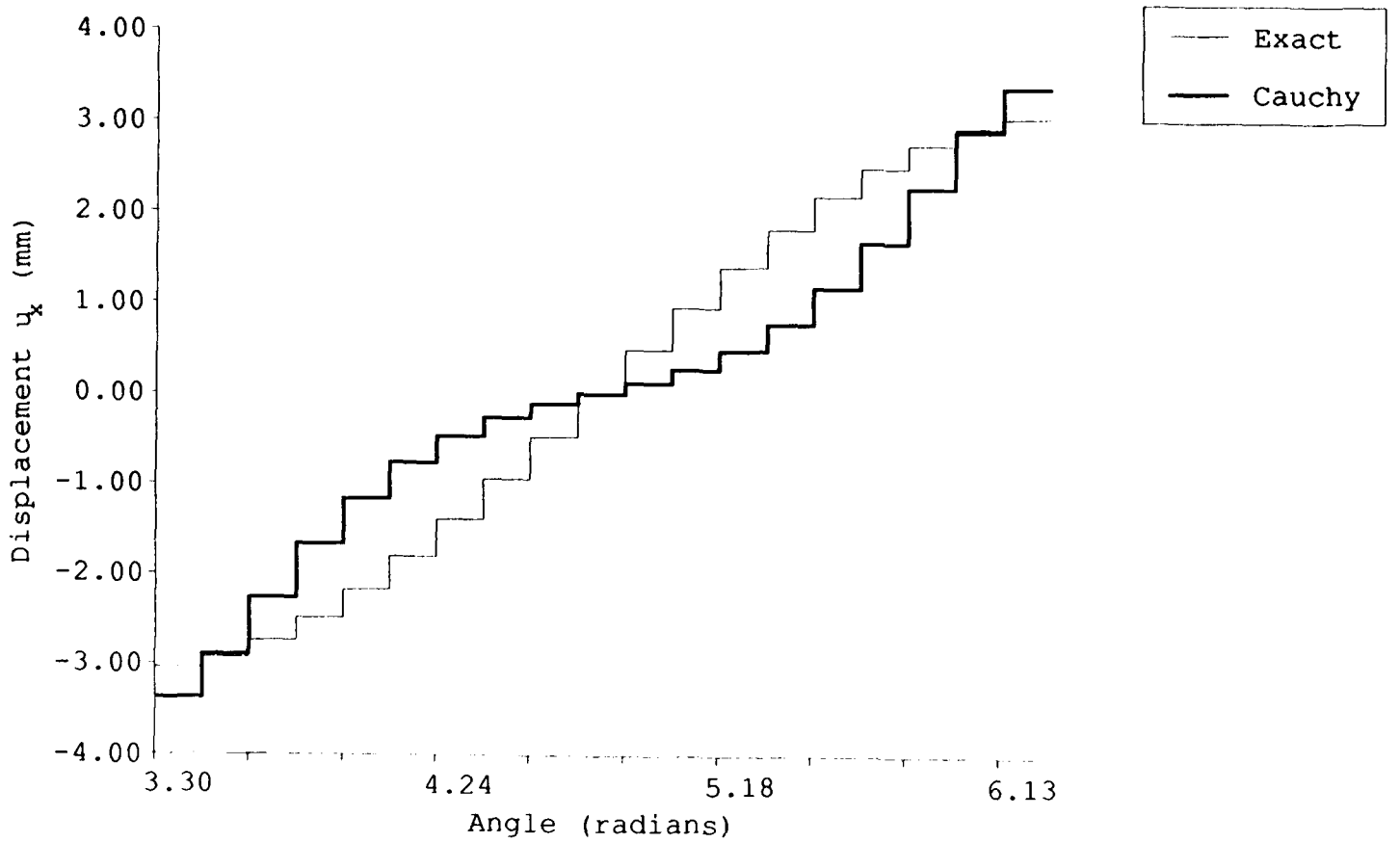
4.00
3.00
2.00
1.00
0.00
-1.00
-2.00
-3.00
-4.00
Displacement u_x (mm)
3.30
4.24
5.18
6.13
Angle (radians)
Exact
Cauchy

Figure 8

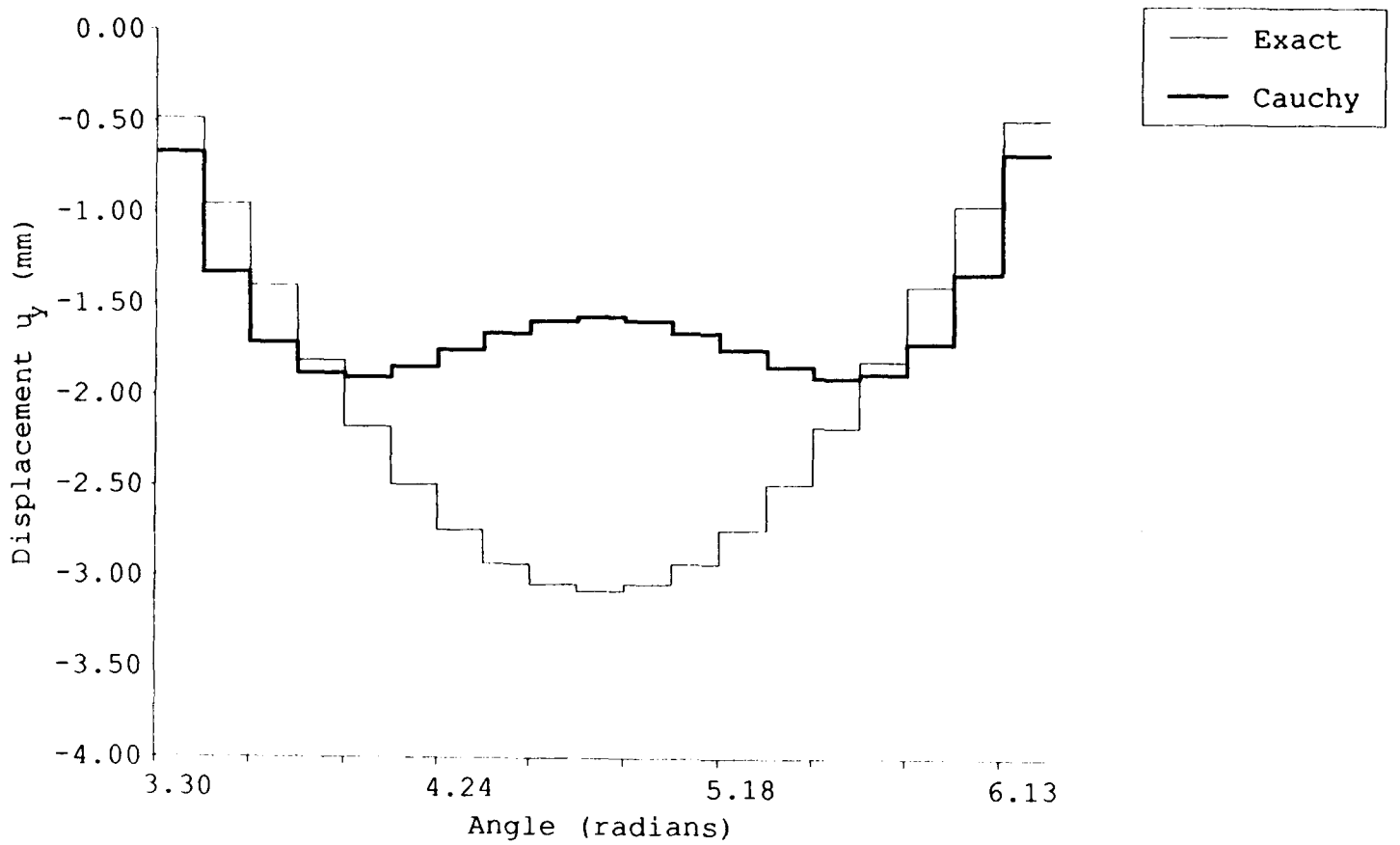
0.00
-0.50
-1.00
-1.50
-2.00
-2.50
-3.00
-3.50
-4.00
Displacement u_y (mm)
3.30
4.24
5.18
6.13
Angle (radians)
Exact
Cauchy

Figure 9

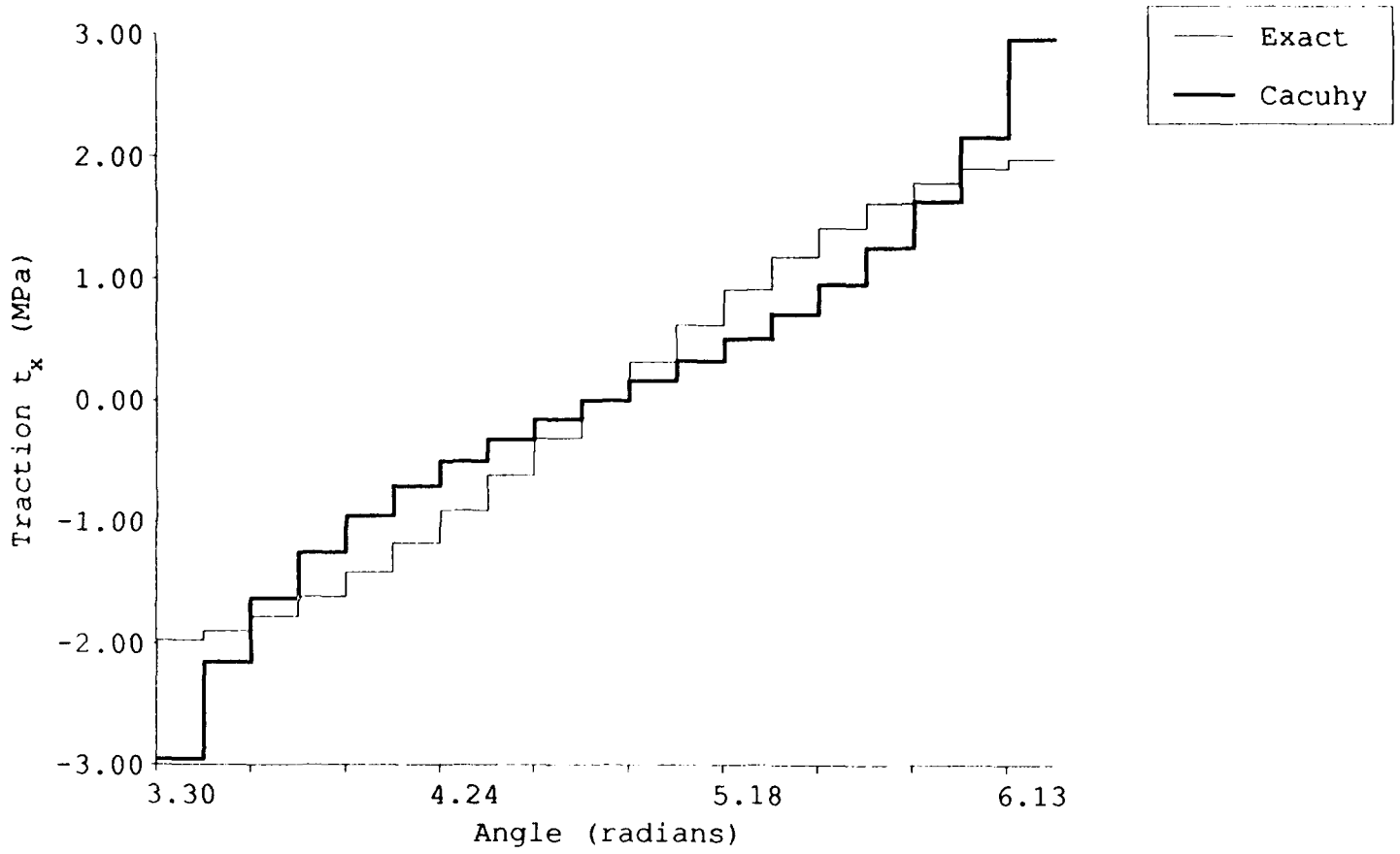
3.00
2.00
1.00
0.00
-1.00
-2.00
-3.00
Traction t_x (MPa)
3.30
4.24
5.18
6.13
Angle (radians)
Exact
Cacuhy

Figure 10

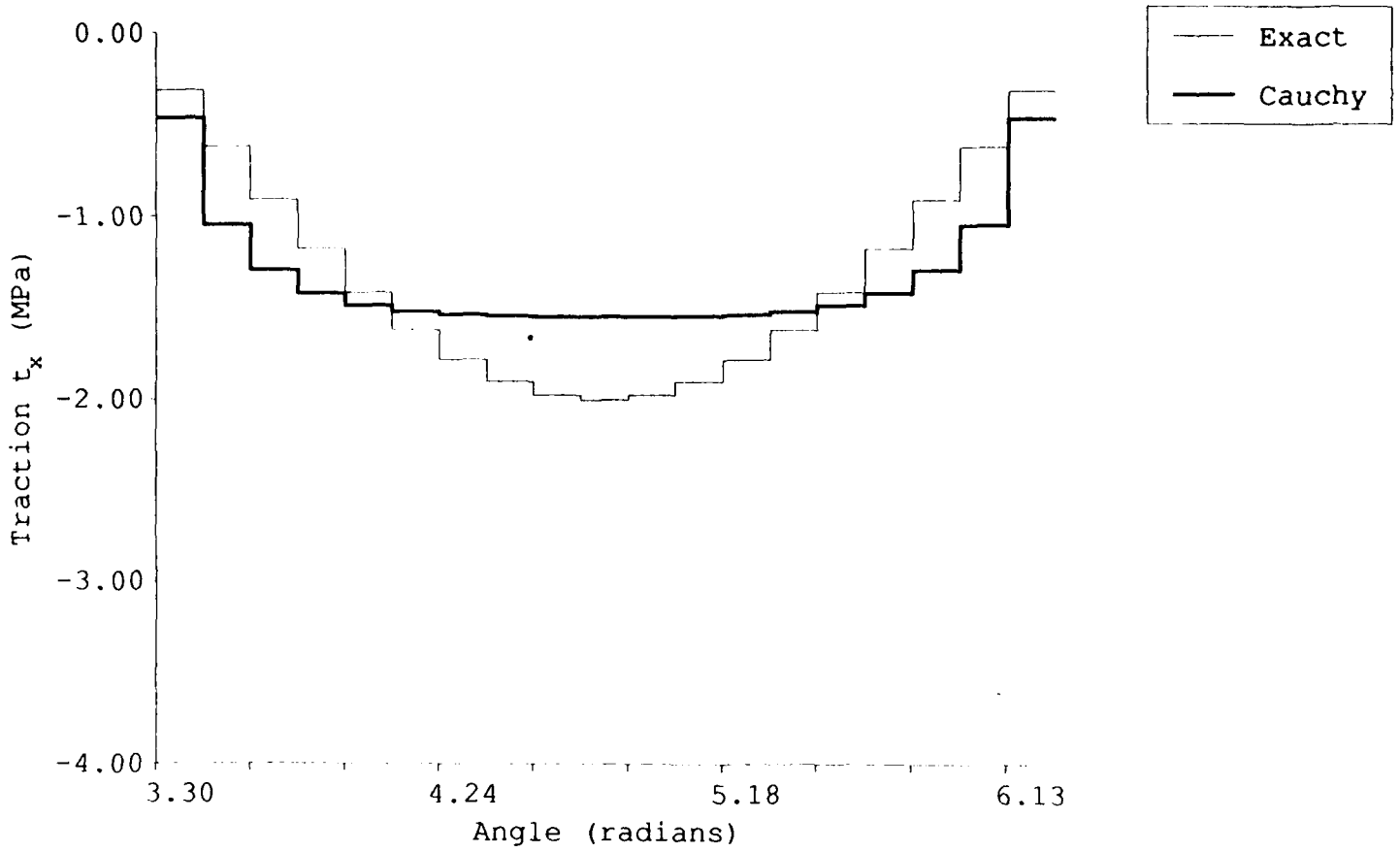
0.00
-1.00
-2.00
-3.00
-4.00
Traction t_x (MPa)
3.30
4.24
5.18
6.13
Angle (radians)
Exact
Cauchy

Figure 11

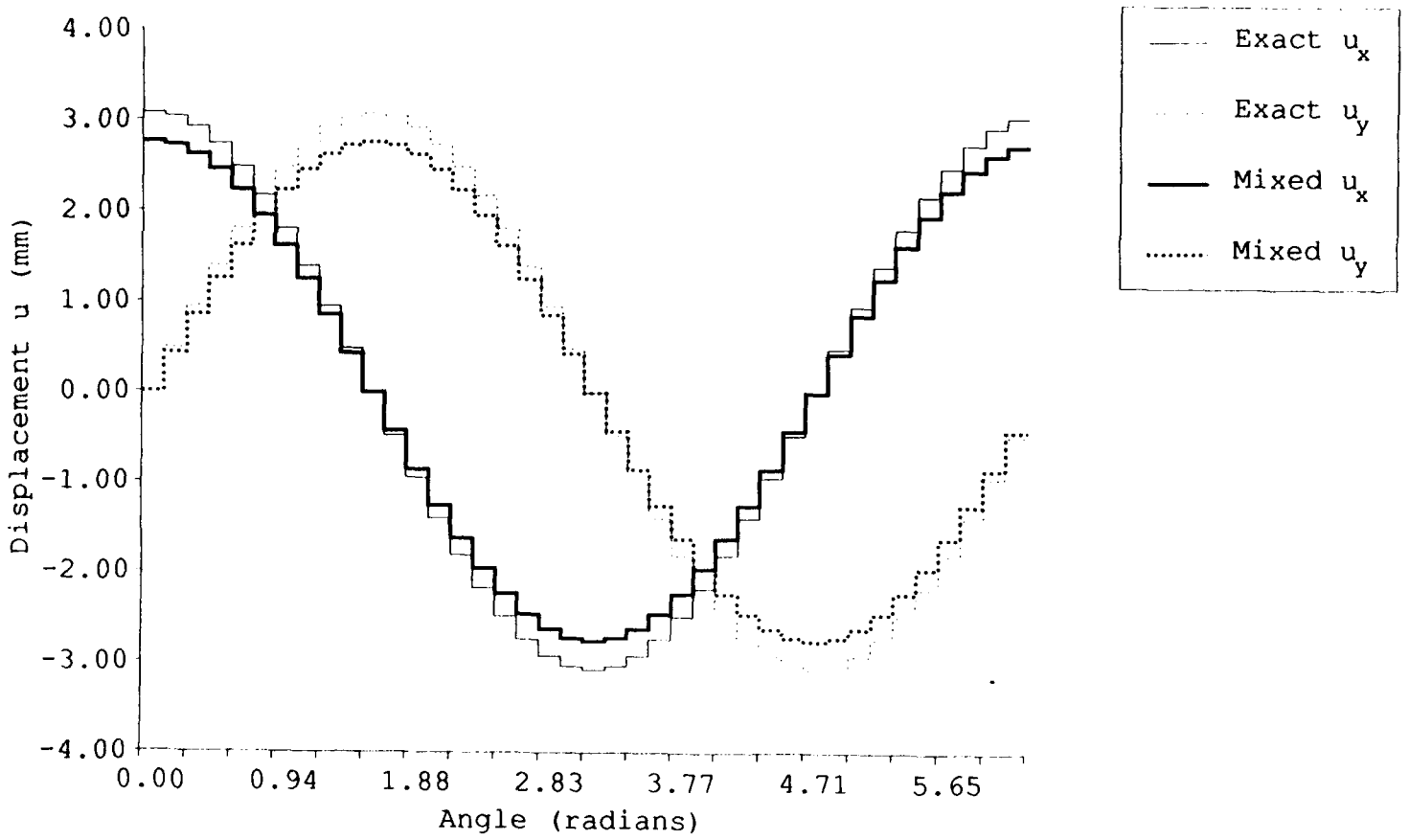
4.00
3.00
2.00
1.00
0.00
-1.00
-2.00
-3.00
-4.00
Displacement u (mm)
0.00
0.94
1.88
2.83
3.77
4.71
5.65
Angle (radians)
Exact u_x
Exact u_y
Mixed u_x
Mixed u_y

Figure 12

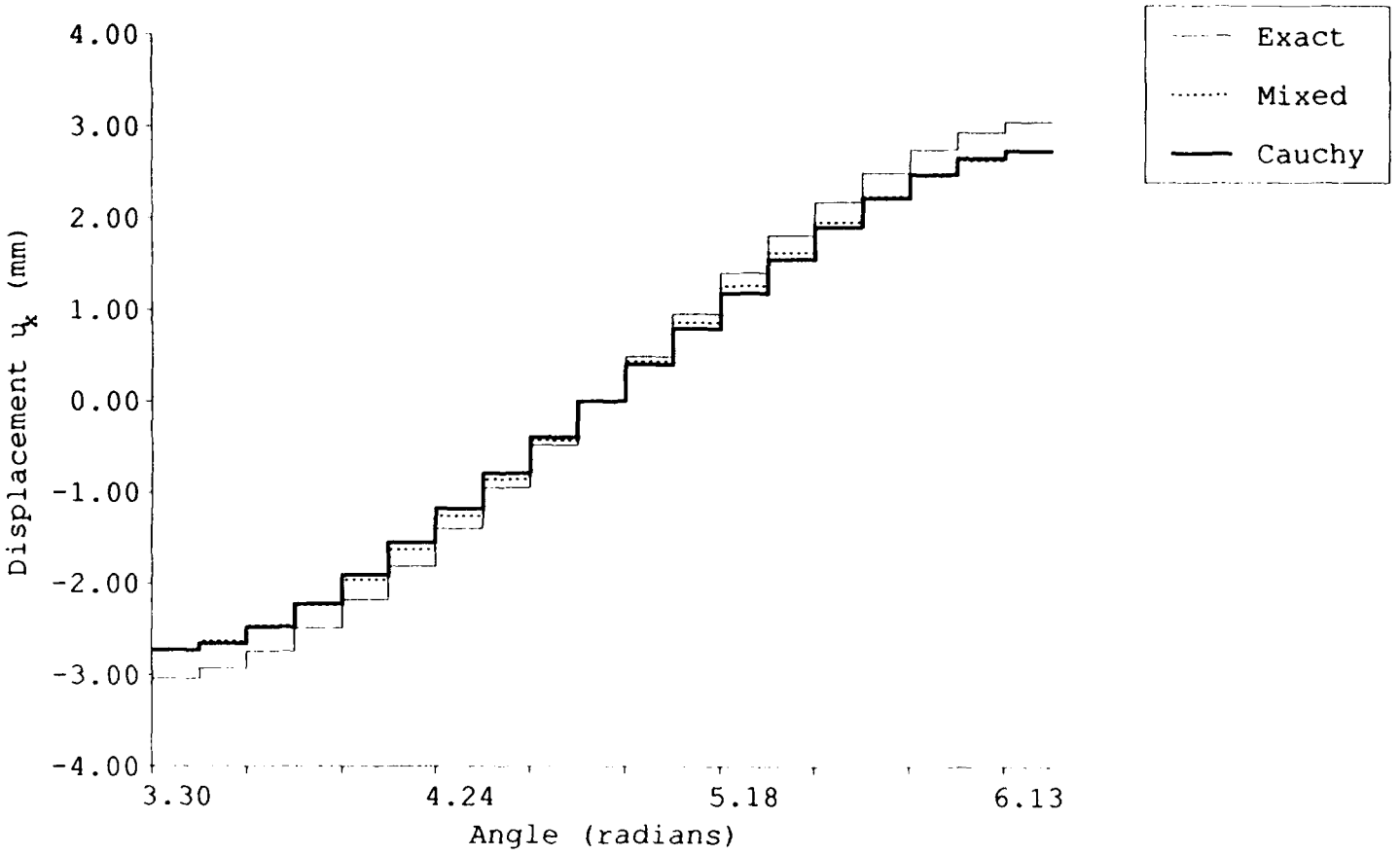
4.00
3.00
2.00
1.00
0.00
-1.00
-2.00
-3.00
-4.00
Displacement u_x (mm)
3.30
4.24
5.18
6.13
Angle (radians)
Exact
Mixed
Cauchy

Figure 13

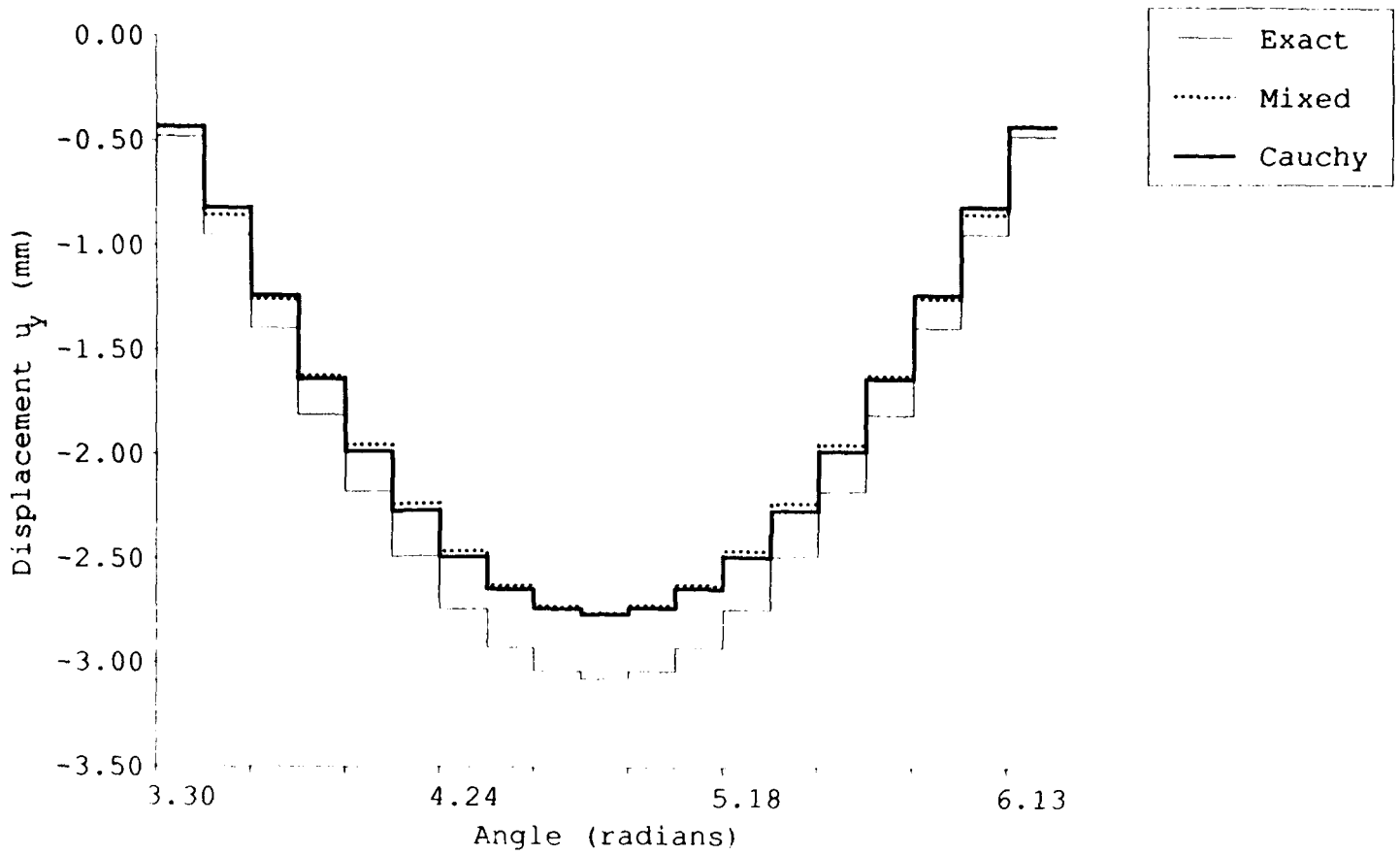
0.00
-0.50
-1.00
-1.50
-2.00
-2.50
-3.00
-3.50
Displacement u_y (mm)
3.30
4.24
5.18
6.13
Angle (radians)
Exact
Mixed
Cauchy

Figure 14

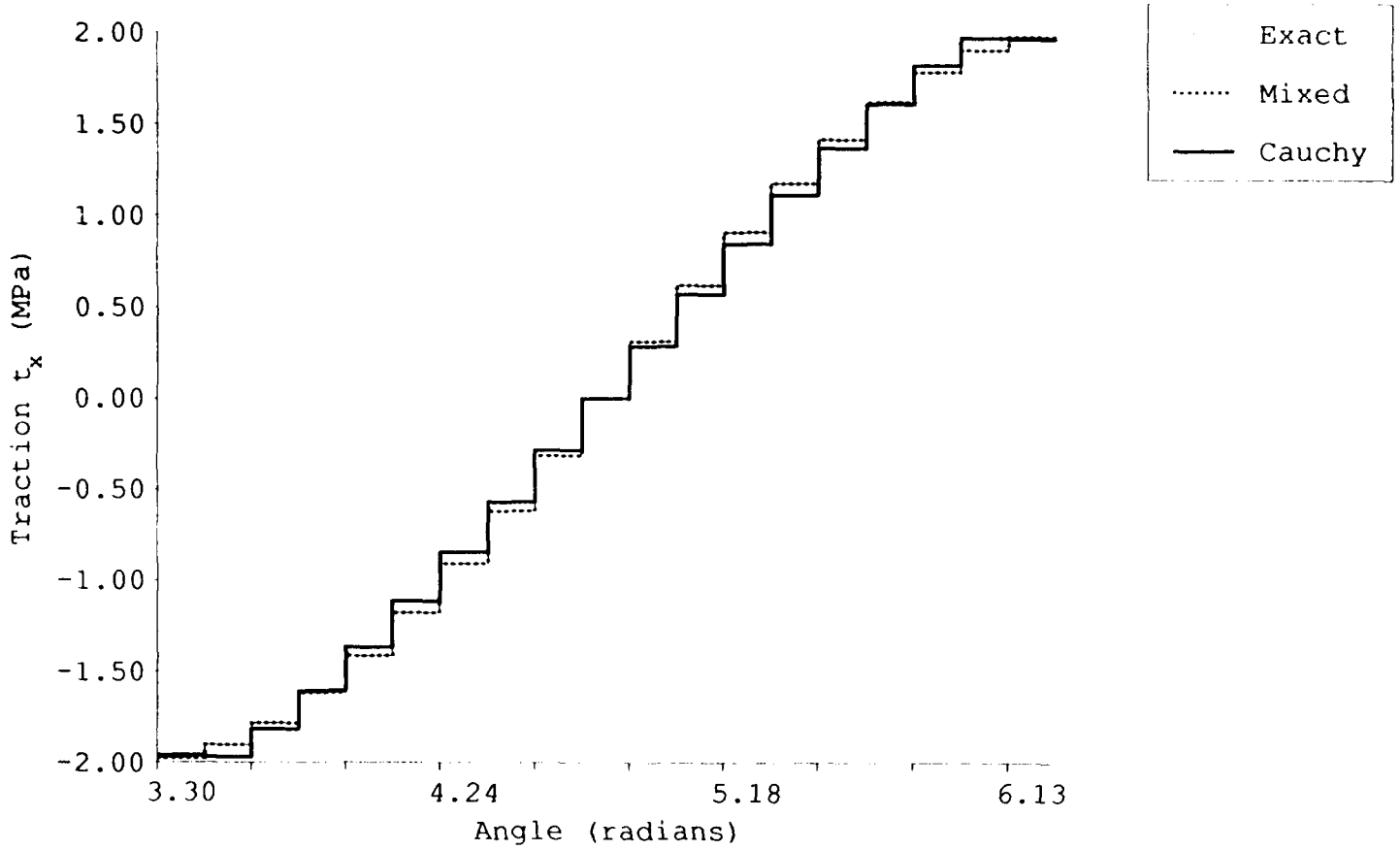
2.00
1.50
1.00
0.50
0.00
-0.50
-1.00
-1.50
-2.00
Traction t_x (MPa)
3.30
4.24
5.18
6.13
Angle (radians)
Exact
Mixed
Cauchy

Figure 15

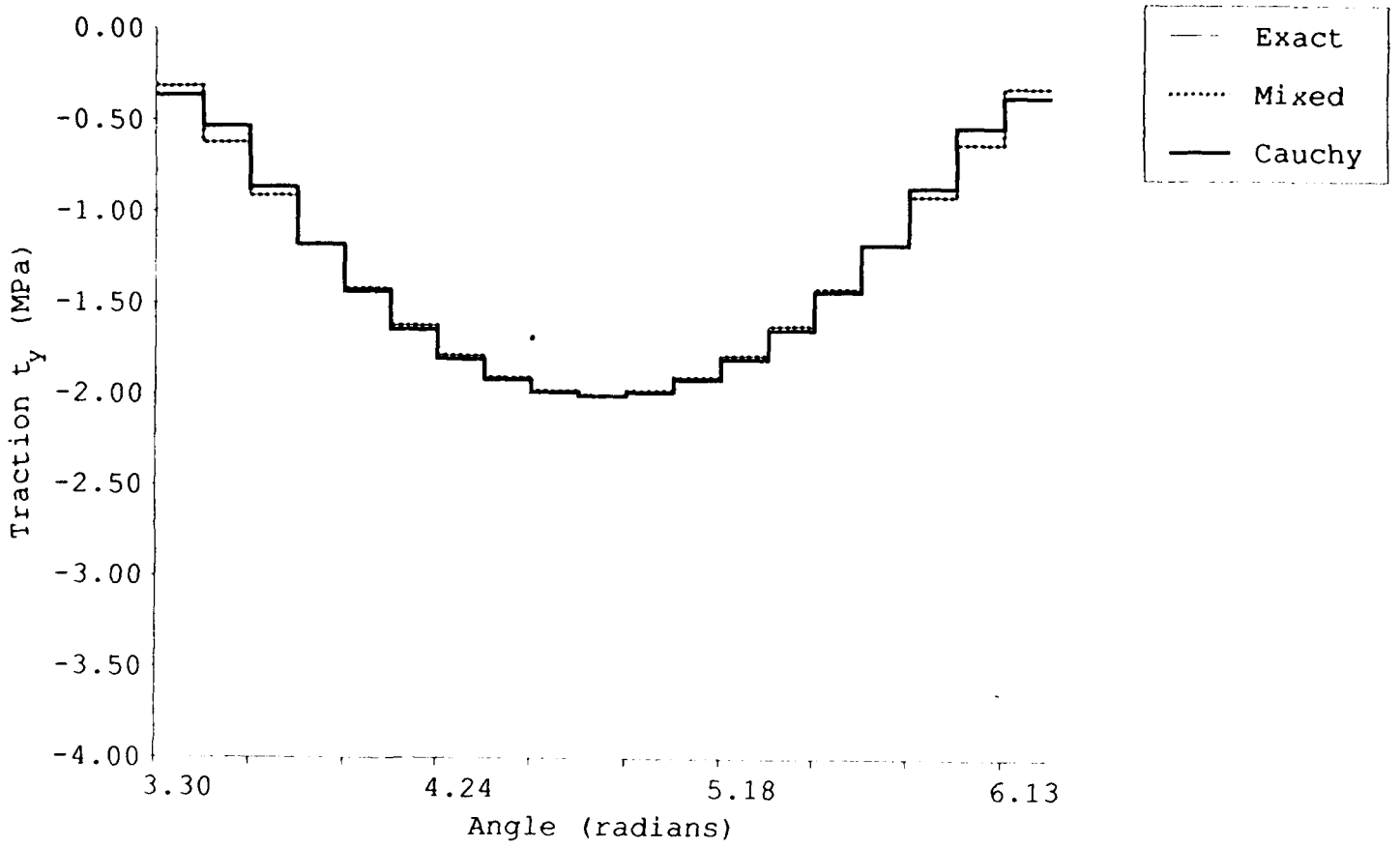
0.00
-0.50
-1.00
-1.50
-2.00
-2.50
-3.00
-3.50
-4.00
Traction t_y (MPa)
3.30
4.24
5.18
6.13
Angle (radians)
Exact
Mixed
Cauchy

Figure 16

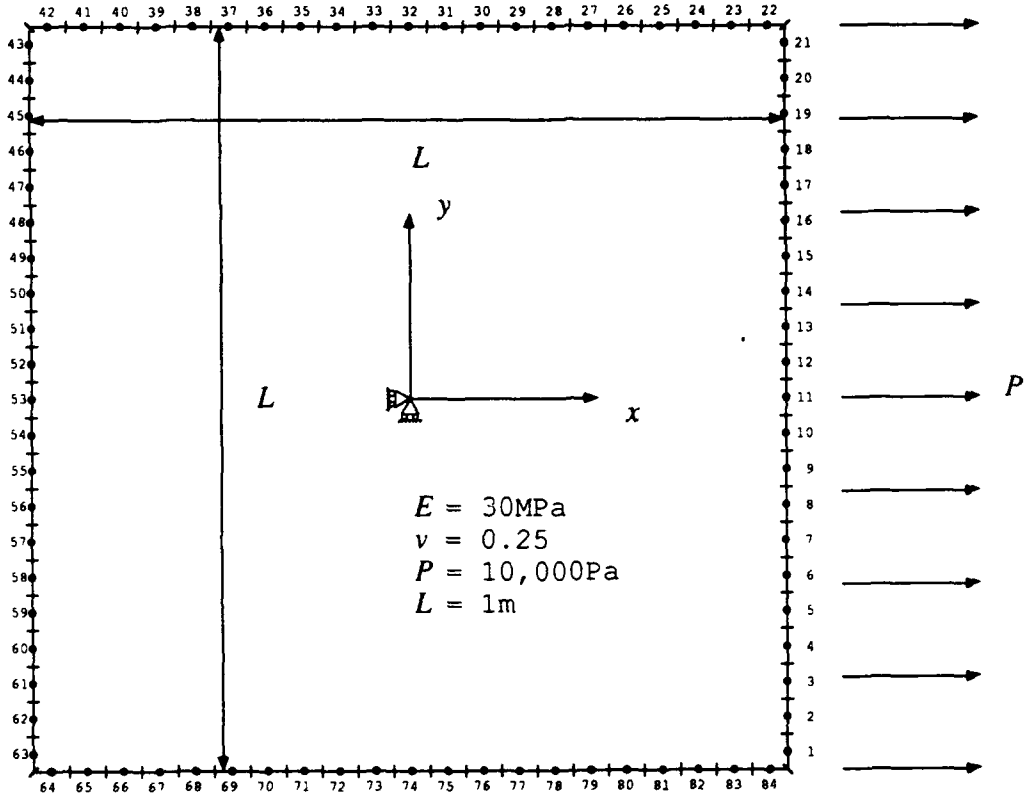

Figure 17

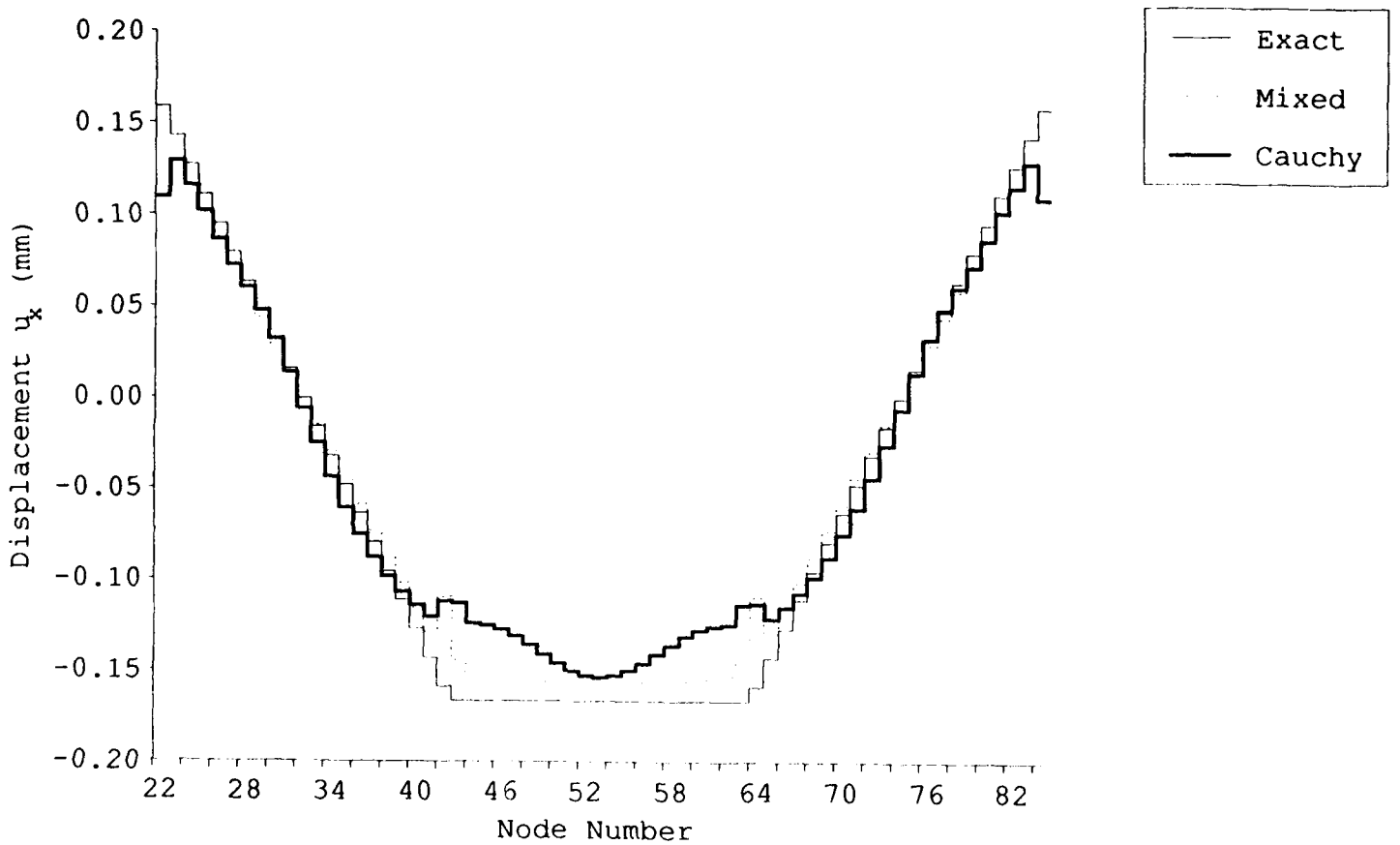
0.20
0.15
0.10
0.05
0.00
-0.05
-0.10
-0.15
-0.20
Displacement u_x (mm)
22
28
34
40
46
52
58
64
70
76
82
Node Number
Exact
Mixed
Cauchy

Figure 18

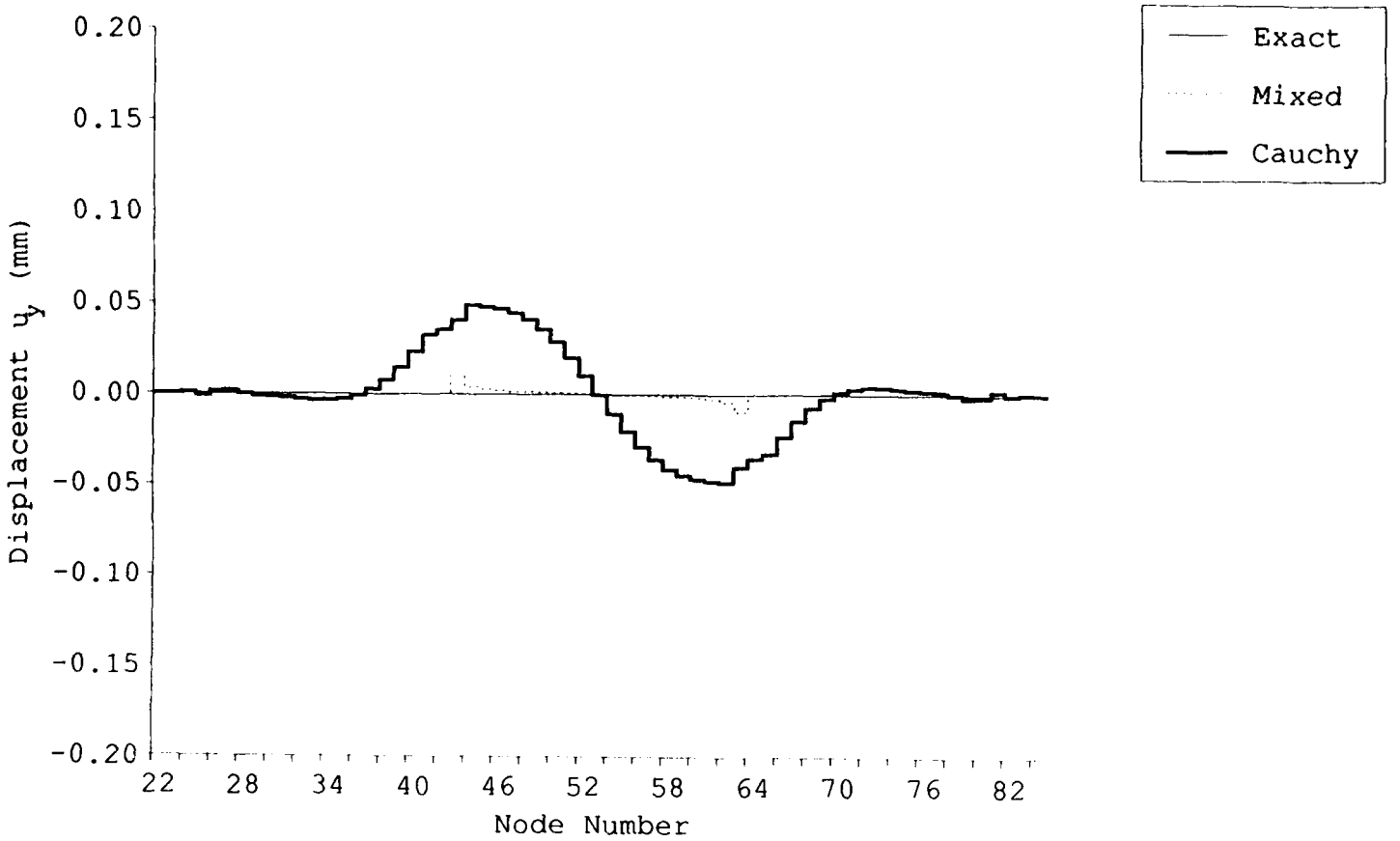
0.20
0.15
0.10
0.05
0.00
-0.05
-0.10
-0.15
-0.20
Displacement u_y (mm)
22
28
34
40
46
52
58
64
70
76
82
Node Number
Exact
Mixed
Cauchy

Figure 19

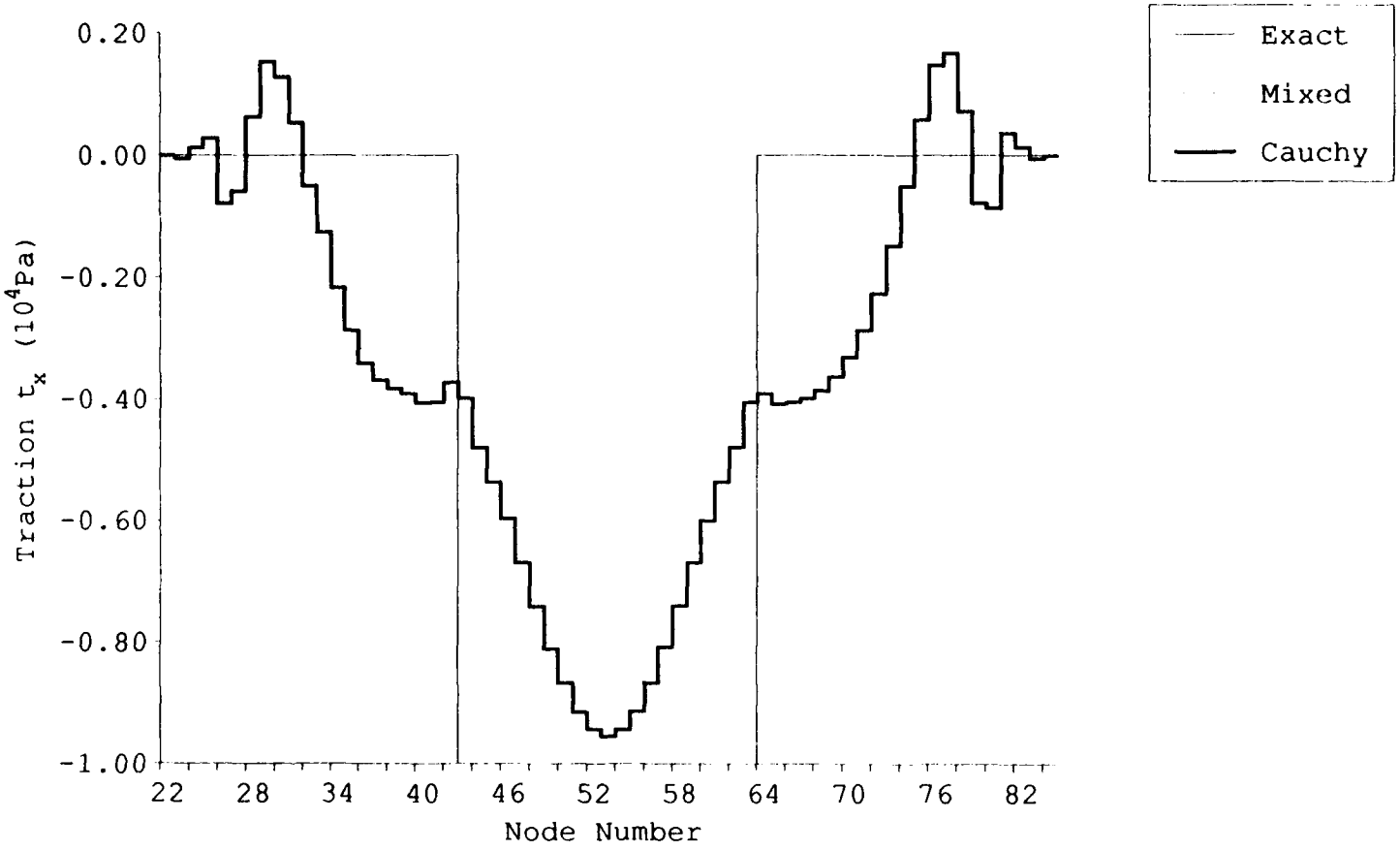
0.20
0.00
-0.20
-0.40
-0.60
-0.80
-1.00
Traction t_x (10^4Pa)
22
28
34
40
46
52
58
64
70
76
82
Node Number
Exact
Mixed
Cauchy

Figure 20

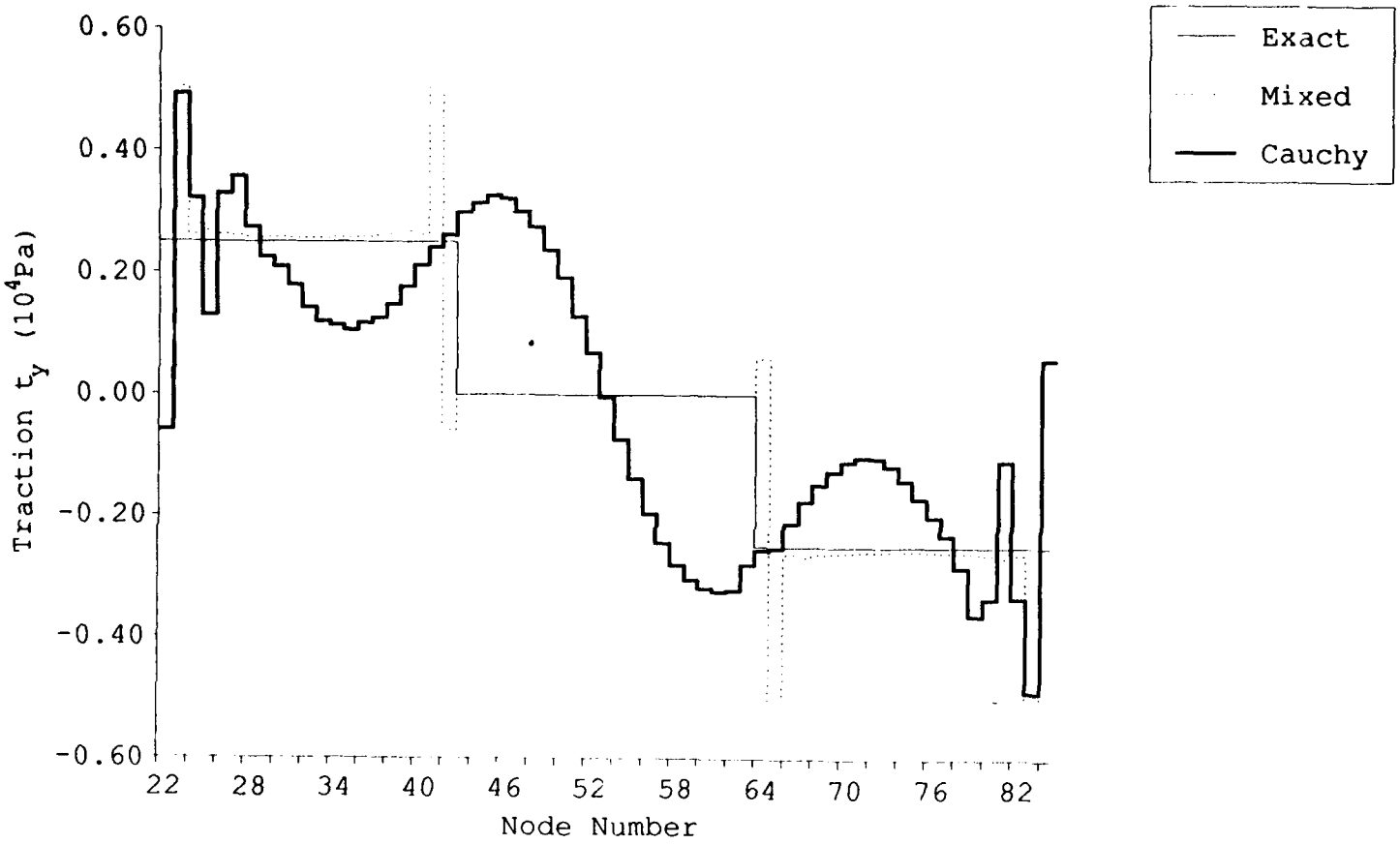
Exact
Mixed
Cauchy
0.60
0.40
0.20
0.00
-0.20
-0.40
-0.60
Traction t_y (10^4Pa)
22
28
34
40
46
52
58
64
70
76
82
Node Number

Figure 21

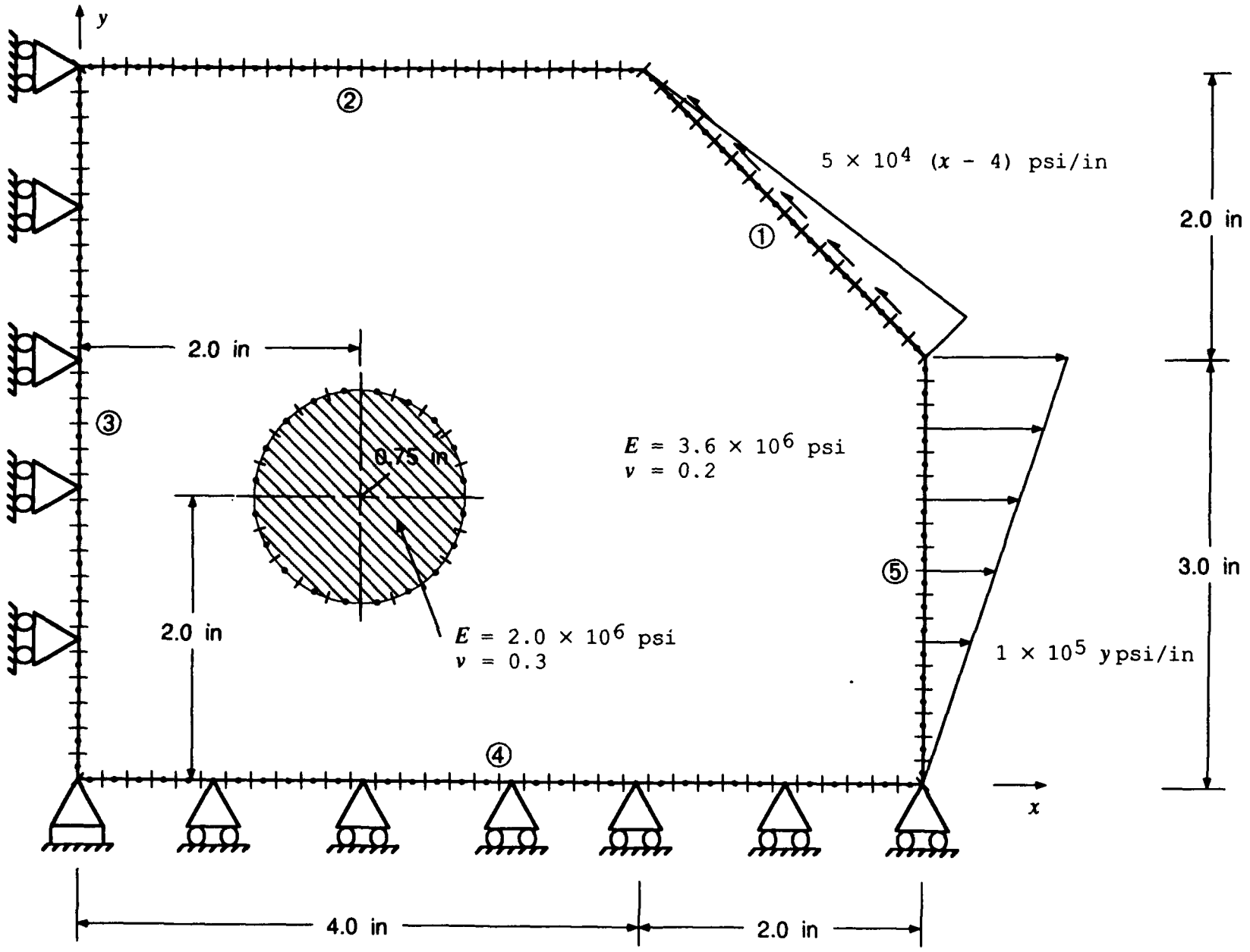
y
x
①
②
③
④
⑤
5 × 10^4 (x - 4) psi/in
1 × 10^5 y psi/in
2.0 in
3.0 in
2.0 in
2.0 in
0.75 in
E = 3.6 × 10^6 psi
ν = 0.2
E = 2.0 × 10^6 psi
ν = 0.3
4.0 in
2.0 in

Figure 22

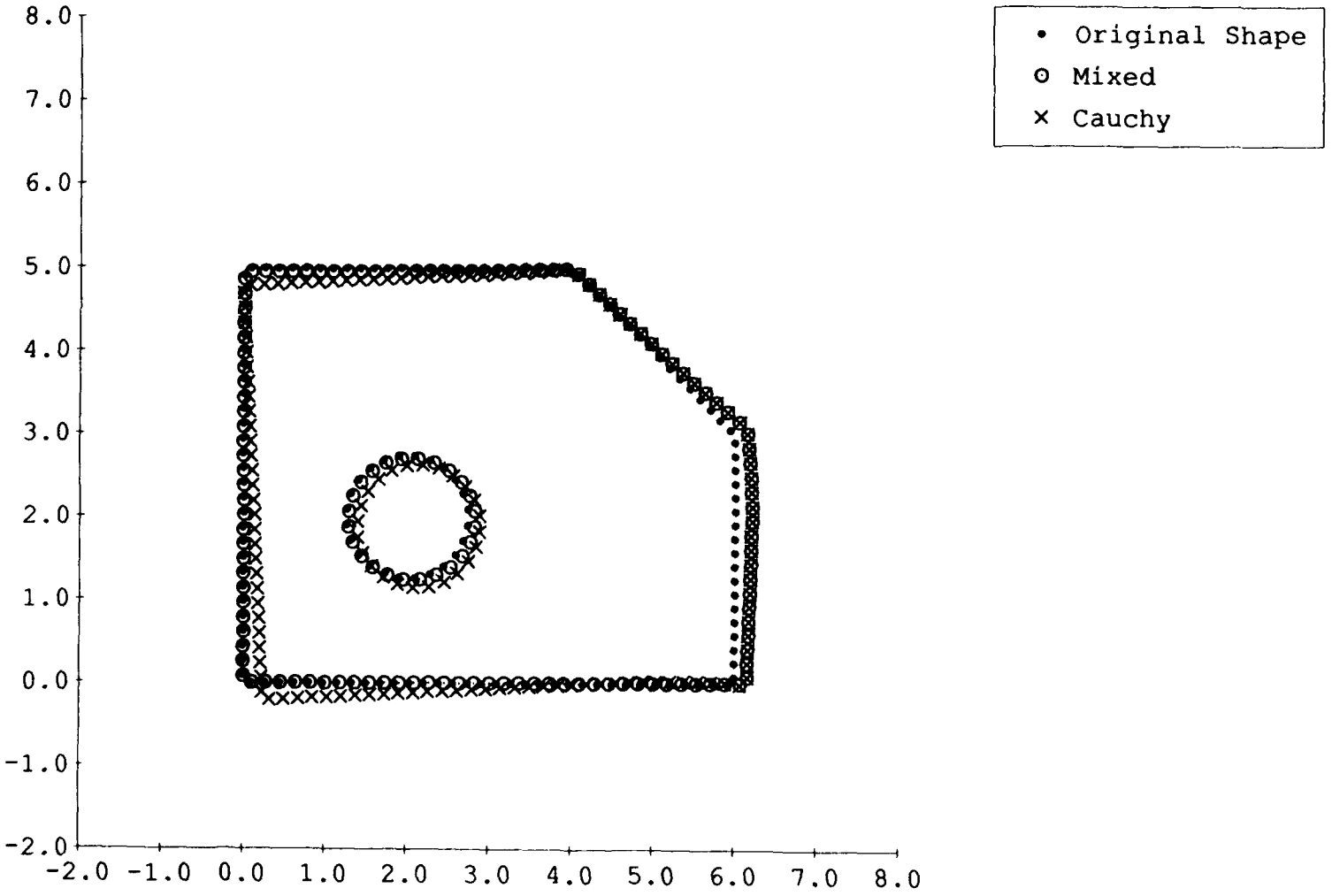
8.0
7.0
6.0
5.0
4.0
3.0
2.0
1.0
0.0
-1.0
-2.0
-2.0 -1.0 0.0 1.0 2.0 3.0 4.0 5.0 6.0 7.0 8.0
Original Shape
Mixed
Cauchy

Figure 23

APPENDIX 6

Load Diffusion and Absorption Problems from a Finite Fiber to Elastic Infinite Matrix by the Equivalent Inclusion Method

Ven-Gen Lee and Toshio Mura
Theoretical and Applied Mechanics
Northwestern University
Evanston, Ill 60208

Abstract

The load transfer behavior of a finite fiber perfectly bonded to an infinite matrix of distinct elastic properties is investigated in this paper. The fiber is subjected to the uniform distributed loading applied at infinity or on one cross section of the fiber. The stress disturbance due to the existing fiber is simulated by the equivalent inclusion method, which formulates the inhomogeneity problem to a system of integral equations. By dividing the fiber into finite numbers of ring elements with uniform distributed eigenstrains, the integral equations can be further reduced to a system of algebraic equations with coefficients expressed in terms of the integrals of Lipschitz-Hankel type. Numerical results are presented for resultant axial force for various fiber length and material properties. The limiting cases of the infinite and semi-infinite fibers are also compared with the exact and approximate solutions.